Correlation of Structure to Performance of Soft Materials for Energy Storage Systems Using Neutron Scattering

A Dissertation Presented for the
Doctor of Philosophy
Degree
The University of Tennessee, Knoxville

Md Ashraful Haque
December 2023

Dedication

This work is dedicated to my parents, siblings, and my wife for their support and encouragement.

Acknowledgments

I would not have reached where I am right now without the support of numerous people. I will try to mention all the people who contributed to this journey.

First of all, I would like to convey my gratitude to my advisor, Dr. Mark D. Dadmun, for his continuous guidance, care, and motivation throughout my Ph.D. journey. I still remember the day when I first met Dr. Dadmun. When he showed me the project I would be working on, I told him honestly that I did not know anything about neutron scattering. Probably realizing my insecurity, Dr. Dadmun told me none of his student who joined the group knew neutron scattering and assured me that he would help and teach me. He kept his word and guided me in each hurdle that I faced. I have enjoyed working with him so much and can certainly say that without his help and guidance, I would not have been here. I would like to thank my committee members, Dr. Tessa Calhoun, Dr. Joshua Sangoro and Dr. Fred Heberle, for their guidance in improving my critical thinking.

I would like to thank my collaborators Dr. Tony Feric, Dr. Sara Hamilton, Dr. Alexandra Easley, Dr. Ah-hyung Alissa Park, Dr. Jodie Lutkenhaus, and Dr. Adam Imel, whose contribution has enriched my research. I would also like to thank the Breakthrough Electrolytes for Energy Storage (BEES), an Energy Frontier Research Center funded by the U.S. Department of Energy, for funding my research work during my tenure at UTK.

While working in the Dadmun group, I encountered excellent researchers who helped in my research projects at the initial stages and also contributed to different phases of my research. I would like to mention the name of Dr. Samantha Rinehart, Dr. Luke Heroux, Dr. Joshua Moncada,

Dr. Jacob Fischer, whose guidance made my research endeavor enjoyable. I also want to thank all my current lab group members for making life easy and fun in the lab.

I would like to mention the name of a few of my mentors who contributed to my academic career. First, I would like to mention my high school chemistry teacher, Nazmul Haque, who has been a great support. I would like to mention Dr. Md. Ashaduzzaman and Shaikat Chandra Dey for their contribution and support while pursuing my MS degree.

The life of an international student in the U.S. at the initial stages is tough, but the contribution of some people made it easy to survive here. First, I want to mention the efforts of Dr. Tasmia Rahman Tumpa and Dr. Md Musabbir Adnan Tamim, who helped my wife and me in the move-in process to our first home here. I still remember and am grateful for your hospitality on the first night in the US. Then I will mention my favorite couple- Dr. Fatema Wahida and Dr. Mohammed Fahad Hasan for helping me with the admission process at the University of Tennessee, Knoxville (UTK), supporting me in one of my worst times in graduate school, and giving the care and space I needed. I want to mention Shoma Saleheen and Dr. Amirus Saleheen- for your continuous blessing and care; specifically, I would mention your effort of caring for me by inviting me for dinner and serving my favorite dish (khichuri). I would also like to thank Dr. Mohammad Al Mamun for his guidance and support. Finally, I will mention Dr. Muhammad Redwan Hassan's name, who is the most entertaining person I have met in my whole life. I am grateful to have him as a friend. Thank you, Redwan, for allowing me to share my happiest and darkest moments with you, which helped me to be a better version of myself. I would also like to thank some of my friends who have been a great support during stressful times. Dr. Pagnareach Tin, Dr. Ruhani Sagar, Dr. Virginia White, Austin Riggins, Dr. Michael Kelly, Dr. Trevor Wilson, and Dr. William Ledford, thank you for making my journey at UTK memorable and less stressful.

I would like to mention my two pets – Turbo & Loki. They have been my emotional savior in this Ph.D. journey. I also want to thank Manchester United- my favorite soccer team, the season 2022-23 has been great for this team, and each game they played boosted and motivated me while writing my dissertation.

I would like to thank my parents and siblings for their unwavering support throughout my academic career. I want to mention my mom's hard work, dedication and care throughout my life. She has gone through so much to make my life better. I want to thank my father for teaching me Math and English in my early childhood, which helped me throughout my academic life. I want to thank my elder brother, Dr. Md Shariful Haque, for his kindness, support, and assistance in every step of my life. I also want to thank my sister, Nashita Tanzeem, for her care and encouragement. I would also like to mention my sister-in-law Dr. Tasnuva Mahjabin and my nephew, Nazeef Mabruk, for their care and support.

Finally, I want to thank my wife, Zarin Tasnim, for her tremendous support, motivation and care during the tough times of my graduation journey. Zarin, you were there in my worst days when I had no confidence in myself, for which I will always be grateful to you.

Abstract

This dissertation presents work that expands our understanding of the relation between the structural features of soft materials applicable in energy storage systems such as redox flow batteries (RFB) and organic radical batteries (ORB) to their performance. The studies focus on soft materials- nanoparticle organic hybrid materials (NOHMs) and the radical polymer, poly (2,2,6,6-tetramethylpeperidinyloxy-4-yl methacrylate) (PTMA). The results obtained in these studies provide a holistic understanding of the structural features of NOHMs and PTMA in solution that may provide insight to rationally improve the performance of energy storage systems.

The first two projects investigate the structure and assembly of nanoparticle organic hybrid materials (NOHMs) in aqueous solution with and without supporting electrolytes using small angle neutron scattering. The first project focuses on the structure and assembly of the polymer canopy and NOHMs with increasing concentrations of NOHMs in aqueous solution with and without supporting electrolyte. The research highlights that a large amount of polymer ungrafts from the nanoparticle surface to free polymer that interact with the grafted polymer canopy. The second project explores the impact of tuning the bonding type (ionic vs. covalent) of the polymer canopy grafted to the nanoparticle in the structure and assembly of NOHMs in aqueous solutions with and without supporting electrolyte. In presence of supporting electrolyte, ionic NOHMs structure observe a collapsed polymer conformation on the nanoparticle surface and covalent NOHMs shows a subtle change in conformation of the polymer canopy.

The next part of the research focuses on the assembly of NOHMs near the electrode surface using neutron reflectivity. This research highlights that under applied potential, the ordering of NOHMs dramatically changes, impacting the current density of the NOHMs solution.

The final project investigates the conformation and assembly of PTMA in solutions with variations in radical loading in the PTMA backbone and temperature using small angle neutron scattering. The results highlight that the amount of radical loading is the primary factor governing the final conformation of PTMA. Correlating the conformation of PTMA in solutions to the electrochemical performance indicates that PTMA with collapsed chain conformation improves the charge transfer process.

Table of Contents

List of Tables

List of Figures

Chapter I Introduction

Overview

This chapter highlights the importance of energy storage systems and introduces two energy storage systems: Redox Flow Batteries (RFB) and Organic Radical Batteries. This chapter also sheds light on Nanoparticle Organic Hybrid Materials (NOHMs) and their potential use as a novel electrolyte in RFB as well as nitroxide-based radical polymers, including poly(2,2,6,6-tetramethylpiperidinyloxy-4-yl methacrylate) (PTMA), which may be used as a cathode material in Organic Radical Batteries. Finally, the chapter provides a foundational understanding of how neutron scattering can be used to determine the structure and assembly of NOHMs and PTMA to provide insight into their performance in their respective applications.

Importance of Energy Storage Systems

In order to meet the goals of the Paris Agreement, which target limiting the rise of worldwide temperature to 2 °C, it is of utmost importance to introduce renewable energy sources in the existing electrical grid.[1] Wind and solar energy are commonly considered promising renewable energy sources. In fact, 62% of the renewable energy allocation in the US is met from wind and solar sources, and this is expected to rise to 82% by the year 2050.[2] However, the sporadic nature of these renewable sources makes it difficult to integrate renewable energy in the existing grid system properly. Moreover, studies suggest that the current electricity grid will fail if 60% of the total energy comes from renewable energy sources without significant changes to energy storage technologies.[3–5] These factors necessitate the development of next-generation energy storage systems.

Currently, there are a number of energy storage technologies that exist in the market. These include pumped storage hydropower (PSH), ice and chilled water storage, compressed air energy storage (CAES), flywheel energy storage, supercapacitors and batteries such as lithium (Li)-ion, and flow batteries.[6–8] According to the International Renewable Energy Agency (IRENA), 123 GW of energy storage is required before 2050 to attain a sustainable energy production and storage system that will keep the global temperature below 2 °C.[9,10] In the U.S., only *ca.* 20% of 123 GW energy storage existed as of 2020. PSH fulfills 93% of this energy storage.[8] Hence, it is of utmost importance to increase the capacity of current energy storage systems. Among the energy storage systems mentioned above, batteries have the greatest potential as they can be developed for mobile applications and transportation. Moreover, batteries possess significant energy density and shorter discharge time scales, making them desirable as energy storage systems. Among all the batteries, redox flow batteries (RFBs) are considered ideally suited to meet the increased demand for energy storage systems on the grid level. This is primarily due to the fact that RFB allows the separation of energy and power which enables scaling the power delivery and energy density according to the need.[11]

Although it seems exciting to integrate the RFB into the grid system, current RFB systems still suffer from low energy density. In the current market, Li-ion batteries (LIB) are preferable as an energy storage system as they provide an order of magnitude higher energy density than RFB.[12] Due to the combination of high energy and power density, LIB has been used in many sectors, including smartphones, laptops, electric vehicles, etc.[13,14] The common cathode material in LIB is $LiCoO_2$, requiring cobalt (Co), which is a rare earth element.[14,15] Co is only available in limited geographical areas, making it expensive for their use in Li-ion batteries.[16] Using organic-based polymeric materials in a battery cathode can be an alternative approach to relieve the problems

associated with the extensive mining and supply chain issues related to Co.[15,16] Recently, the use of organic radical batteries (ORB) has been on the rise, replacing the transition elements used in LIB cathodes with organic material.[17] The lucrative theoretical capacity of 147 $mAhg^{-1}$, comparable to the capacity of $LiCoO_2$ (140 $mAhg^{-1}$), makes ORB a highly desirable battery technology in current and future technologies.[18,19]

To improve the performance and integrate RFB and ORB systems in the current electrical system, it is crucial to have a fundamental understanding of the materials that are needed for the next generation of these promising systems. Hence, the following sections briefly review the RFB and ORB technologies and propose materials related research projects that can address potential hurdles and shortcomings in these systems.

Redox Flow Battery

RFB technology differs from a conventional battery system as the electro-active species are stored separately in external tanks. Figure 1 shows an illustration of the operation of a typical RFB. Besides the external tanks, an RFB consists of a cell with an ion exchange membrane separating the electrodes. The electroactive species are transported from the external tanks with the help of pumps to the cell. During the discharging process, the active species are reduced at the positive electrode, releasing an electron and at the negative electrode, the active species are oxidized by accepting an electron. During the charging process, the reverse reaction takes place. The ion exchange membrane allows protons to pass from the positive end to the negative end of the cell. Multiple cells may be stacked together to develop an RFB that scales power delivery. Additionally, the energy storage capacity of an RFB system is also scalable by varying the size of the tank or concentration of the electroactive species.[20,21]

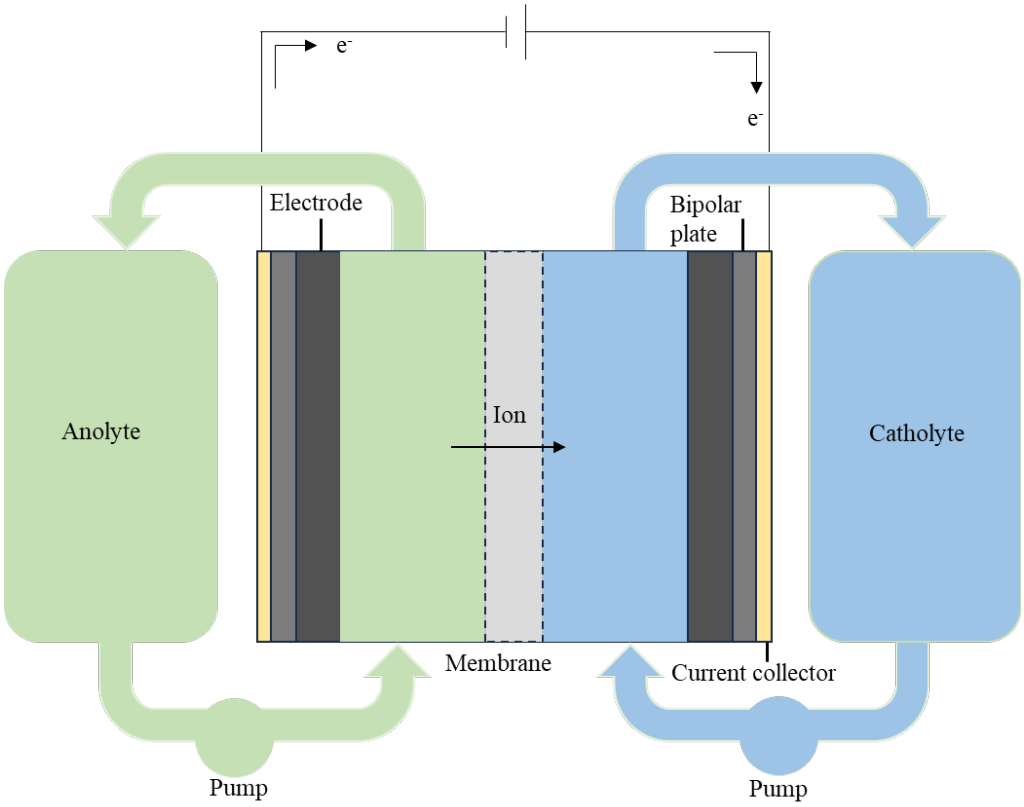

Figure 1. Diagram of redox flow battery (RFB), with anolyte and catholyte in separate tanks. Electrons travels through the external circuit whereas ions pass through membrane.

Two types of electrolytes are typically used in RFB systems, i) aqueous electrolytes and ii) non-aqueous electrolytes. Aqueous electrolytes are advantageous over non-aqueous electrolytes as they provide high energy and current density. However, the aqueous electrolytes suffer from limited coulombic efficiency.[22,23] Furthermore, the energy density of the most popular redox flow battery is around 25-35 Wh/L that is an order magnitude lower than the common lithium-ion batteries.[24] Hence, novel electrolytes are needed to improve the performance of RFB. In this study, nanoparticle organic hybrid materials (NOHMs) are proposed as a component that is added to the aqueous redox flow batteries to increase the solubility of the electroactive species and improve the energy density of the RFB system. Moreover, the presence of NOHMs may promote a smooth deposition of metal on the electrode surface, reducing dendrite formation and increasing the lifetime of the battery.

Organic Radical Battery

Organic Radical Batteries have a similar design and working principle as LIB. In a typical ORB, graphite material is used as anode material and a radical organic moiety, commonly a nitroxide radical, is used at the cathode. Similar to LIB, organic solvents such as ethylene carbonate:diethyl carbonate/dimethyl carbonate or propylene carbonate:ethylene carbonate:dimethyl carbonate mixtures are used with added lithium salt ($LiPF_6$, $LiBF_4$) in ORB.[25,26] The chemical moieties such as nitroxyl, hydrazyl and phenoxyl are preferable as functional groups for the use in organic radical battery.[27,28] Figure 2 illustrates a scheme of a typical organic radical battery.

The use of manganese, iron, nickel and other transition metals in LIB results in the limited recyclability of LIBs and may have toxic side effects.[29] The use of organic moieties with stable radical pendant groups in place of these transition metals may alleviate the limited recyclability

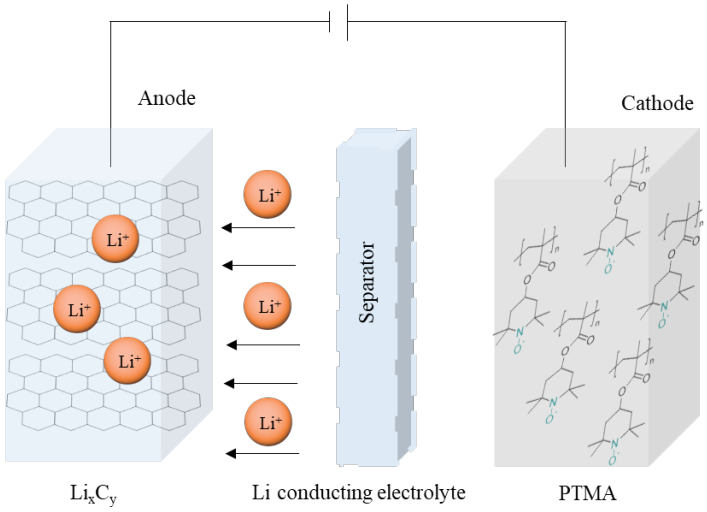

Figure 2. Schematic of Organic Radical Battery (ORB) where graphite works as anode and PTMA works as cathode. Li conducting electrolytes transport lithium ions.

issues of LIBs. These polyradicals undergo reversible redox reactions with the potential of long-time stability. Among the possible polyradicals, poly (2,2,6,6-tetramethylpiperidinyl-oxy methacrylate), PTMA is the most studied organic radical polymer due to its high theoretical capacity and easy synthesis.[30] However, the conformation and thermodynamic interaction of PTMA in common battery solvents are not well established. Hence, to improve the performance of ORB that incorporates PTMA, it is essential to understand the molecular arrangement of PTMA under conditions that are similar to operation. In this study, we investigate the conformation and thermodynamics of PTMA in various battery-relevant solvents at different temperatures.

Nanoparticle Organic Hybrid Materials (NOHMs)

NOHMs are nanocomposites that consist of polymer grafted to an inorganic nanoparticle. The grafted polymers form canopies on the nanoparticle cores. Previous studies showed that changing the core or the chemical nature of the polymer allows the formation of NOHMs that are a glassy solid, a gel or a liquid-like material that flows.[31,32] The earlier generation NOHMs, initially referred to as Nanoscale Ionic Materials (NIMs), were developed by grafting sulfonate terminated polymers to tertiary-amine functionalized inorganic cores.[32,33] The next generation of NIMs was prepared by functionalizing the core with sulfonate groups, whereas the polymer canopy was a polyetheramine (HPE), with one amine functional end group.[34,35] This allowed the development of NIMs/NOHMs with a variety of polymer canopies.

NOHMs provide great advantages in many technologies, including zero vapor pressure, increased thermal stability, high conductivity, and a large electrochemical window without the use of additional solvents.[31,36–40] These unique features allow NOHMs to be used in various applications such as lubricants,[41] water treatment,[42] pretreatments of chemicals,[39] small molecule capture[37,43] and electrolytes.[31] Recently, NOHMs have been proposed to be used in RFB systems

as additives, with the hypothesis that the interaction of electrolytes with the polymer canopy will allow increased solubility of conductive species. It is hypothesized that this will also increase the energy density of a conventional RFB.

Although NOHMs have been proposed to be used in RFBs, the structure and assembly of NOHMs in aqueous solutions are not well understood. Previously, attempts have been made to understand the structure and assembly of neat NOHMs or NOHMs with the presence of the host polymer as a matrix. For instance, Fernandes et al. used small-angle X-ray Scattering (SAXS) to investigate the ordering of NIMs that consists of amine-terminated poly(ethylene oxide) PEO as a cation and silica nanoparticles with hydroxyl groups (silanols) as anion. The NIMs showed a high degree of ordering of particles in thin films and bulk with a particle-to-particle distance of 27 nm.[44] A molecular dynamics simulation study showed that all the polymer present in the system were grafted to the nanoparticle by overcoming the entropic barrier in highly stretched conformations. When salt is added to the system, electrolyte ions occupy some grafting sites; hence some polymer desorbs away from the surface.[45] McDonald et al. investigated a subset of NOHMs termed liquid polymer nanocomposites, where the polymer is used as a matrix to disperse the NOHMs. Using Small Angle Neutron Scattering (SANS), the study shows that the polymer grafted to the nanoparticle attains a relaxed state at a grafting density of 0.7 chains nm^{-2}. Moreover, variation in the inorganic core size can induce reversible aggregation in the bulk structure.[46] These studies suggest that a number of factors can impact the structure and assembly of NOHMs. Hence, it is crucial to understand the structure and assembly of NOHMs to fully elucidate the performance of NOHMs in an electrochemical environment. Figure 3 shows an illustration of ionic NOHMs or NOHM-I-HPE and covalent NOHMs or NOHM-C-HPE used in this study. Here, SiO_2 is used as the inorganic core and an amine-functionalized polyethylene oxide/polypropylene oxide

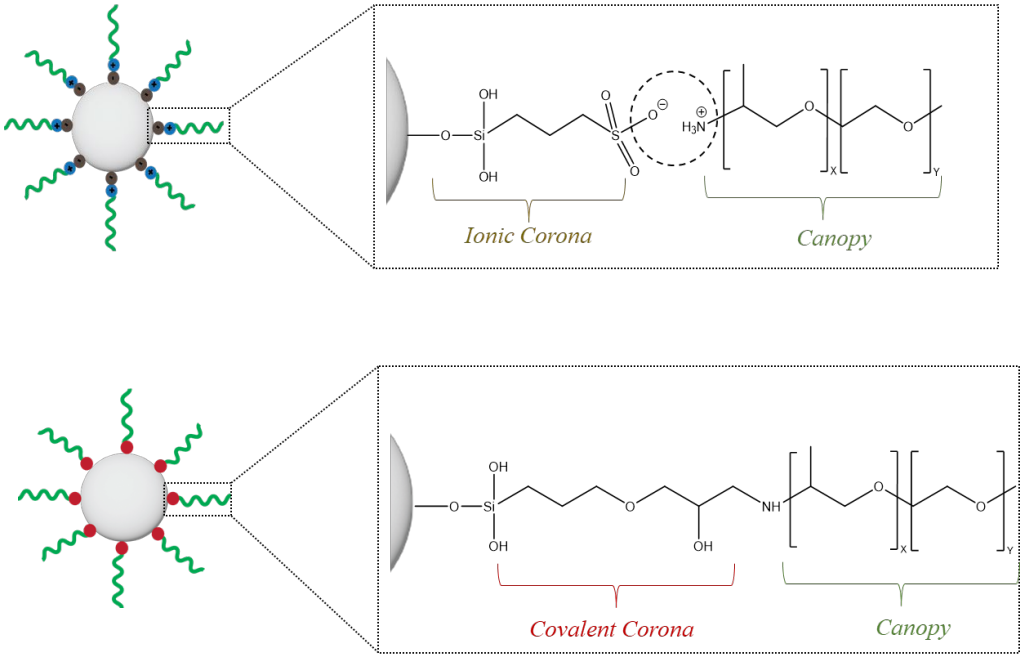

Figure 3. Graphical representation of NOHM-I-HPE and NOHM-C-HPE. The core is SiO_2 nanoparticles and HPE polymer is ionicially or covalently grafted to the functionalized silica nanoparticle.

(PEO/PPO) copolymer or JEFFAMINE M2070, which is abbreviated to HPE, is used as the organic canopy. In this study, Chapter 2 reported the investigation of the structure and dispersion of NOHM-I-HPE in aqueous solution at a series of concentrations 10-40 wt.% with and without the presence of supporting electrolyte. Chapter 3 highlights the impact of the grafting motif of the polymer to the silica nanoparticle core on the structure and assembly of NOHMs in aqueous solutions. Finally, Chapter 4 elucidates the ordering of NOHMs in aqueous solution near an electrode surface.

Organic Radical Polymer : PTMA

The (2,2,6,6-tetramethylpiperidin-1-yl)oxidanyl or Tempo-based organic radical polymer PTMA, is an often studied radical polymer that may be used as cathode material in an ORB. PTMA has a backbone structure that is similar to poly(methyl methacrylate) (PMMA) with a TEMPO radical as a pendant group. The four methyl groups around the nitroxide radical preserve the steric stability of the radical. During the charging process, the reduction and oxidation process of PTMA results in an oxoammonium cation or aminoxyl anion. During discharging, the nitroxide radical regains its stability by acquiring the electron in a hopping mechanism.[47–49] Figure 4 shows the reversible oxidation-reduction reaction of the TEMPO radical. The TEMPO radical may be used as either positive and negative electrodes in batteries. However, the instability of the anion in typical carbonate-based electrolytes limits its applicability. The application of TEMPO with a backbone such as PMMA in the ORB system may increase the charge density of the system. Moreover, the operational capacity at almost 100% of the theoretical capacity, impressive chemical stability, and a life cycle of 1000 recharges make PTMA a lucrative choice to use in ORBs.[27,29,49,50]

Recently, efforts have been made to establish a relationship between the conformation of the PTMA polymer and the charge transfer process of PTMA. Molecular dynamics simulations

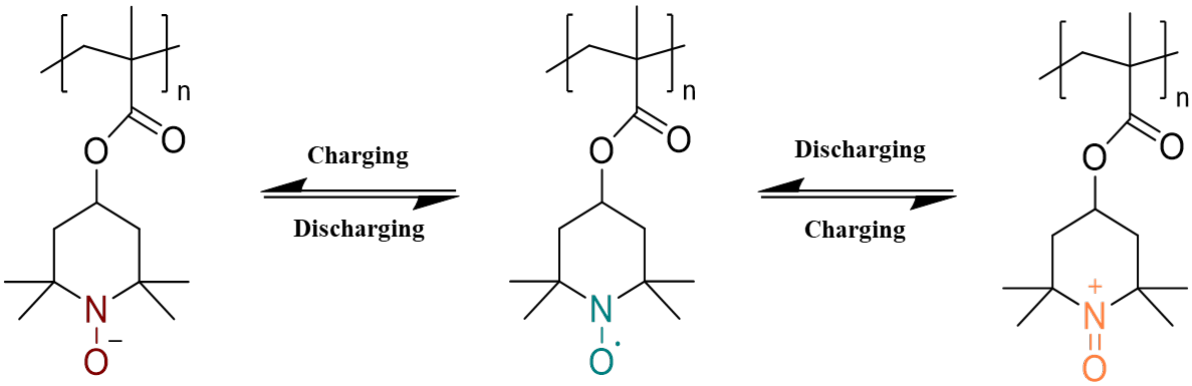

Figure 4. Oxidation-reduction mechanism of PTMA. In the oxidation process, the nitroxide radical converts to aminoxyl anion, and in the reduction process, the nitroxide radical converts to oxoammonium cation.

indicate that in the amorphous film, the *interchain* interactions of PTMA dominate over *intrachain* interactions. This assembly contributes to the increased coupling of the nitroxide radical with the neighboring chains. This interchain interaction results from the bulky TEMPO pendant group that limits the close intramolecular packing of the PTMA polymer chain.[47] Using Electron paramagnetic resonance (EPR), Bobela et al. establish that the amount of radical loading dramatically affects the molecular conformation of PTMA. The study investigated a random co-oligomer of PTMA-X where X refers to the amount of TEMPO radical in the backbone. Here, EPR observed the coupling of the -NO• groups, where the results show that the radical coupling reaches a maximum at approximately 60% of TEMPO in the polymer backbone.[50] Small-angle neutron scattering study performed by Martin et al. investigated the conformation of PTMA-X in both neutral and oxidized states. In the neutral state, it is observed that the rigidity along the polymer backbone increases with increasing radical loading, which biases the formation of more inter-chain interactions. In the oxidized state, the polymer chain with 100% TEMPO radical does not change its conformation with oxidation; however, the chain with 20% TEMPO radical loading forms a more rigid conformation when oxidized. These studies indicate that the conformation of the polymer chain depends on the TEMPO radical, the amount of radical on the polymer chain and its oxidation state.[51]

In order to have an in-depth understanding of the performance of PTMA in the battery systems, Chapter 5 of this dissertation reports the results of an investigation of the conformation and thermodynamic interaction of PTMA polymer in battery-relevant solvents: N-methyl-2-pyrrolidone (NMP) and a 50:50 (wt.%) ethylene carbonate:dimethyl carbonate (EC:DMC) at two temperatures (25 °C and 60 °C). Moreover, our study also investigates the impact of radical loading on the conformation of PTMA chains in these solvents.

The next section will briefly review two characterization tools primarily used in this study- small-angle neutron scattering and neutron reflectivity. The review will explain the working principle as well as the importance of using neutron scattering to elucidate the structure and assembly of NOHMs and the conformation of PTMA in solution.

Small angle scattering

Small angle scattering investigates structures in the length scales of *ca.* 0.1-200 nm.[52]. A general picture of the scattering experiment involves the interaction of a beam of radiation (X-ray, neutron or light) with the target material. In X-ray radiation, X-rays interact with electron clouds of the scattering atom, whereas in neutron scattering the interaction occurs between the neutron and nuclei of an atom. This feature of neutron scattering provides some advantages over X-ray scattering as the technique allows isotope labeling that changes the scattering pattern with little perturbation to the native structure leading to a unique structural determination of the material of interest. Moreover, neutron scattering is a non-destructive technique allowing samples to be remeasured multiple times.[53] Due to these advantages, neutron scattering is used as the primary tool for investigating of the structure of NOHMs and PTMA in solution.

In a basic scattering experiment, the radiation interacts with a material with initial incident wave vector $\boldsymbol{k_i}$ and scatter off the material with a final wave vector $\boldsymbol{k_f}$, as shown in Figure 5. Here, the modulus of the wave vector, $\boldsymbol{k}$ equals to $2\pi/\lambda$ and the change in wave vector ($\boldsymbol{k_i} - \boldsymbol{k_f}$) corresponds to the momentum transfer, **Q**. In elastic scattering, no change in energy is observed. Therefore, the magnitude of the final and the initial wave vector is the same, $|\boldsymbol{k}| = |\boldsymbol{k_i}| - |\boldsymbol{k_f}|$. The vector diagram in Figure 5 elaborates the relation between the wave vector, $\boldsymbol{k}$ and momentum transfer, **Q**. Figure 5 shows that the wave vector of the incident radiation $\boldsymbol{k_i}$ is scattered off of the particle at an angle of 2θ as the scattered radiation $\boldsymbol{k_f}$. As the magnitude of the wave

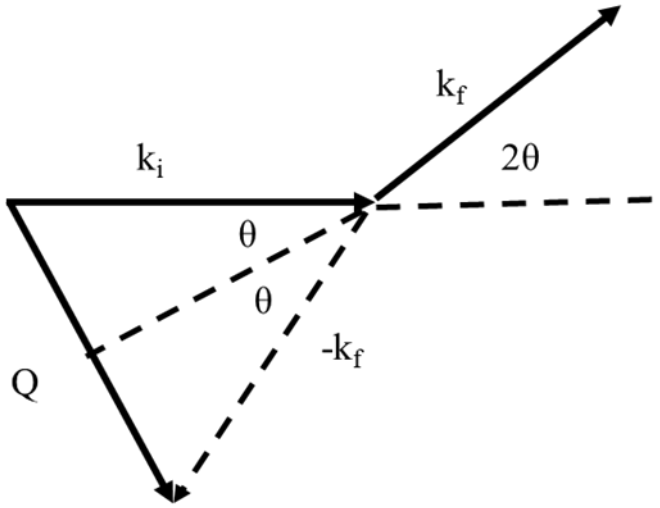

Figure 5. Vector diagram of the scattering event. where $\boldsymbol{k_i}$ is the incident radiation, $\boldsymbol{k_f}$ is the final scattered radiation, **Q** is the momentum transfer.

vector, $|\boldsymbol{k}|$ is the same in the elastic scattering, the triangle formed in the scattering event depicted in Figure 5 leads to Equation 1.1

$$\frac{Q}{2} = |k| \sin\theta \qquad \textbf{1.1}$$

Now, Equation 1.2 can be obtained from Equation 1.1, where the magnitude of the wave vector , $|\boldsymbol{k}| = 2\pi/\lambda$ in Equation 1.1.

$$Q = \frac{4\pi}{\lambda} \sin\theta \qquad \textbf{1.2}$$

The magnitude of the momentum transfer, **Q**, can be correlated with the length scales of the structure that are examined in the material of interest using Bragg's law. According to Bragg's law, $n\lambda = 2d \sin\theta$, where d is the spacing between the diffraction planes, λ is the wavelength, θ is the scattering angle and n is the order of the diffraction.[54] Combining Equation 1.2 and Bragg's law establishes a relation between Q and the scattering angle and the length scales examined, *d*.

$$Q = \frac{2\pi n}{d} \qquad \textbf{1.3}$$

According to Equation 1.3, structures with large length scales are observed by the scattering at low-Q values, and smaller length scale structures are observed by the scattering at high-Q values.[53,55]

The quantity measured in small angle scattering is the differential scattering cross section $d\sigma/d\Omega$, which is proportional to the intensity of the scattered radiation. $d\Omega$ represents a small portion of the solid angle, Ω. It emphasizes the angular region on the detector over which the intensity of the scattered radiation is monitored. Equation 1.4 documents the relationship between differential scattering cross section for neutrons and the structure of the scattering object.

$$\frac{d\sigma}{d\Omega}(Q) = \frac{1}{N}\left|\sum_j^N b_j e^{iQr_j}\right|^2 \sim I(Q) \quad \textbf{1.4}$$

In Equation 1.4, N is the number of scattering atoms, b is the scattering length of nuclei *j*, where r is the position of the nuclei. The integration of the differential scattering cross section over the entire solid angle provides the total scattering cross-section. Equation 1.5 shows the relation between the total scattering cross-section and intensity of the scattered radiation.

$$\frac{d\sigma}{d\Omega}(Q) = \frac{1}{N}\left|\int \rho(r) e^{iQr}\, dr\right|^2 \sim I(Q) \quad \textbf{1.5}$$

where ρ(r) is the density distribution of the scattering length density. Figure 6 shows an illustration of a basic scattering experiment.

Small angle neutron scattering (SANS)

SANS monitors the intensity of the scattering of neutron beams from a sample as a function of momentum transfer, Q. This technique is used to probe the structure of constructs such as polymers, nanoparticles, microemulsions and ionic liquids.[56–60] The unique feature of neutron scattering is that the neutron interacts with each atom with a specific strength, which is known as scattering length density. The scattering length density of a molecule or nanoscale object can be obtained using Equation 1.6.[61]

$$\rho = \frac{dN_A}{M_w}\sum_i \rho_i \quad \textbf{1.6}$$

Here, ρ is the scattering length density (SLD) of the scattered object, d is its density, N_A is Avogadro's number, M_w is the molecular weight of the scattered object and ρ_i is the scattering length of each atom in the scattered object. The scattering length of hydrogen is -3.74 x 10^{-6} Å and that of deuterium is 6.67 x 10^{-6} Å, where this significant difference leads to the scattering length

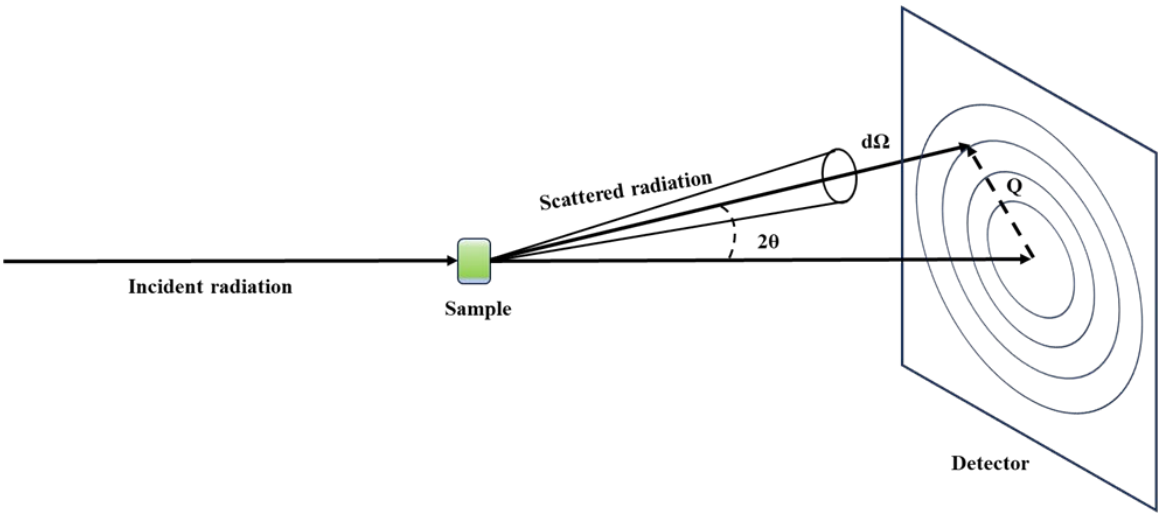

Figure 6. Schematic of small-angle scattering involving incident radiation, sample, scattered radiation and detector.

density of water (H_2O) = -5.60 x 10^{-7} $Å^{-2}$ being very different than that of deuterium oxide (D_2O) = 6.34 x 10^{-6} $Å^{-2}$.[62] The large variation in the scattering length densities of water and deuterium oxide means that sufficient contrast can be achieved in a sample by incorporating protiated solutes in a deuterated solvent or deuterated solutes in a protonated solvent. For example, to investigate the structure of the polyetheramine polymer (HPE) (SLD = 5.17 x 10^{-7} $Å^{-2}$) in aqueous solutions, deuterium oxide is used as a solvent to achieve contrast with the protonated HPE polymer. This contrast variation is not possible to achieve in small angle X-ray scattering; hence small angle neutron scattering is used to investigate NOHMs and PTMA polymers in solvents.

The measured scattered intensity from a target material consists of both coherent and incoherent scattering. The coherent scattering depends on the location of each atom at a given distance in the scattered object. In incoherent scattering, the neutrons interact with individual atoms independently and the scattered waves lose their phase coherence. Therefore, incoherent scattering does not provide any structural information about the scattered object. In SANS, the incoherent scattering is considered as background scattering and subtracted from the total scattering.[52] The differential scattering cross-section of an object in a SANS experiment is described by Equation 1.7.[61]

$$\frac{d\sigma}{d\Omega} = I(Q) = \frac{N}{V}\,(\Delta\rho^2)V_{obj}\,P(Q)\,S(Q) + B_{inc} \qquad \textbf{1.7}$$

Here, N is the number of scattering objects, V is the volume of the sample, Δρ is the scattering length density difference between the scatterer and solvent, V_{obj} is the volume of the scatterer, P(Q) is the form factor that describes the shape of the scatterer, S(Q) is the structure factor that provides information on the interparticle interaction and B_{inc} is the incoherent scattering.[53] As an example, the scattering profile of a sphere-like scatterer in a dilute solution is

provided in Figure 7. In a dilute solution, the structure factor S(Q) = 1 as the particles do not interact. The form factor of a sphere is provided by Equation 1.8.[63]

$$P(Q) = \frac{\sin(Qr) - Qr\cos(Qr)}{Qr^3} \quad \textbf{1.8}$$

In Equation 1.8, *r* is the radius of the sphere. Figure 7a shows a scattering from a mono disperse sphere and Figure 7b shows the scattering from polydisperse spheres where the scattering at high-Q is smeared due to the size distribution of the scattered particles. Inspection of Equations 1.7 and 1.8 demonstrate that the volume of the particles, the size of the particles, particle polydispersity, and scattering length density difference between the particle and surrounding medium; contribute to the intensity and shape of the scattering profile.

In this dissertation, various scattering models are used to extract information about the structure, assembly and conformation of NOHMs or PTMA from the scattering profile that emerges from the coherent neutron scattering of NOHMs or PTMA. Specifically, Chapter 2, 3 and 5 benefit from using SANS to determine the structure and assembly of polymers and nanoparticles, and each chapter provides a detailed reasoning of the models chosen to fit each scattering profile.

Neutron Reflectivity (NR)

Neutron reflectivity is a powerful technique that provides information on the buried density profile of a sample perpendicular to the surface. Typically, a resolution ranging from 5-10 Å is attainable in a neutron reflectivity experiment. The experimental data obtained using neutron reflectivity measurements is fit to the reflectivity of a model system to obtain the density profile that provides information about the buried structures. In a neutron reflectivity experiment, a neutron beam is focused on a sample at a very small angle θ. Once an incident neutron beam interacts with the sample, it either reflects off of the surface or refracts through the sample, as

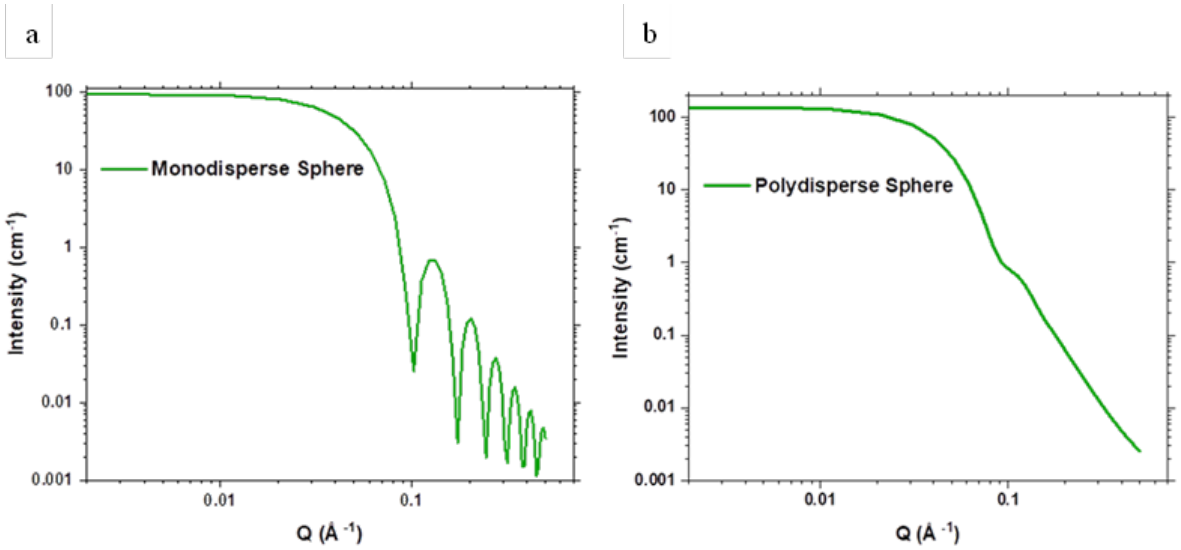

Figure 7. Small angle scattering profile of sphere of radius, r = 50 Å. Figure 7a showing scattering profile of a monodisperse sphere and 7b showing scattering profile of a polydisperse sphere

shown in Figure 8.

The relation among the incident angle (θ_0), reflected angle (θ_r) and refracted (θ_1) angle can be obtained for medium of 0 and 1 with refractive indices n_0 and n_1 through Snell's law, $n_0 \cos\theta_0 = n_1 \cos\theta_1$ and law of reflection, $\cos\theta_0 = \cos\theta_r$. In general, the top layer (L_0) is air and hence $n_0 = 1$. When the incident angle, θ_0 is less than or equal to the critical angle, θ_c, the incident radiation completely reflects off the layer. Hence, to obtain information of the buried surfaces, the reflected neutron beam is measured at an incident angle, θ_0, scanning from a small angle to an angle larger than the critical angle, θ_c. The neutron refractive index, n of a material can be obtained from Equation 1.9.[64]

$$n = 1 - \delta + i\beta \qquad \textbf{1.9}$$

Here, $\delta = \frac{\lambda^2 \rho}{2\pi}$ is the real component of the refracted index and $\beta = \frac{\lambda \rho_{abs}}{4\pi}$ is the imaginary component. In these equations, λ is the wavelength of the neutron, ρ is the SLD of the object and ρ_{abs} is the absorption density. The real component considers the transmission and reflection of incident radiation while the imaginary component considers the absorption of the radiation by the layer. The SLD, ρ, of most polymeric materials, is in the order of 10^{-6} Å^{-2}. While δ is on the order of 10^{-6} Å^{-2}, β is on the order of 10^{-8} and 10^{-9} Å^{-2}. Furthermore, since few atoms significantly absorb neutrons, the imaginary component, β of Equation 1.9, is often assumed to be negligible. The scattering lengths of elements do not follow a systematic order with an increase in molecular weight, but the large difference in scattering lengths between isotopes of hydrogen, protium ($b = -3.74 \times 10^{-6}$ Å) and deuterium ($b = 6.67 \times 10^{-6}$ Å) allows the labeling of polymer to induce contrast in a sample without interfering with the chemistry of the polymer. [62]

Neutron reflectivity, R is defined as the ratio of the intensity of the reflected neutron beam

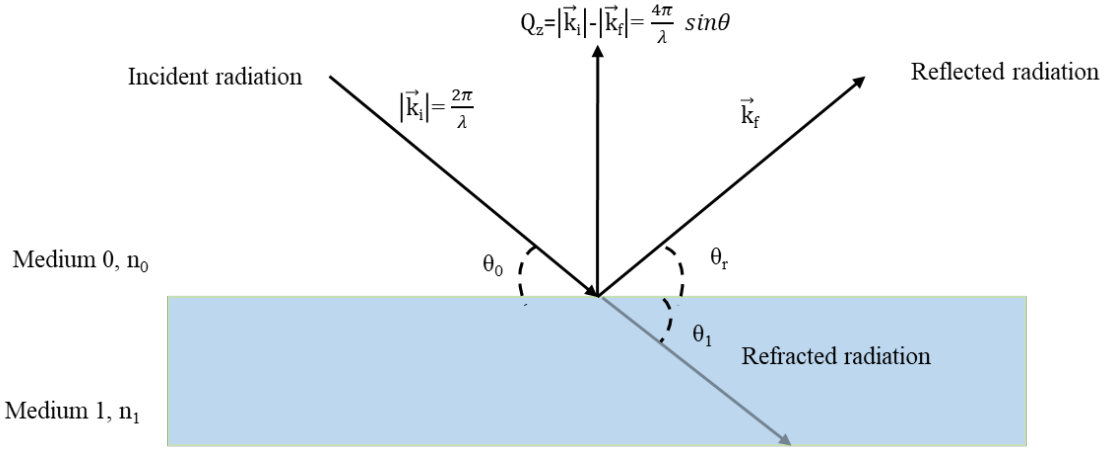

Figure 8. Geometry of general reflectivity experiment, where the difference in incident and reflected radiation provides momentum transfer Q in the z direction. θ_0, θ_r, θ_1 are the incident angle, reflected angle and refracted angle, respectively. Neutron refractive index of medium 0 and 1 are n_0 and n_1, respectively.

to the intensity of the incident neutron beam. Although neutron reflectivity depends on incident angle and wavelength of the neutron, reflectivity is typically expressed as a function of momentum transfer, Q, that accounts for both incident angle and wavelength (Equation 1.2). For a single surface without any roughness, the reflectivity profile exhibits a Q^{-4} dependence which is also known as Fresnel reflectivity. When a second material with a different SLD/refractive index than the first layer is deposited on top of the first layer, fringes can be observed in the neutron reflectivity profile owing to the interference (constructive and destructive) of the reflected neutron beam from the interface of the first and second layer and the reflected beam from the interface of the second layer and air. Equation 1.10 correlates the thickness of the layer (*d*) on the surface to the width of the fringes (ΔQ) observed in the reflectivity profile.

$$d = \frac{2\pi}{\Delta Q} \qquad \textbf{1.10}$$

In reality, there are few surfaces with no roughness and hence, the impact of this roughness on the reflected intensity must be accounted for. The roughness of a surface attenuates the reflected beam intensity, and can be accounted for quantitatively with Equation 1.11.[64]

$$R = \frac{16\pi^2}{Q^4} \Delta\rho^2 e^{-\sigma^2 Q^2} \qquad \textbf{1.11}$$

In Equation 1.11, Δρ is the variation in SLD perpendicular to the surface and σ is the roughness of the interface. Equation 1.11 quantifies that a larger variation of the SLD with depth increases the intensity of the fringes. Figure 9 shows the reflectivity profile of a silica surface with no roughness or the Fresnel reflectivity profile.[53] Figure 9 also shows a reflectivity profile of a thin film of gold deposited on the silica surface. The fringes in Figure 9 provide information about the thickness of the gold layer using Equation 1.10.

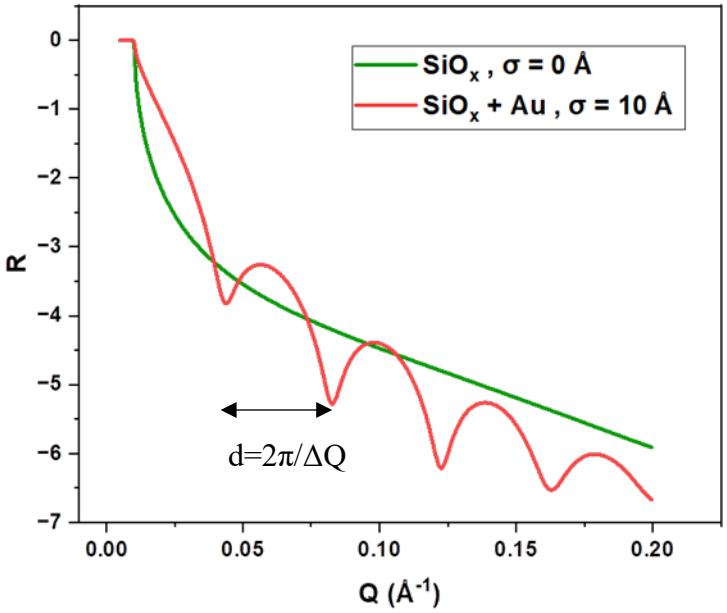

Figure 9. Examples of reflectivity profile. Green plot shows SiO_x surface with no roughness, red plot shows Au with 10 Å roughness surface on top SiO_x surface. The fringes observed on the (SiO_x + Au) reflectivity profile provides information about thickness (d) of the sample.

Equation 1.11 also shows that the roughness greatly impacts the density profile of the scattering length density. Figure 10 illustrates that with an impact of an increase in layer roughness on SLD profiles, forming more diffused SLD profiles.

In order to understand the ordering of NOHMs near an electrode surface in an electrochemical cell, reflectivity experiments of NOHMs solutions near various surfaces were performed at the Oak Ridge National Laboratory (ORNL). The neutron reflectivity experiments of NOHMs in an electrochemical cell are obtained in an inverted geometry to obtain the depth profile of NOHMs near the solid electrode surface.[65] In the inverted geometry reflectivity experiment, the incident neutron first passes through the silicon wafer at the bottom of the cell and interacts with NOHMs solution. Due to the use of inverted geometry, the electrode surfaces are prepared on a silicon wafer that is transparent to the neutrons. The reflectivity profiles obtained from these experiments were analyzed using MOTOFIT analysis package in which multilayer Parratt-formalism is used.[66] Genetic optimization with the least square method is followed to obtain the best fit of the experimental reflectivity profile.

Summary

The enhanced performance of energy storage systems can be achieved by incorporating novel and recyclable soft materials. The functionality of these soft materials depends on the molecular structure and assembly that can be tuned to increase the performance of the energy storage system. Hence, a fundamental understanding of the structure and assembly of these polymeric materials is required to optimize the performance of energy storage systems. Chapters I and II describe experiments that focus on the structure and assembly of NOHMs in aqueous solutions using small angle neutron scattering. Moreover, the interaction of supporting

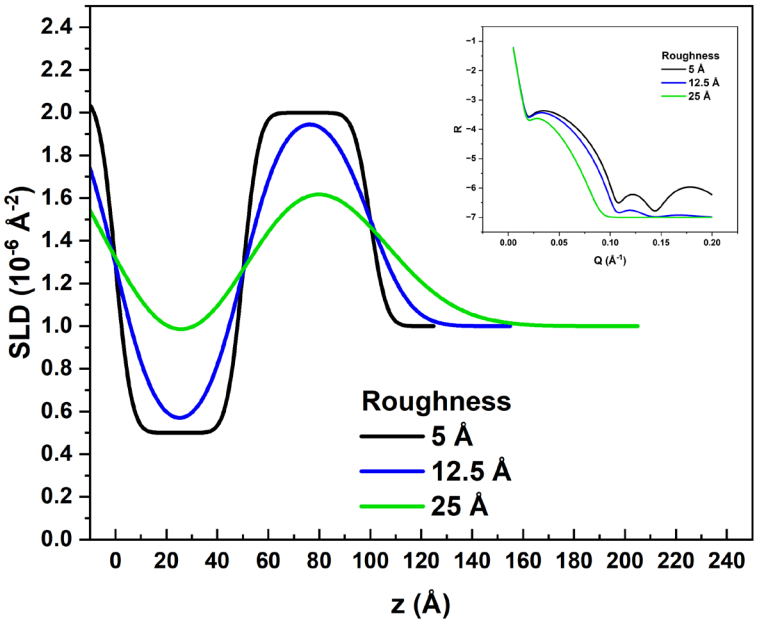

Figure 10. Demonstration of impact of roughness on the SLD profile. Black, blue and green line corresponds to 10% , 25%, 50% roughness of the layer thickness. Corresponding reflectivity profiles of roughness are provided in the inset.

electrolyte 0.1 M $KHCO_3$ with NOHMs and its impact on the structure as well as the performance of NOHMs is also detailed in both the chapters. A thorough understanding of the interaction of NOHMs with electrode material is required to enhance the performance of energy storage system. Neutron reflectivity is used in Chapter III to investigate near surface ordering of NOHMs in the presence of supporting electrolyte with and without an applied potential.

Finally, Chapter IV reports results that investigate the conformation and thermodynamics of PTMA in battery relevant solvents, N-methyl-2-pyrrolidone (NMP) and a 50:50 (wt.%) ethylene carbonate:dimethyl carbonate (EC:DMC) using small angle neutron scattering. This study also focuses on the change in conformation with temperature (25 °C and 60 °C) and radical loading (68% vs 98%) on the backbone of the PTMA polymer chain. The results obtained from this study expand our understanding of the conformation of PTMA polymer chain in solutions that correlates to the electrochemical performance of PTMA in devices.

Chapter II Structure and Dispersion of Free and Grafted Polymer in Nanoparticle Organic Hybrid Materials-based Solutions by Small-Angle Neutron Scattering

A version of this chapter was originally published by Md Ashraful Haque, Tony G. Feric, Sara T. Hamilton, Ah-Hyung Alissa Park, Mark D. Dadmun :

Md Ashraful Haque, Tony G. Feric, Sara T. Hamilton, Ah-Hyung Alissa Park, Mark D. Dadmun. 'Structure and Dispersion of Free and Grafted Polymer in Nanoparticle Organic Hybrid Materials-based Solutions by Small-Angle Neutron Scattering'. *J. Phys. Chem. C* 2021, 125, 9, 5327–5334.

Md Ashraful Haque performed all the SANS experiments and analysis. Tony G. Feric and Sara T. Hamilton synthesized the NOHM-I-HPE and measured viscosities of the solutions.

Abstract

Liquid-like Nanoscale Organic Hybrid Materials or NOHMs consisting of polymer grafted nanoparticles have shown great promise in applications, such as electrochemistry and gas separation due to their enhanced conductivity, tunability, and negligible vapor pressure. Recently, NOHMs are considered to be used as novel electrolytes in Redox Flow Batteries (RFBs). However, to employ NOHMs in redox flow batteries as electrolytes it is important to understand the conformation and dispersion of NOHMs in the electrochemical milieu. Here, we report the use of small-angle neutron scattering to probe the structure and dispersion of Jeffamine M2070 polymer grafted to SiO_2 nanoparticle in an aqueous solution with and without the presence of a supporting electrolyte. Our results indicate that in the aqueous environment, there exists a large amount of free polymer in the solution that is not grafted to the functionalized nanoparticles. These protonated free polymers, dispersed in the aqueous solvent, may also strongly interact with the grafted polymer layer and greatly affect the neat structure of NOHMs. Thus, there also exist polymers

identified as “interacting” polymers to distinguish them from tethered or truly free polymers in the fluid system. The presence of supporting electrolyte shows a greater effect on the structure of NOHMs-based fluid as it not only alters the structure of the free polymer but also hinders the interaction of the polymer with the functionalized nanoparticles. Moreover, the change in the interaction of the Jeffamine M2070 with the functionalized nanoparticles due to the addition of supporting electrolyte has revealed a drastic change in the viscosity of NOHMs solutions. Overall, the dispersion of the free polymer, the interaction of the interacting polymer with grafted polymer as well as the change in conformation of free polymer and grafted layers with the addition of supporting electrolyte provides valuable insight into the overall scenario of the electrochemical environment of NOHMs. These results can be applied to fine-tune the structure of liquid-like NOHMs and will aid in a better understanding of their performance as potential electrolytes in RFBs.

Introduction

The performance of redox flow batteries (RFBs) is known to be limited by electrolyte conductivity, the electrochemical window and the solubility of redox active species.[22,67–69] The solubility of the selected redox active species in the electrolyte and the cell voltage dictate the maximum achievable energy density, while electrolyte conductivity impacts achievable power densities in RFBs. The performance of aqueous RFB electrolytes are constrained by their electrochemical stability window, as well as the limited solubility of redox active species in water, which restricts achievable energy densities to < 50 Wh L^{-1} in most cases.[22,69] This has prompted research into the development of organic solvents as electrolytes, which boast wider electrochemical windows, enabling wider cell voltages to be achieved. However, commonly employed redox active materials have very limited solubilities in organic solvents.[70,71] Non-

aqueous RFBs also have reduced ionic conductivity compared to aqueous RFBs, limiting achievable power densities.[72,73] Additionally, organic solvents often present undesirable safety hazards such as high volatility and flammability. Thus, emerging research has focused on the design and development of novel, structured electrolytes that can simultaneously achieve high conductivity, wide electrochemical windows and high solubility of redox active species.[74–78]

Liquid-like nanoparticle organic hybrid materials (NOHMs) consist of a polymer canopy that is tethered to an inorganic nanoparticle core via ionic[40,79–81] or covalent bond[40,82], depending on the selection of the linker molecule. Owing to their negligible vapor pressure,[36] improved thermal-oxidative stability relative to the neat polymer canopy[36,37] and chemical tunability,[40] NOHMs have been extensively studied in the neat state for various energy storage[83–85] and gas separation applications.[36–38,40,43,80,82,86,87] More recently, this class of materials has been proposed as an emerging electrolyte additive in redox flow battery applications because of the potential for the functional groups along the polymer backbone to interact with and enhance the solubility of redox active species while maintaining high electrolyte conductivity.[75] The electrochemical behavior of Cu(II) ions in the presence of amine functionalized NOHMs have recently been reported.[75] Interestingly, the complexation between the amine functional groups and the Cu(II) ions was found to be tunable by the protonation state of the amine (i.e., the pH of the electrolyte), thus suggesting the capability of NOHMs to capture and subsequently release redox active species based on environmental stimuli.[75]

Though initial results suggest that NOHMs are promising for electrochemical applications, the structure of NOHMs in aqueous solutions containing supporting electrolyte is not yet fully understood. To design optimized electrolytes that can effectively capture and deliver target molecules (i.e., redox active species) to electrode surfaces, the structure and conformation of the

NOHMs' polymer canopy, in solution, needs to be elucidated further. In this work, the structure of NOHMs consisting of an SiO_2 nanocore and an ionically tethered polymer canopy of Jeffamine M2070, NOHM-I-HPE, in aqueous solution with and without supporting electrolyte (0.1 M $KHCO_3$) has been probed using small-angle neutron scattering.

Small-Angle Neutron Scattering (SANS) has been extensively used to characterize numerous polymer grafted nanoparticles.[46,58,88–92] In our study, SANS elucidates the structure, assembly and dispersion of NOHM-I-HPE in deuterated water. An NMR study on similar ionically tethered NOHMs samples identified two dynamic regions of the polymer in the NOHMs, where one timescale accounts for the grafted polymer whereas the other is consistent with the presence of untethered or free polymer.[93] Our SANS analyses shed further light on the conformation of the free polymer and its interaction with the grafted polymer layer structure. Moreover, the analysis of the NOHM-I-HPE solution with 0.1 M $KHCO_3$ salt clearly indicates an alteration in the structure of free and grafted polymer, which suggests a strong interaction between the salt, $KHCO_3$ and the nanoparticle surface. This interaction appears to alter the nature of the grafted layer and this translates to significant changes in the viscosity of the NOHM solutions with the added salt.

Experimental

Synthesis of NOHMs

NOHM-I-HPE was synthesized according to a previously reported procedure.[36,39,82,94] 18.3 g of a 30 wt.% colloidal suspension containing 7 nm diameter SiO_2 nanoparticles (LUDOX SM-30, Sigma-Aldrich) was diluted with deionized water to a final SiO_2 concentration of 4 wt.%. 30 g of a 35 wt.% 3-(trihydroxysilyl)-1-propane-sulfonic acid solution (acquired from Gelest Inc.) was diluted to a final concentration of 7 wt.%. After stirring both solutions for one hour, the SiO_2 suspension was then added dropwise to the silane solution. Then, 1 M NaOH was added dropwise

until a pH of 5 was reached and the resulting mixture was stirred and heated at 70 °C for 24 hours. Afterwards, the mixture was dialyzed against deionized water for 48 hours (SnakeSkin Dialysis Tubing 3500 MW cutoff, Thermo Scientific) to ensure the removal of any unbound silane molecules. The functionalized SiO_2 nanoparticles were then passed through a cation-exchange resin (Dowex Marathon C hydrogen form, Sigma Aldrich). During this step, the sulfonate groups on the linker molecules became protonated and any additional cations present in the solution were removed.

Next, Jeffamine M2070 (obtained from Huntsman Co.), an amine-terminated polyether with a molecular weight of 2000 g/mol, was tethered to the functionalized nanoparticles via an ionic bond. Jeffamine M2070 (referred to as HPE) was diluted in water to a concentration of 20 wt.% and then dropwise added to the functionalized silica nanoparticle solution until the equivalence point (pH = 6.5) was reached. This solution was then placed in a vacuum oven at 60 °C overnight to remove the excess water.

Small-Angle Neutron Scattering Experiments

For the SANS experiments, 30 wt.% SiO_2 nanoparticles were dissolved in H_2O whereas all NOHMs samples were dissolved in D_2O to achieve maximum contrast between the polymer and surrounding solvent. All the experiments were conducted at the National Institute for Standards and Technology's Center for Neutron Research using the NG-7 beamline with a Q range of 0.0042−0.41 $Å^{-1}$. Here Q is the wave vector = $4\pi/\lambda \sin(\theta)$, where λ is the neutron wavelength and θ is the scattering angle. Each sample was placed in a 1 mm thick demountable cell. Coherent scattering data was obtained by correcting the experimentally obtained scattering for sample transmission, empty cell and solvent scattering, and dark current background. This was then normalized to absolute units using a scattering standard using the NCNR SANS reduction

package.[95] All experimental scattering data are fit and analyzed using the SasView fitting program.[96] The errors related to the SANS analysis are obtained from the fitting of the SANS profile with the SasView software.

Viscosity Measurements

Before sample preparation, the NOHM-I-HPE was dried under vacuum at 60 °C for 3 hours to remove any absorbed moisture. Subsequently, mixtures of NOHM-I-HPE and deionized water were prepared using an analytical balance (ML104T, Mettler Toledo) with a precision of 10^{-4} g. The following wt.% NOHM-I-HPE samples were prepared: 10.0, 15.0, 20.0, 25.0, 30.0 and 40.0 wt. %. NOHM-I-HPE solutions with added salt (0.1 M $KHCO_3$, Sigma Aldrich, ACS, ≥99.0%) were prepared. Samples were mixed in 10 mL graduated flasks until complete dissolution of the salt was observed.

The dynamic viscosities of the prepared solutions were measured at 25.00 ± 0.05 °C using a piston-based viscometer (VISCOlab 4000, Cambridge Viscosity – PAC) equipped with a water bath (Julabo F12) for temperature control. The uncertainty in the viscometer measurements was determined to be within ±5% for all samples.

Results and Discussion

Small-angle neutron scattering (SANS) provides insight into the structure, assembly, and dispersion of the nanoparticle, polymer and solvent in nanoparticle organic hybrid materials (NOHMs). In particular, the contrast afforded by using deuterated solvent and protonated polymer allows the elucidation of the state of the polymer throughout the sample, whether it is tethered to the nanoparticle or free. The fitting of the scattering of the NOHM solutions requires a variety of fit parameters and being able to assign a value for any of these parameters aids in the analysis and

interpretation of the scattering patterns. With this in mind, the small-angle neutron scattering of a 30 wt.% solution of the SiO_2 nanoparticle dispersed in D_2O was measured and is shown in Figure 44 (pg. 172 in Appendix). This scattering curve is fit to a sphere model, which provides the size and scattering length density of the silica nanoparticle (r = 4.5 nm, SLD = 4.3 x 10^{-6} $Å^{-2}$) that serve as guides for these parameters in fitting the scattering of the NOHM solutions.

The SANS patterns of NOHM-I-HPE solutions in D_2O at loadings from 10-40 wt.% NOHM were measured and are shown in Figure 11. Inspection of the curves surprisingly shows that the scattering intensity *decreases* at low q ($q \lesssim 0.1$ $Å^{-1}$) with increased NOHM loading, but scattering intensity increases with NOHM loading at high q ($q \gtrsim 0.1$ $Å^{-1}$). This is unexpected because the scattering of a solution is directly proportional to the concentration of the solute, thus the scattering intensity of the curves should uniformly increase with NOHM loading if the structure of the solutions is not changing with concentration.

One explanation of this unanticipated result is that the *scattering contrast* between the nanoparticle and surrounding fluid is decreasing with increased NOHM loading. This, in turn correlates to the realization that there exists free (protonated) polymer in the surrounding (deuterated) solvent, which increases in loading with NOHM concentration. The presence of the free protonated polymer in the surrounding D_2O effectively lowers the contrast between the nanoparticle and surrounding fluid, decreasing the scattering intensity. Fitting of these curves to a core-shell sphere model combined with the polymer excluded volume model provides a detailed picture of the nanoparticle, conformation of the tethered polymer and free polymer, as well as penetration of free polymer into the tethered polymer canopy.

At the same time, fitting of the NOHMs scattering to a core-shell sphere model failed to capture the high-q portion of the data. However, the inclusion of the polymer excluded volume

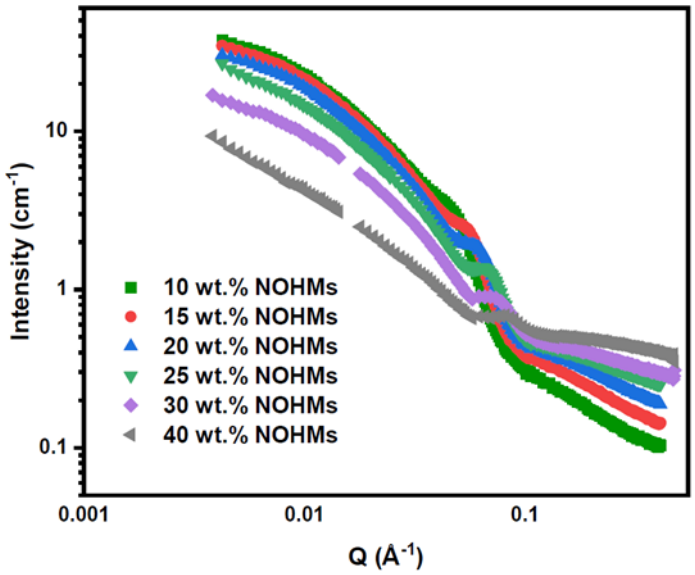

Figure 11. Small-angle neutron scattering curves of the NOHM-I-HPE solutions in D_2O with 10-40 wt.% NOHM loadings.

model to physically account for the presence of free polymer provides a robust model to fit the data as shown in Figure 45 (pg. 180 in Appendix). The square well and sticky hard sphere structure factors were used in the fitting with the core-shell sphere model for the form factor.[97,98] Table 12 (pg. 179 in Appendix) includes all the details of the combined model used for the fitting process. The functional form of a core-shell sphere model that describes NOHMs with a core-shell structure is provided in Equation 2.1.[63]

$$P(Q) = \frac{scale}{V}\frac{3}{V_s}\left[V_c(\rho_c - \rho_s)\frac{\sin(QR_c) - QR_c\cos(QR_c)}{Qr_c} + V_s(\rho_s - \rho_{solv})\frac{\sin(QR_s) - Qr_s\cos(QR_s)}{QR_s}\right] \quad \textbf{2.1}$$

Where, V_s is the volume of the NOHMs particle, V_c is the volume of the silica nanoparticle core. R_S is the radius of the NOHMs that includes the radius of the silica and the thickness of the shell (corona+canopy), R_c is the radius of the core, ρ_c is the SLD of the core, ρ_s is the SLD of the shell, ρ_{solv} is the SLD of the deuterated solvent.

The polymer excluded volume model describes the scattering from the polymer chains that are exposed to excluded volume effects and the functional form of the model is provided in Equation 2.2.[99]

$$P(Q) = \{\gamma\left(\frac{1}{2\nu}, U\right) - \frac{1}{U^{\frac{1}{2\nu}}}\gamma\left(\frac{1}{\nu}, U\right) \quad \textbf{2.2}$$

Where, γ is the incomplete gamma function, ν is the excluded volume parameter, U is a variable that is defined in terms of scattering vector, Q and includes the radius of gyration, R_g variable as described in Equation 2.3.

$$U = \frac{Q^2R_g^2(2\nu+1)((2\nu+2)}{6} \quad \textbf{2.3}$$

The fitting of the SANS curves to this model provides the diameter of the nanoparticles (~ 9 nm), the thickness of the grafted layer (corona + tethered canopy polymer), the radius of gyration of the free polymer in the solution, and the scattering length density (SLD) of the surrounding D_2O/polymer solution. Further analysis of the SLD of the surrounding fluid provides a measure of the amount of free polymer in the surrounding fluid. The presence of free polymer creates a surrounding fluid that is a solution of D_2O and Jeffamine M2070 polymer. Therefore, the SLD of the shell (tethered polymer) and the surrounding fluid varies from 0.517×10^{-6} Å^{-2} (SLD of pure polymer) to 6.35×10^{-6} Å^{-2} (SLD of pure D_2O). Completing this analysis on the series of NOHMs samples provides insight into the impact of increased NOHMs loading on the structure of the tethered layer, the conformation and concentration of the free polymer, and the interpenetration of the two.

Characteristics of Free Polymer

The amount of free polymer in solution between the nanoparticles can be determined by quantitatively analyzing the scattering length density of the surrounding solvent, which consists of D_2O and protonated polymer. The relationship between the measured scattering length density (SLD) and volume fraction of free polymer in the solvent (Φ_1) is given by Equation 2.4. In Equation 2.4, SLD_{poly} is the SLD of polymer = 0.517×10^{-6} Å^{-2}, SLD_{D2O} is the SLD of D_2O = 6.35×10^{-6} Å^{-2}, and SLD_{solv} is the SLD of the surrounding solvent, which is a mixture of the free polymer and D_2O. Figure 12 plots the volume fraction of free polymer in each NOHM solution (blue) as a function of NOHM concentration, as well as the percentage of polymer in the sample that is free in each solution (red).

$$\emptyset_1 = \frac{SLD_{solv} - SLD_{D_2O}}{SLD_{poly} - SLD_{D_2O}} \qquad \textbf{2.4}$$

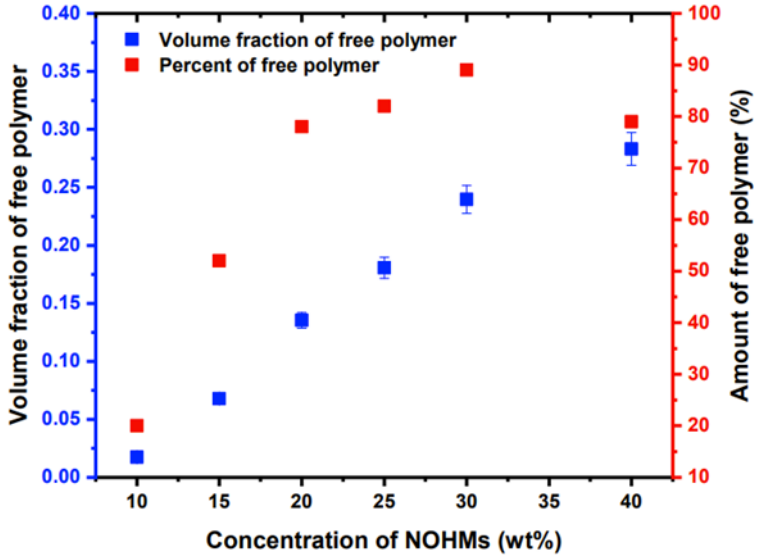

Figure 12. Increase in volume fraction and percentage of free polymer in solution with increasing NOHMs loading.

Inspection of Figure 12 shows that the volume fraction of free polymer increases steadily with NOHM loading, and that this corresponds to an increase in the percentage of polymer that is free in the NOHM solutions. This is surprising and emphasizes the importance of fully understanding the presence and consequence of free polymer, and its interaction with the tethered polymer, in the performance of NOHMs in functional applications. For instance, the grafting assuming all of the polymer is grafted to the nanoparticle is 2.0-2.5 chains/nm^2, however this decreases to 0.5-1.5 chains/nm^2 when accounting for free polymer.

A possible interpretation of these results is that as the loading of NOHMs increases, the distance between nanoparticles decreases and approaches the size of the tethered polymer. In this scenario, the "free polymer" is really just the tethered polymer spanning between nanoparticles. To test this, the interparticle distance between the surfaces of the nanoparticles (ID) is calculated and compared to the diameter of the free polymer. The ID is calculated with Equation 2.5, where d is the diameter of the nanoparticle and ϕ is the volume fraction of the nanoparticle.[100–102]

$$ID = d\left[\left(\frac{2}{\pi\,\phi}\right)^{\frac{1}{3}} - 1\right] \qquad \textbf{2.5}$$

Figure 13 plots the distance between the outer edge of the tethered polymers on neighboring nanoparticles and the diameter of the free polymer. Inspection of this figure clearly shows that the distance between nanoparticles is much greater than the size of the free polymer (or tethered nanoparticle as shown below), and thus the decrease in scattering length density of the solvent cannot be explained by the extension of the tethered polymer between nanoparticles. Thus, there must exist free polymer in the D_2O, where a large percentage of the polymer in the NOHM solution is not tethered to the polymer.

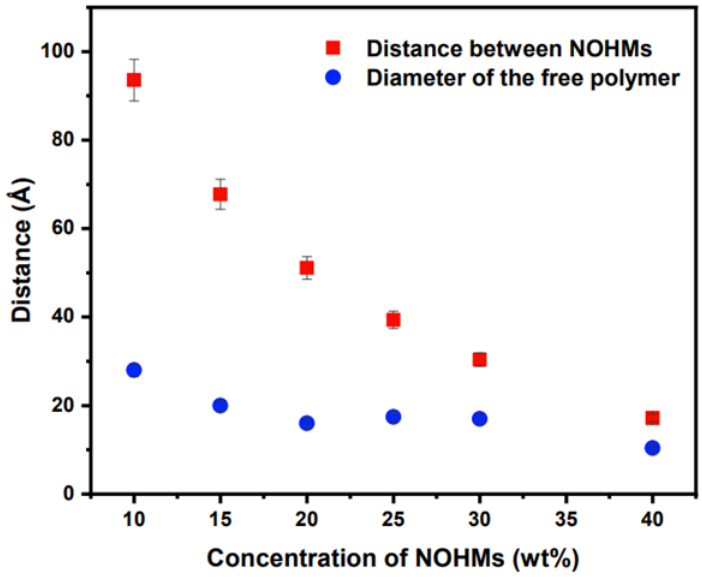

Figure 13. The interparticle distance of NOHMs and the size ($2R_g$) of the free polymer.

Moreover, as the NOHM concentration approaches 30 wt.%, the size of free polymer ($2R_g$) approaches the distance between two NOHMs nanoparticles. At these high loadings, the conformation of the free polymer appears to be constrained by the surrounding nanoparticle, creating a potentially anisotropic conformation that may impact ion or molecular transport in these materials.

The contrast afforded by the deuterated solvent and protonated polymer also provides a robust picture of the structure of the tethered polymer and the penetration of free polymer and solvent into the grafted canopy on the nanoparticle. Figure 14 plots the scattering length density of the grafted layer as a function of NOHM concentration, while Figure 15 plots the effective thickness of the grafted polymer layer as a function of NOHM concentration.

Figure 14 indicates that at low NOHMs loading, the tethered polymer is mostly solvated by D_2O, as the SLD at 10-15 wt.% is closer to that of D_2O than it is to the SLD of the polymer. As the NOHM concentration increases in the solution, the grafted layer may have collapsed or the free polymer penetrates into the grafted layer, both of which expels D_2O from the grafted layer lowering the scattering length density.

Inspection of Figure 15 shows that at low NOHM loading (~10-15 wt.%) the extension of the tethered polymer is similar to the R_g of the free polymer (Figure 13), suggesting that the tethered polymer is not distorted by the packing of the NOHMs or the presence of the free polymer. However, at higher NOHM loadings, the tethered layer thickness decreases dramatically, approaching values that are only a few Å thick. Clearly, it is not physically realistic that the tethered polymer only extends a few Å from the surface.

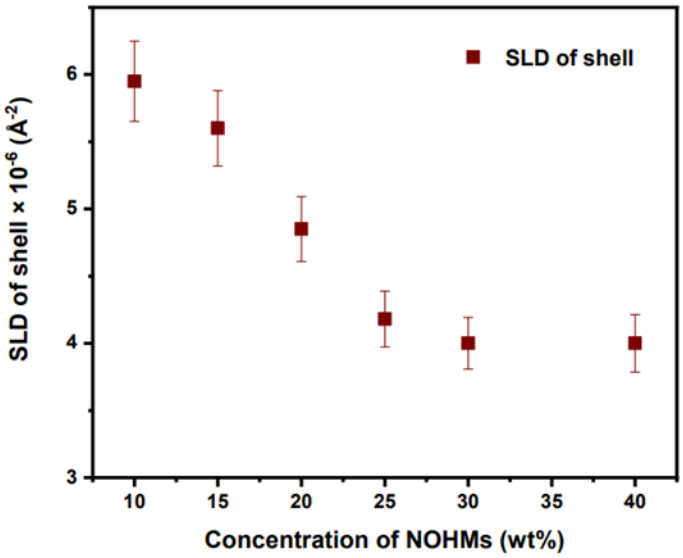

Figure 14. Decrease in scattering length density (SLD) of the grafted layer as a function of NOHMs loading.

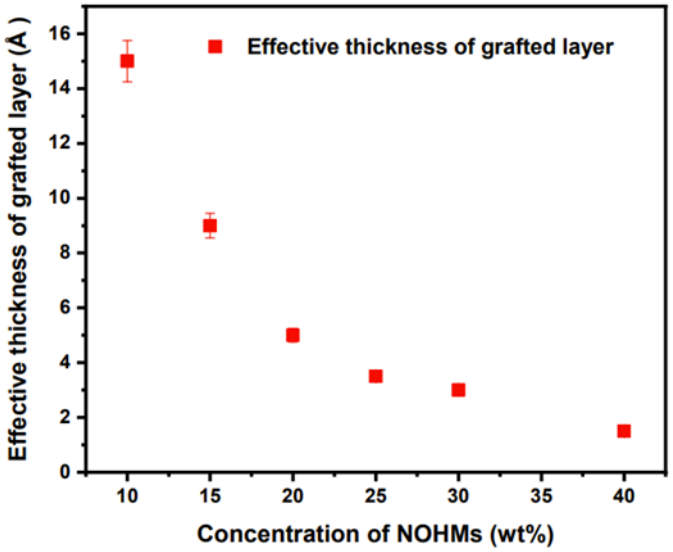

Figure 15. Change in the effective thickness of the tethered polymer with increasing NOHMs loading.

However, it must be remembered that neutron scattering contrast is dominated by the proton density in a layer and that the core-shell sphere model defines that portion of the grafted layer that has a different scattering length density of the surrounding fluid. Thus, our interpretation of this result is that the tethered polymer consists of two layers, one that is close to the nanoparticle that is only penetrated by D_2O and an outer layer of the tethered polymer that is penetrated by D_2O and the free polymer. This outer layer has a scattering length density that is very similar to that of the surrounding fluid (i.e., free polymer + D_2O), and therefore, is essentially invisible to neutrons. Thus, the values reported in Figure 15 are an effective thickness of the grafted layer and report that portion of the tethered layer that is not penetrated by the free polymer.

Figure 16 illustrates the emerging picture of the structure and assembly of the tethered polymer, free polymer, and nanoparticles in NOHM solutions based on these SANS results. The structure around a given nanoparticle surface consists of; i) tethered polymer: a polymer that is grafted (ionically bonded) to the functionalized silica nanoparticles, ii) interacting polymer: free polymer that penetrates the grafted layer, and iii) free polymer: polymer chains that exist in the bulk solution. Previous work by Vaia and co-workers that used NMR to monitor polymer chain dynamics in similar NOHM solutions demonstrates free unhindered polymer dynamics that is consistent with this interpretation.[93] Clearly, the structure and assembly of the free polymer, tethered polymer, and nanoparticles is quite complex, with a significant increase in free polymer chains that interact with the grafted polymer with increased NOHM loading. Moreover, it is clear that all aspects of this structure must be considered when interpreting the dynamic and functional properties of the NOHM solutions.

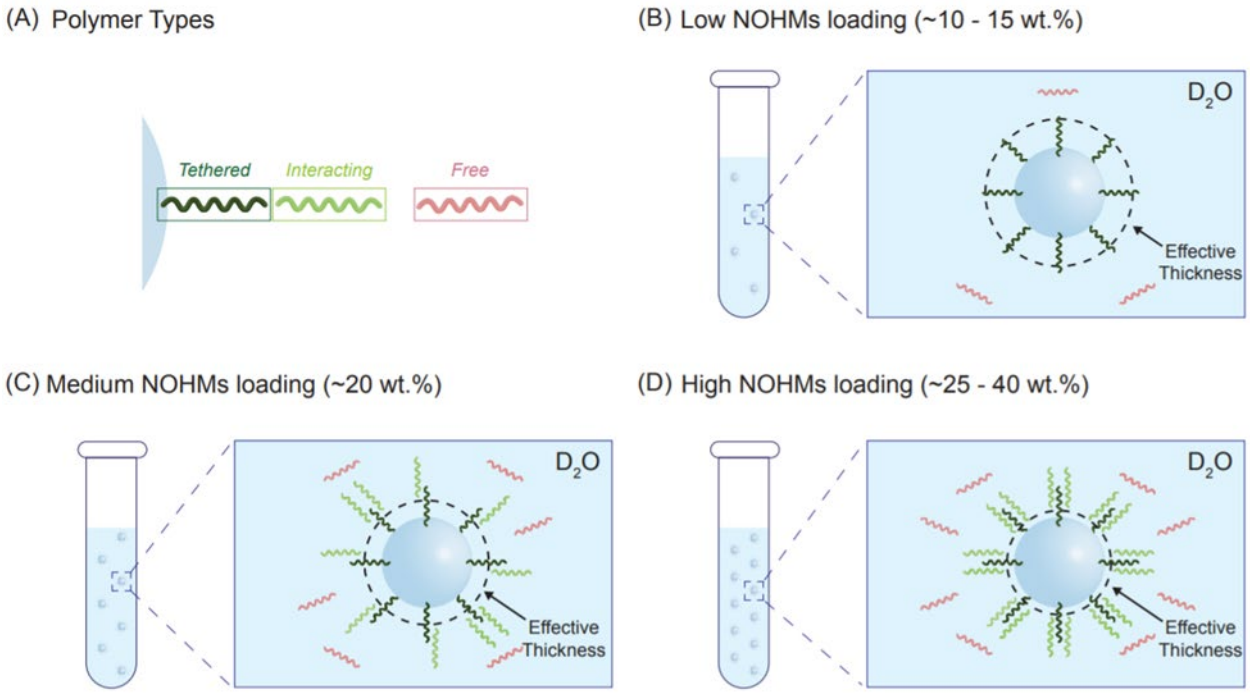

Figure 16. Schematic of NOHM-I-HPE structure at different loadings. Figure A shows three different polymer types in the solution, figure B, C, D shows decrease in effective thickness of grafted layer with increasing NOHMs loading.

Role of added salt on NOHM structure and assembly

The scattering curves of the NOHMs solutions with 0.1 M $KHCO_3$ are shown in Figure 46 (pg. 181 in Appendix). These curves are also fit to the combined model (core-shell sphere + polymer excluded volume) with the sticky hard sphere structure factor. Similar to the data shown in Figure 11, these data also have scattering intensities that *decrease* at low q ($q \lesssim 0.1$ Å^{-1}) with increased NOHMs loading, but increased scattering intensity with NOHMs loading at high q ($q \gtrsim 0.1$ Å^{-1}), indicative of the presence of free polymer in the NOHM solutions. Fitting these data to the combined core-shell sphere + polymer excluded volume form factors provides insight into the impact of the addition of the $KHCO_3$ salt on the structure of the grafted layer, the conformation and concentration of the free polymer, and the interpenetration of the grafted layer by interacting polymer.

Figures 17 and 18 plot the nominal thickness of the grafted layer and radius of gyration of the free polymer as a function of NOHM loading, respectively, for the NOHM solutions with and without the $KHCO_3$ salt. These data clearly show that the presence of the salt decreases the radius of gyration of the free polymer and increases the effective thickness of the grafted layer. Recalling that at these NOHM loadings, the effective thickness is interpreted to correspond to the portion of the tethered polymer that is not penetrated by interacting polymer, these results demonstrate that the presence of the salt limits the ability of the interacting polymer to penetrate the tethered polymer layer, while decreasing the global size of the free polymer.

It should be noted that there exists another interpretation that is consistent with this data; that the presence of the salt interrupts the ionic bonding of the canopy with the corona. In this scenario, the K^+ ion replaces the amine cation on the JEFFAMINE M2070 to release the polymer. This results in the grafted layer thickness corresponding to the corona (which is consistent with

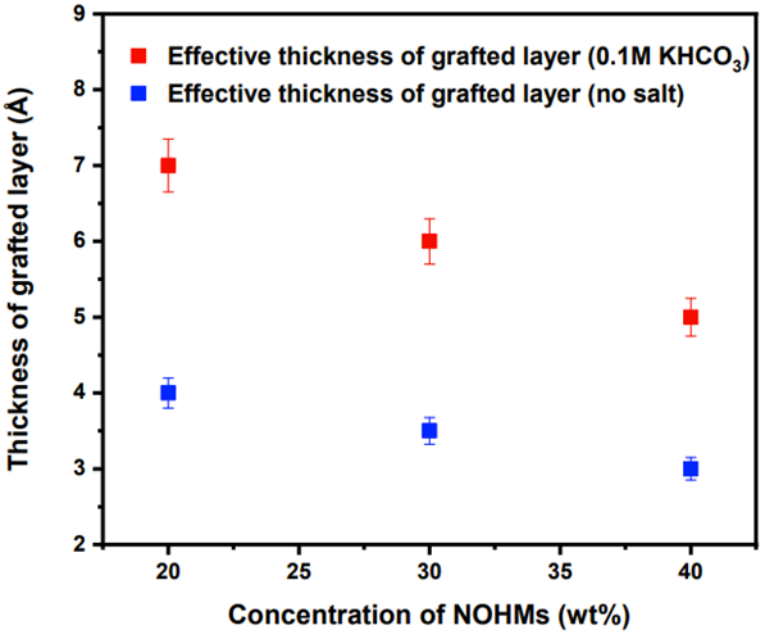

Figure 17. Change in effective thickness of grafted layer in salt and salt-free solution for 20 wt.%, 30 wt.%, 40 wt.% NOHMs solution.

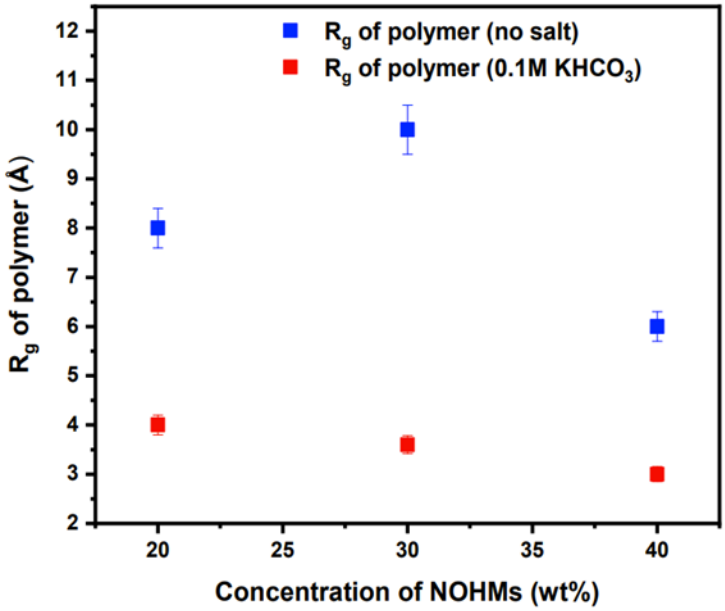

Figure 18. Change in R_g of free polymer in salt and salt-free solution for 20 wt.%, 30 wt.%, 40 wt.% NOHMs solution.

the data in Figure 17), which is surrounded by free polymer. This interpretation is also supported by work by Jespersen and co-workers on similar NOHM-I-HPE nanoparticles that showed that the addition of a supporting electrolyte changes the diffusion dynamics of the polymer because the electrolyte ions bond to the corona, freeing the HPE (Jeffamine M2070).[103]

Viscosity of NOHM solutions

Table 1 presents the viscosities of the NOHM-I-HPE solutions with and without $KHCO_3$, as well as the viscosity of Jeffamine M2070 solutions of similar concentrations. The addition of nanoparticles to the HPE solutions significantly increases the viscosity of the solution, which is not surprising.

It is interesting that the addition of salt to NOHMs solutions, however, produces a system that has a viscosity that is much more similar to that of the Jeffamine M2070 polymer solution than the viscosity of the NOHM solutions. Clearly, the addition of the salt dramatically decreases the interaction of the nanoparticle with the surrounding fluid. One possible mechanism is that the addition of salt interrupts the ionic bond that connects the canopy to the corona, which will create a smaller nanoparticle that results in a lower viscosity. This interpretation is consistent with literature results that show that the viscosity of covalently bonded NOHMs have a larger viscosity than ionically bonded NOHMs, which is ascribed to the slippage between the canopy and corona.[104] Thus, the viscosity data are consistent with the interpretation that the addition of salt creates a nanoparticle where the K^+ ion replaces the amine cation on the Jeffamine M2070 to release the polymer. This creates a system with fewer grafted polymer chains and lower viscosity.

Table 1. Viscosity measurements of the NOHM-I-HPE solutions with and without salt (The uncertainty in the viscometer measurements was determined to be within ±5% for all samples.)

Concentration (wt.%)	**Jeffamine M2070 Polymer (cP)**	**NOHM-I-HPE without salt (cP)**	**NOHM-I-HPE with 0.1M $KHCO_3$ salt (cP)**
10	2.14	4.39	1.95
15	4.6	9.83	3.08
20	6.79	21.8	5.55
25	10.05	41.59	5.81
30	14.48	76.18	14.67
40	21.39	313	35.87

Conclusion

Small-angle neutron scattering experiments provide valuable insight into the structure and dispersion of NOHMs in aqueous solution with and without the presence of supporting electrolyte, 0.1 M $KHCO_3$ salt. A decrease in scattering intensity with increasing NOHMs loading is interpreted to indicate the presence of free polymer in the solution. Further quantitative analysis shows that a large portion of the polymer is free in solution and not bound to the functionalized nanoparticles. The careful analysis of the scattering patterns shows that the effective thickness of the grafted layer decreases with increased NOHMs loading, indicating that the free polymer penetrates the grafted layer structure at high NOHMs loading. Thus, the structure of the NOHM must be viewed as consisting of three distinct types of polymers: tethered polymer, interacting polymer and free polymer in solution. The addition of a supporting electrolyte in the solution, however, also alters the conformation of the grafted layer and free polymer. The grafted polymer layer increases in thickness, while the global size of the free polymer decreases with addition of salt. Comparison of these structural studies to their viscosity strongly suggests that the addition of salt provides a cation that may compete with the amine of the tethered polymer in the canopy, replacing the tethered polymer and detaching the polymer from the nanoparticle. Thus, these results provide crucial information on the structure and assembly of the tethered polymer, interacting polymer, free polymer, and nanoparticle in NOHM solutions and their variation with the addition of the supporting electrolyte. These results provide an important structural foundation for the rational improvement of the performance of NOHMs in functional applications, such as an electrolyte additive in flow batteries.

Acknowledgement

This work was supported as part of the Breakthrough Electrolytes for Energy Storage (BEES), an Energy Frontier Research Center funded by the U.S. Department of Energy, Office of Science, Basic Energy Sciences under Award # DE-SC0019409. We acknowledge the support of the National Institute of Standards and Technology, U.S. Department of Commerce, in providing the neutron research facilities used in this work.

Chapter III Insights into the Assembly and Conformation of Nanoparticle Organic Hybrid Materials (NOHMs) in Solution with the Change in Grafting Type

A version of this chapter was originally published by Tony G. Feric, Sara T. Hamilton, Md Ashraful Haque, Javad Jeddi, Joshua Sangoro, Mark D. Dadmun Ah-Hyung Alissa Park:

Tony G. Feric, Sara T. Hamilton, Md Ashraful Haque, Javad Jeddi, Joshua Sangoro, Mark D. Dadmun Ah-Hyung Alissa Park; "Impacts of Bond Type and Grafting Density on the Thermal, Structural, and Transport Behaviors of Nanoparticle Organic Hybrid Materials-Based Electrolytes." *Adv. Funct. Mater.* **2022**, *32*, 2203947.

Md Ashraful Haque performed all the SANS experiments and analyses. Tony G. Feric and Sara T. Hamilton synthesized NOHM-I-HPE and NOHM-C-HPE nanoparticles and measured viscosities of the solutions.

Abstract

Recently, nanoparticle organic hybrid materials (NOHMs) have been considered as novel electrolytes for energy storage applications due to their unique properties, which include good thermal stability, negligible vapor pressure and easy synthesis. To deploy NOHMs in energy storage systems, it is essential to be able to correlate the structural features of NOHMs to their performance in electrochemical systems. Hence, in this study, we investigate the impact of grafting type (ionic vs covalent) on the structure and performance of NOHMs that consists of a silica core and grafted HPE polymer (Jeffamine M2070) in aqueous solution with and without the presence of supporting electrolyte (0.1 M $KHCO_3$) using small-angle neutron scattering (SANS). Our previous study investigated similar ionically bonded NOHMs with a grafting density of 2.0-2.5 chains nm^{-2}, where these studies show that a significant portion of polymer detaches from the functionalized surface, altering the assembly and structure of NOHMs in solution. These studies elaborate our understanding of the impact of graft type on the structure and assembly of NOHMs

in aqueous solutions, with all NOHMs having a similar polymer grafting density. The careful analyses of these studies indicate that even at low grafting density (0.8 chains nm^{-2}) and concentration (1-3 wt.%), ionic NOHMs solutions contain free polymer that can interact with the grafted polymer, altering the assembly of NOHMs in solution. Our investigation also elucidates that the covalent NOHMs solutions consist of both aggregated and dispersed NOHMs in the solution. Unlike ionic NOHMs, the functionalization of covalent NOHMs does not allow polymer to detach from the nanoparticles surface and hence the grafted layer density of the covalent NOHMs structure is preserved. Moreover, the addition of supporting electrolyte affects the assembly and structure of polymer in the ionic NOHMs solution significantly, whereas the conformation of the polymer grafted to the covalent NOHMs varies only slightly with the addition of salt. These conformational changes alter the performance of NOHMs solution resulting in a dramatic change in viscosity. Careful analysis shows that this significant alteration of solution viscosity in the ionic NOHMs can be traced back the presence of the free polymer that interacts with the grafted layer, and the attenuation of this interaction between free and grafted polymer with the addition of salt. Thus, these studies elucidate the impact of grafting type on the overall structure, assembly, and performance of functionalized NOHMs in aqueous solution, where the difference between ionically grafted NOHMs and covalently grafted NOHMs is significant and must be considered when designing functional systems that incorporate NOHMs.

Introduction

The need to reduce carbon emissions and fossil fuel usage to prepare for a sustainable future has motivated current researchers to search for environment-friendly alternatives for energy production and storage. The use of renewable energy can relieve some of the demand of fossil fuels and consequently can reduce our carbon footprint in nature.[105,106] However, the intermittency

of renewable energy has challenged the successful utilization of this source in the existing power-grid.[107,108] Hence, energy storage systems, such as redox flow batteries (RFB), are needed to harness the production of renewable energy sources.[109,110] There are several limitations of redox flow batteries including conductivity, solubility of redox species and a narrow electrochemical window that require attention to realize their potential.[69,111,112] The rational design of novel electrolytes can play a key role in overcoming these limitations of RFBs. For instance, ionic liquids (ILs),[110,113–115] microemulsion,[116–119] and deep eutectic solvents (DESs)[120–122] have recently gained attention as candidates to deploy as novel electrolytes in energy storage systems for their attractive properties. Nanoparticle organic hybrid materials (NOHMs) are also an interesting candidate as novel electrolytes that have gained attention for their unique properties including negligible vapor pressure,[36] high thermal stability[37,39,123] and tunable chemistry.[40,124]

Nanoparticle organic hybrid materials (NOHMs) consist of an inorganic core with an organic polymer canopy grafted to the core ionically or covalently. This class of polymer grafted nanoparticles has been extensively studied and have been shown to improve the performance of lithium batteries[84,125,126] and to efficiently capture CO_2 at large capacity.[36,79,86,123,127–129] Moreover, the opportunity to alter the ligand chemistry,[129] the corona connectivity[40,82] and the nanoparticles[42] offers tunability in the performance of NOHMs, making them an attractive choice for energy storage systems. However, NOHMs suffer from high viscosity that can limit their performance and often requires them to be used as additives in solution in an electrochemical system.[36,130,131] Solubilizing NOHMs in an aqueous solution reduces the viscosity significantly,[36] potentially overcoming an apparent barrier of the use of NOHMs as an electrolyte. However, solubilizing the NOHMs can alter the structure and assembly of the NOHMs, and correlating these structural characteristics to performance is needed to effectively implement them in energy storage systems.

This is essential as the transport and structural properties of electrolytes have been shown to dictate the overall electrochemical performance.[78,132–135]

Recently, NOHMs solutions have been extensively investigated to develop an understanding of their structure and transport mechanism in energy storage systems. These studies show that factors such as pH, salt , solvent polarity and NOHM concentration can significantly impact the conformation, assembly, and ordering of ionic NOHMs.[75,130,131,136] For instance, Hamilton et. al. have studied the effect of pH on ionic NOHMs solutions and showed that the complexation of Cu^{2+} with the polymer canopy can be altered by tuning the pH of the system.[75] Moreover, Hamilton et. al. also showed in a different study that the polymer conformation of ionic NOHMs can be altered by adding and removing salt (ionic stimulus) in the solution.[131] Feric et. al. have highlighted the effect of the structure of the secondary solvent on the performance of ionic NOHMs and showed that the interaction of the polymer with the nanoparticle surface can be modified by the different secondary fluids.[130] In our previous study using small-angle neutron scattering (SANS) experiments, we investigated the structure and assembly of a series of ionic NOHMs in aqueous solution with NOHMs loadings of 10 - 40 wt.%.[136] These results showed that the aqueous solutions of NOHMs with a grafting density of 2-2.0 chains nm^{-2} have a significant amount of free polymer in the solution at these concentrations. The free polymers in solution can interact with the grafted polymer and thus, changes the molecular assembly of the polymer near the nanoparticle surface. To expand our understanding of NOHMs in functional applications, we have completed similar experiments on NOHMs that have the polymer covalently bound to the nanoparticle, where a tethering-untethering process is precluded. The experiments on covalently bound NOHMs elucidate the importance of the grafting type, and thus the tethering-untethering

equilibrium of the grafted polymer, the structure of NOHMs based fluids, as well as the impact of added electrolyte on their structure and performance.

Thus, we have investigated the structure and assembly of NOHM-I-HPE$_{0.8}$, NOHM-C-HPE$_{0.5}$, NOHM-C-HPE$_{0.7}$ (grafting densities are included as subscript), which have an inorganic silica core and grafted HPE (Jeffamine M2070) canopy at identical concentrations using small angle neutron scattering (SANS). SANS offers information on the conformation of the free and grafted polymer, as well as the structure of the grafted layer.

Investigating the structure and assembly of the ionic and covalent NOHMs offers insight into the dispersion and conformation of grafted and free polymer in the NOHMs aqueous solution. Additionally, our results document the impact of added salt on the conformation of the free and grafted polymer and how this assembly subsequently impacts the viscosity of the solution. A small portion of the SANS results of this study has been reported.[137] However, in this study, we provide a more complete analysis of the small angle neutron scattering results to deduce the impact of grafting type on the complex assembly of NOHMs in aqueous solution.

Experimental

Synthesis of Ionically bound NOHMs (NOHM-I-HPE)

NOHM-I-HPE was synthesized to a targeted grafting density (0.8 chains nm^{-2}) using a process similar to that reported previously.[36,39,79,82,94,128,130] In short, a 1 wt.% solution of the ionic linker, 3-(trihydroxysilyl)-1-propane-sulfonic acid (Gelest Inc.) was added to a 4 wt.% SiO_2 nanoparticle (LUDOX SM-30 obtained from Sigma-Aldrich) solution in a dropwise manner. The resulting surface coverage of silica nanoparticles is expected to be ≈1.0 chains nm^{-2} after the addition of the ionic linker. Then, the pH of the solution was adjusted to 5 by the addition of 1 M

NaOH in the solution and subsequently, the solution was stirred at 70 °C for 24 h. The functionalized silica nanoparticles were then passed through a cation exchange resin (Dowex Marathon C hydrogen form, Sigma Aldrich) to protonate the linker molecules and remove any excess cations. 20 wt.% Jeffamine M2070 polymer (MW = 2000 g mol^{-1}, acquired from Huntsman Co., referred to as HPE) was added dropwise resulting in grafting density of 1.0 chains nm^{-2}, prior to sample purification. After mixing overnight at room temperature, the solution was dialyzed for at least 48 h (SnakeSkin Dialysis Tubing 10K MW cutoff, Thermo Scientific) to remove any untethered polymer, with frequent water changing. To confirm the removal of excess water, the solution was placed in an oven at 60 °C overnight.

Synthesis of Covalently bound NOHMs (NOHM-C-HPE)

A previous protocol was also used to synthesize NOHM-C-HPE at the targeted grafting densities.[36,40,82] In this process, 3 wt.% of HPE dissolved in ethanol is mixed with 3 wt.% of (3-glycidyloxypropyl) trimethoxysilane (acquired from Gelest Inc. and referred to as GPC) in ethanol. To complete the reaction between the HPE chains and the GPC linker, the mixture was then stirred at 50 °C for 12 hrs. After the completion of the reaction, a distillation process was used to remove the ethanol resulting in the functionalized HPE polymer. The HPE polymer was then dissolved in deionized water to a concentration of 7 wt.% that was then mixed with 3 wt.% of silica nanoparticles (LUDOX SM-30 obtained from Sigma-Aldrich). Similar to the NOHM-I-HPE synthesis, the mixture of HPE polymer and silica nanoparticles was then left overnight to mix. The mixture then went through a 48 h dialysis process. To remove excess water, the mixture was left in a vacuum oven overnight at 60 °C .

Small-Angle Neutron Scattering

The samples of 1 wt.% and 3 wt.% of NOHM-I-HPE$_{0.8}$, NOHM-C-HPE$_{0.5}$, NOHM-C-HPE$_{0.7}$ and 1 wt.% and 5 wt.% of HPE were prepared by dissolving in D_2O. Samples of NOHM-I-HPE$_{0.8}$, NOHM-C-HPE$_{0.5}$, NOHM-C-HPE$_{0.7}$ and HPE at identical concentrations were also prepared by dissolving in D_2O with added 0.1 M $KHCO_3$ salt. The SANS experiments were performed at a Q range of 0.001–0.8 Å at the HFIR CG-2 GP SANS beamline located at the Oak Ridge National Laboratory. The wave vector, Q, is $= 4\pi/\lambda \sin(\theta)$, where λ is the neutron wavelength and θ is the scattering angle. The coherent scattering profiles were obtained using the Jupyter software program that corrected for the empty cell scattering, thickness of the cell, transmission of the sample, and solvent scattering. The small angle scattering analysis software package SasView was used to fit and analyze the scattering profiles of the HPE, NOHM-I-HPE, and NOHM-C-HPE solutions.[138] The errors related to the SANS analyses are obtained from fitting the SANS profiles with the SasView software.

Viscosity

The viscosity of aqueous solutions of HPE, NOHM-I-HPE, and NOHM-C-HPE with and without the presence of salt (0.1 M $KHCO_3$), were measured using a VISCOlab 4000 (Cambridge Viscosity – PAC) viscometer. This viscometer can measure viscosities from 0.2 to 10000 cP. While measuring the viscosity of the samples, the temperature was controlled at 25.00 ±0.05 °C using a water bath (VWR 1166D). The error in viscosity was within ±5% for all the samples.

Discussion and Results

Impact of grafting type (Ionic vs Covalent) on the Structure and Assembly of NOHMs in aqueous solution

Conformation of HPE polymer in Solution

The structure and conformation of the polymer in solution without nanoparticles is examined first to provide a basis to understand the impact of the nanoparticle on the structure and assembly of the free polymer. The SANS profiles of 1 wt.% and 5 wt.% HPE in D_2O are shown in Figures 19 and 47 (pg. 181 in Appendix), respectively. These figures also show the fits of the data to the polymer excluded volume model, from which the radius of gyration (R_g) and Porod exponent (which correlates to the mass fractal dimension of the polymer chain) can be determined. The mass fractal dimension documents the compactness of the polymer chain over length scales below the radius of gyration (R_g) and above the statistical length (b) of the polymer, and corresponds to a q range of $1/R_g < q < 1/b$.[139] The fractal dimension is often correlated to the Flory exponent where the fractal dimension scales inversely to the Flory exponent. The Flory exponent provides insight on the conformation of the polymer in a solvent, where a Flory exponent, $\nu = 0.5$, refers to a theta solvent in which a polymer follows a random walk conformation and $\nu = 0.33$ refers to poor solvent and a collapsed polymer chain.[140] Table 2 shows the radius of gyrations and Flory exponents of the HPE polymer in aqueous solution that emerge from this fitting process. These results indicate that the radius of gyration of the polymer varies from ~17 to ~12 Å. Moreover, the Flory exponent shows that the polymer chain is not expanded in water. From the Flory exponent values, it is evident that water is a theta solvent ($\nu = 0.5$) for the HPE polymer, and the polymer follows a random walk model. With the addition of salt, the Flory exponent decreases indicating that the polymer chain collapses, consistent with the decrease in R_g. This conformational analysis of HPE

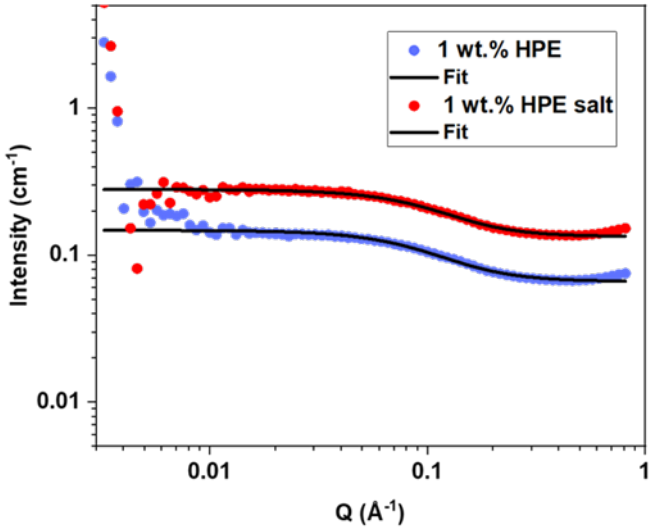

Figure 19. SANS profile fit of 1 wt.% HPE in aqueous solution with and without salt. The 1 wt.% salt solution scattering profile and fit is scaled for clarity.

Table 2. Radius of gyration (R_g) and Flory exponent (ν) of HPE polymer in aqueous solution obtained from polymer excluded volume fits of the SANS curves.

Sample	R_g (Å) ± 1 Å	Flory exponent, ν
1 wt.% HPE	17	0.50
1 wt.% HPE 0.1 M $KHCO_3$ salt	15	0.39
5 wt.% HPE	13	0.50
5 wt.% HPE 0.1 M $KHCO_3$ salt	12	0.41

polymer provides a foundation to interpret the scattering analysis of the NOHMs solutions more fully.

Structure of ionic NOHMs in solution

With the goal of understanding the impact of grafting bond type on the structure and assembly of NOHMs in solutions, the neutron scattering profile of NOHM-I-HPE and NOHM-C-HPE with similar grafting density and concentration were measured. In our previous study of the structure of ionically bonded NOHMs in solution (NOHM-I-HPE$_{2\text{-}2.5}$), the scattering profiles of the solutions showed a decrease in intensity at low Q ($Q \lesssim 0.1$ Å^{-1}) and an increase in intensity at high-q ($Q \gtrsim 0.1$ Å^{-1}) with increasing concentration of NOHMs, which is a result of the presence of free polymer.[136] The NOHM-I-HPE used in this previous work had a grafting density of 2.0-2.5 chain nm^{-2} corresponding to a significant amount of free polymer. However, in order to compare the structure and assembly of similar ionic and covalent NOHMs solutions, it was necessary to decrease the grafting density and decrease the NOHM concentration due to the limited miscibility of the covalent NOHMs in solution. Thus, the SANS profile of covalent and ionic NOHMs at 1 wt.% and 3 wt.% with grafting densities of 0.5-0.8 chains nm^{-2} were collected. Figure 20 shows the scattering profile of 1 wt.% and 3 wt.% NOHM-I-HPE with a grafting density of 0.8 chains nm^{-2}. Initially, only the core-shell sphere model with a square well structure factor was used to fit the scattering profile. However, this model fails to fit the full scattering profile of these samples. However, inclusion of the polymer excluded volume model with the core-shell sphere model captures the whole scattering profile. This is similar to our previous studies and indicates that the solution consists of NOHMs as well as free polymer in solution. The fits of the SANS profiles of 1 wt.% and the 3 wt.% NOHM-I-HPE$_{0.8}$ to this model are provided in Figure 48 (pg. 182 in Appendix). In the analysis of the data with this model, the radius (~4.5 nm) and the

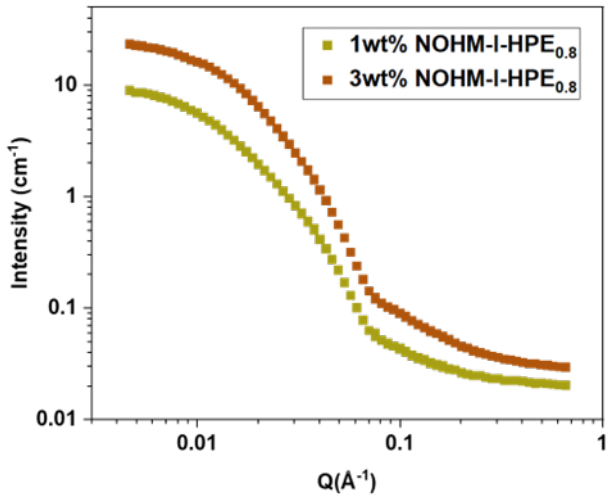

Figure 20. Small-angle neutron scattering profile of 1 wt.% and 3 wt.% NOHM-I-$HPE_{0.8}$ in aqueous solution.

scattering length density of the silica nanoparticle (~4.4E-06 $Å^{-2}$) are kept constant. The scattering length density of the grafted layer and the solvent, the thickness of the grafted layer and the radius of gyration of the free polymer are then fitted in the analysis. The results of this successful fitting process provide valuable information on the structure and assembly of the NOHM-I-HPE and free polymer in solution, including the conformation of the free polymer and concentration dependence of the thickness of the grafted layer of NOHM-I-$HPE_{0.8}$. Figure 21 shows a graphical representation of the structure and assembly of free polymer and grafted free polymer in these NOHM-I-HPE solutions. Figure 22 plots the thickness of the grafted layer and the radius of the gyration of the free polymer at both 1 wt.% and 3 wt.% loadings. The result shows that the thickness of the grafted layer and the radius of gyration of the free polymer are very similar ~13-14 Å. The R_g of the polymer in solution at 1 wt.% has been measured to be 17Å, indicating that the presence of the nanoparticle in solution collapses the polymer chain slightly. The model also provides insight into the amount of free polymer that is present in the NOHM-I- $HPE_{0.8}$ solution. Equation 3.1 shows the analytical relationship between the concentration of free polymer and the experimentally measured scattering length density (SLD) of the solvent in the NOHMs samples.

$$\emptyset_1 = \frac{SLD_{solv} - SLD_{D_2O}}{SLD_{poly} - SLD_{D_2O}} \qquad \textbf{3.1}$$

In Equation 3.1, (Φ_1) is the volume fraction of free polymer in the solvent, SLD_{poly} is the SLD of polymer = 0.517E-06 $Å^{-2}$, SLD_{D2O} is the SLD of D_2O = 6.35E-06 $Å^{-2}$, and SLD_{solv} is the experimentally determined SLD of the solvent, which is a mixture of the free polymer and D_2O. Using Equation 3.1, the volume fraction of free polymer in the solvent is determined to be 0.005 (±.00025). This corresponds to an average of 42 vol.% of the polymer present in the sample being free polymer. This indicates that a significant portion of the free polymer is present in the 1 wt.% and 3 wt.% NOHM-I-$HPE_{0.8}$ aqueous solutions.

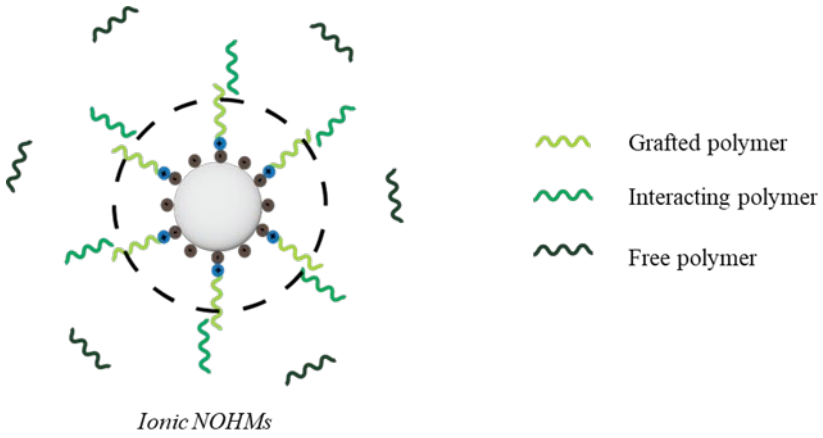

Figure 21. Illustration of the structure and assembly of free polymer and grafted polymer in NOHM-I-HPE solution.

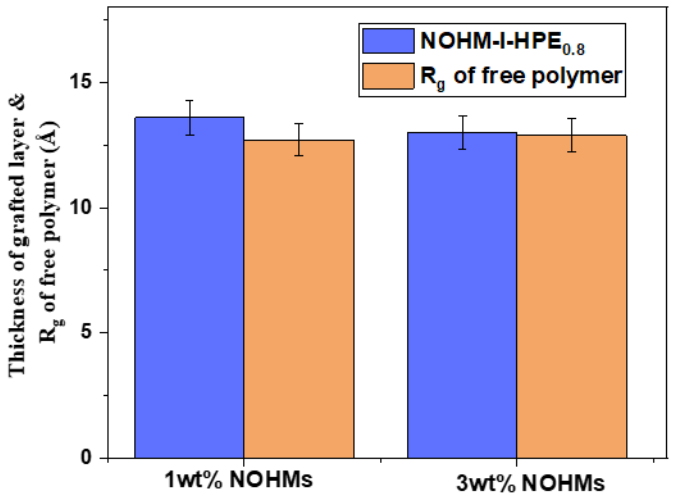

Figure 22. Thickness of grafted layer of NOHM-I-HPE$_{0.8}$ and R_g of free polymer.

Moreover, our previous studies clearly demonstrated that the free polymer penetrates and interacts with the grafted layer at NOHMs loadings above 15 wt.%.[136] However, in these studies, the similarity of the R_g of the grafted layer and that of the free polymer indicates that at these lower NOHMs concentrations, there is minimal impact of the presence of the free polymer on the conformation of the grafted layer.

Structure of Covalent NOHMs in solution

To provide insight into the impact of the grafting type on the structure and assembly of the NOHMs in aqueous solution, the SANS profiles of the covalently bound NOHMs are similarly analyzed. Figure 23 compares the 1 wt.% and 3 wt.% NOHM-C-HPE scattering profiles to those of the NOHM-I-HPE solutions. Figure 23 shows the scattering intensity of the NOHM-C-HPE solutions are higher than that of NOHM-I-HPE, indicating the presence of aggregates in the NOHM-C-HPE solution. This is verified by the fact that the core-shell model no longer fits the scattering of the covalently bound samples. In fact, fitting the scattering profile of covalent NOHMs using only the fractal model does not capture the scattering over the entire Q range, especially at high q ($0.08\ Å^{-1} < Q < 0.1\ Å^{-1}$), which corresponds to length scales of ~62-78 Å. The excess scattering at these length scales is consistent with the presence of *dispersed individual* covalent NOHMs particles in the solution. Therefore, a scattering model that combines fractal core-shell (aggregates) and core-shell spheres (individual NOHMs) is used to capture the total scattering of covalent NOHMs solutions. Figure 24 show SANS profiles and the fits to this model of the 1 wt.% and 3 wt.% NOHM-C-HPE aqueous solution at different grafting densities. The analysis of the scattering curves by this fitting process documents the extent of aggregation of the NOHM-C-HPE in solution. The fitting process also provides mass fractal

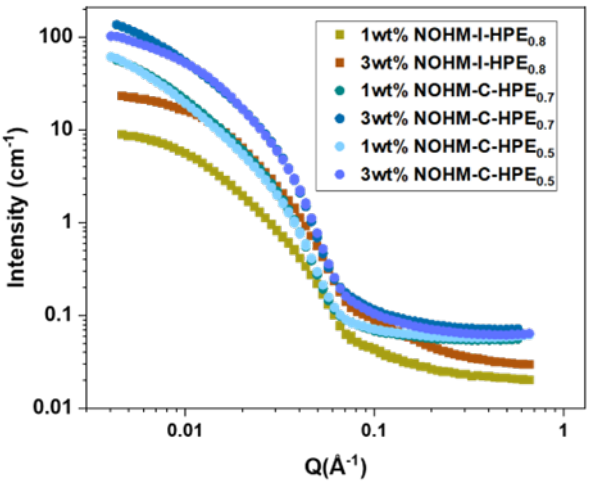

Figure 23. Small-angle neutron scattering profile of 1 wt.% and 3 wt.% NOHM-I-HPE0.8, NOHM-C-HPE0.7, NOHM-C-HPE0.5 in aqueous solution.

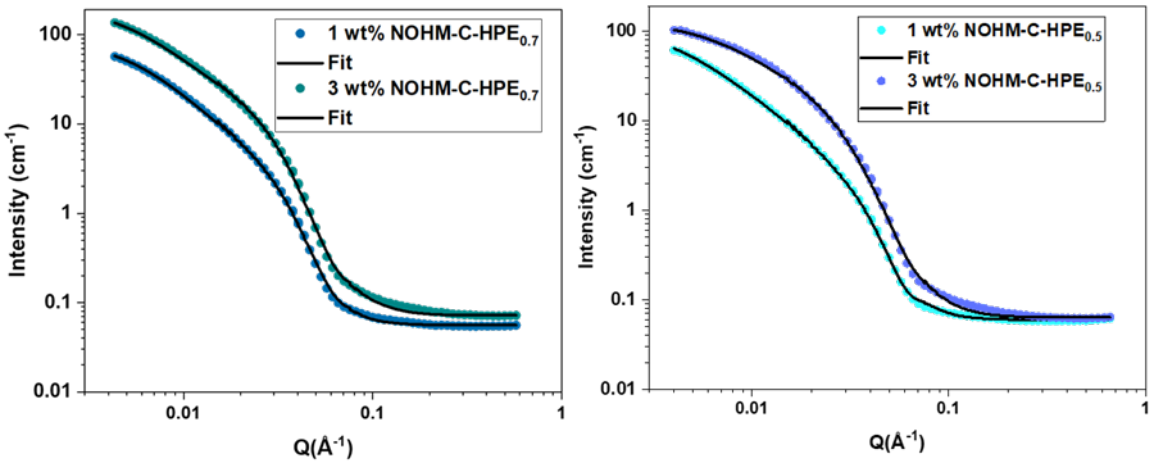

Figure 24. SANS profile fit of 1 wt.% and 3 wt.% NOHM-C-HPE0.7 (left) and NOHM-C-HPE0.5 (right) in aqueous solution.

dimension of the aggregates, which correlates to the compactness of the aggregates. Figure 25 illustrates the correlation between mass fractal dimensions and compactness of the aggregates. The mass fractal dimension can range from 1 to 3 where 1 corresponds to linear aggregates, whereas 3 refers to condensed compact aggregates.[141,142] The fractal dimension of the covalent NOHMs aggregates in solution is ~2.5, indicating the aggregates are quite compact, but not completely collapsed. This aggregation clearly impacts the dispersion and mobility of the covalent NOHMs particles in the solution. The fitting analysis of the covalent NOHMs solutions reveals that the SLD of the solvent is equal to that of D_2O (6.35E-06 $Å^{-2}$) and does not vary with NOHM concentration. This indicates that there is *no free polymer* in the covalent NOHMs solution, in contrast to the ionic NOHM solutions. The fitting analysis of the scattering also provides information on the grafted layer thickness of the covalent NOHMs particles in this solution, where Figure 26 plots the thickness of the grafted layer, showing that the length of the grafted NOHM-C-HPE polymer is ~21 Å. It is well known that grafting density can significantly impact the grafted polymer height. At different grafting densities, the polymer can attain different conformations. At low grafting density, the polymer are relaxed in the mushroom region, which shifts to a semi-dilute polymer brush conformation at intermediate grafting densities. Further packing of grafted polymer onto the surface forces an extended polymer brush conformation at high grafting density.[143] This study does not focus on the variation in polymer conformation with grafting density, but rather highlights the conformation of the polymer with the change in graft type. However, a study by McDonald et al. on similar covalent NOHMs suggests that the polymer chain with a grafting density of less than 0.8 chains nm^{-2} attains a mushroom conformation. [46] In this study, the maximum grafting density of covalent NOHMs is 0.7 chains nm^{-2} and, would suggest that our grafted polymer is in a relaxed state. Figure 27 clearly shows the role of the grafting type

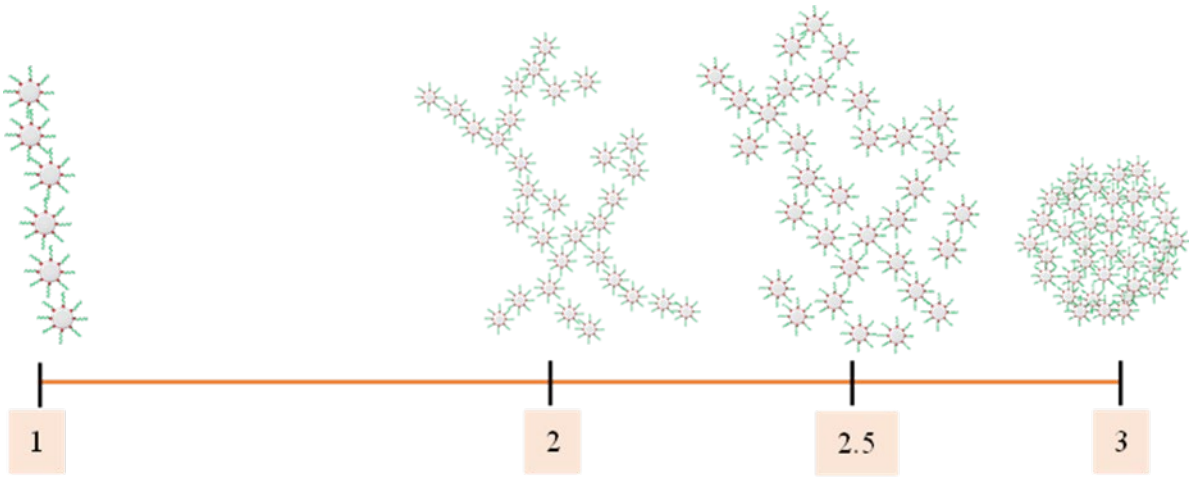

Figure 25. Illustration of aggregation of covalent NOHMs at different mass fractal dimensions. Fractal dimension 1 corresponds to linear aggregates, whereas 3 refers to condensed compact aggregates. Fractal dimension of NOHM-C-HPE solution ~2.5 corresponds to compact but not completely collapsed aggregates.

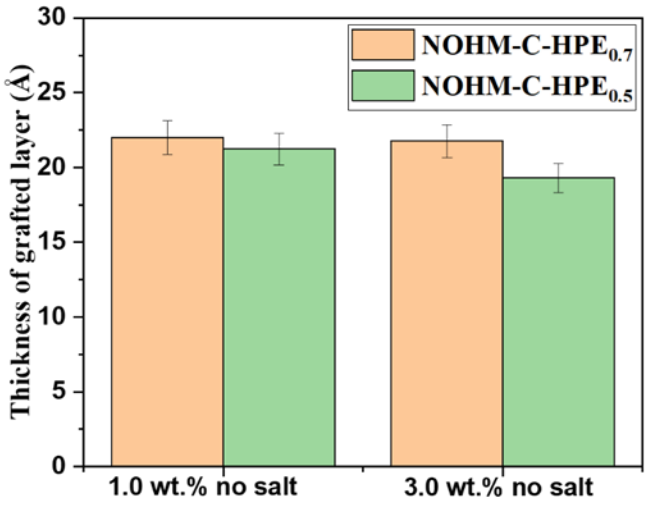

Figure 26. Thickness of grafted layer of NOHM-C-HPE in aqueous solution.

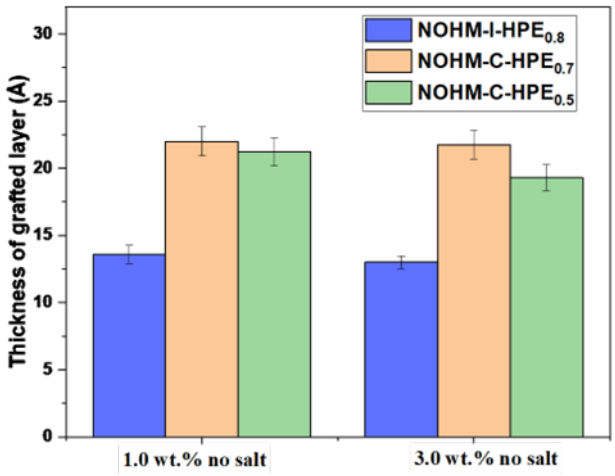

Figure 27. Thickness of grafted layer of NOHM-I-HPE0.8, NOHM-C-HPE0.7, NOHM-C-HPE0.5 in aqueous solution.

on the grafted layer thickness of the NOHM-I-HPE and NOHM-C-HPE. This data shows a stark contrast in the thickness of the grafted layers with the change in graft type. The thickness of the grafted layer of ionic NOHMs is significantly less than that of the covalent NOHMs, at similar grafting density. Even considering that some of the grafted polymer detaches in the ionic NOHMs, the maximum amount of free polymer present in the solvent is ~ 42 vol.%, which corresponds to a 'true' grafting density of ~0.5 chains nm^{-2} for the ionic NOHMs. Our interpretation of this discrepancy is that the thickness of the grafted polymer of ionic NOHMs obtained from the fitting parameter is not the actual thickness. Rather, the free polymer partially penetrates the grafted layer, which manifests as a reduction in the grafted layer thickness that emerges from the fitting. Therefore, the thickness of the ionically grafted layer is not the actual thickness of the grafted polymer, rather it is the effective thickness of the grafted layer. While our previous finding of the interaction of free polymer with the grafted layer starts above 15 wt.%, the analyses performed in this study clearly show that the interaction of free polymer with the grafted layer is also present at low NOHMs loadings, as low as 1 wt.%. This variation in the assembly and structure of the grafted layer with the change in graft type, including the interaction of the free polymer with the grafted layer in the ionic NOHMs, will undoubtedly impact the performance of these nanostructures in solution.

The fitting analysis also provides information on the amount of D_2O solvent penetrating the canopy/shell of the ionic and covalent NOHMs. Similar to Equation 3.1, Equation 3.2 shows the analytical relationship between the concentration of D_2O in the grafted layer (ϕ_1) and the experimentally measured scattering length density (SLD) of the grafted layer in the NOHMs samples. In Equation 3.2, SLD of D_2O = 6.35E-06 $Å^{-2}$, SLD of polymer = 0.517E-06 $Å^{-2}$ and

SLD_{shell} is the experimentally determined SLD of the canopy that is obtained from fitting the scattering data of the ionic and covalent NOHMs solutions.

$$\emptyset_1 = 1 - \frac{SLD_{D_2O} - SLD_{shell}}{SLD_{D_2O} - SLD_{poly}} \quad \textbf{3.2}$$

This analysis shows that the amount of D_2O penetrating the shell in the 1 wt.% ionic and covalent NOHMs are 90% and 60%, respectively. A high amount of D_2O penetration in the shell of ionic NOHMs is consistent with an increase in free space near the nanoparticle surface due to the release of the grafted polymer from the corona. This results in more D_2O near the nanoparticle surface in ionic NOHMs than in covalent NOHMs.

Effect of added salt on the structure and assembly of ionic and covalent NOHMs in solution

The scattering curves of the NOHM-I-HPE and NOHM-C-HPE solutions with 0.1 M $KHCO_3$ were also measured and analyzed using the same scattering models for the solutions without salt. These analyses provide insight into the impact of adding salt to the NOHMs assembly and structure, including the grafted layer thickness of the NOHM-I-HPE and NOHM-C-HPE. Figure 28 plots the variation in the thickness of the grafted layer of the NOHM-I-HPE and NOHM-C-HPE in solution with a change in the amount of salt in the aqueous solution. Figure 49 (pg. 182 in Appendix) shows the SANS profiles of NOHM-I-HPE and NOHM-C-HPE in the aqueous solution with salt.

With the addition of salt, the thickness of the grafted layer on NOHM-I-HPE decreases from ~14 Å to ~10 Å and the radius of gyration of the free polymer decreases from 13 Å to 12 Å. However, when salt is added to the NOHM-C-HPE solution, the assembly of NOHMs changes very slightly, where there is only a nominal change in grafted layer thickness. Thus, the addition of salt significantly alters the structure of the grafted layer in ionic NOHMs, but not in the

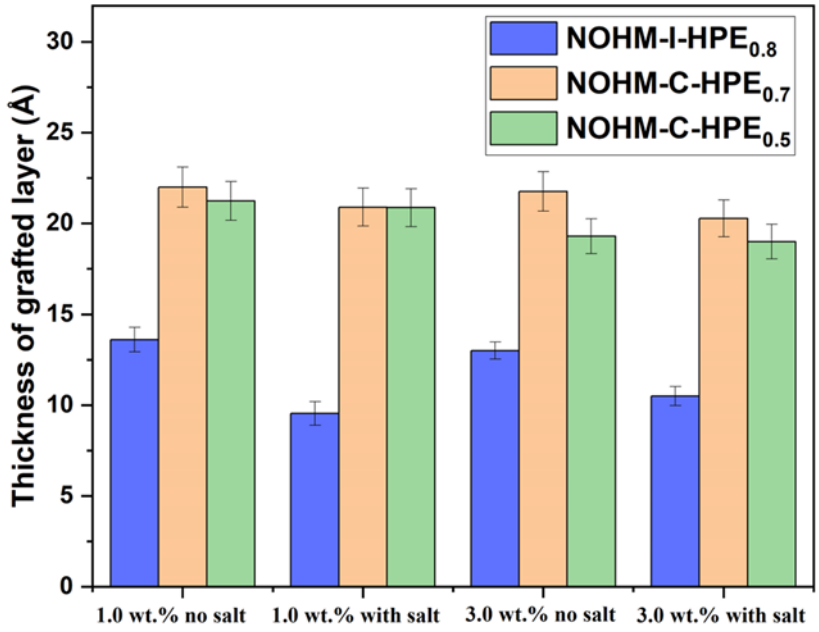

Figure 28. Thickness of grafted layer of NOHM-I-HPE$_{0.8}$, NOHM-C-HPE$_{0.7}$, NOHM-C-HPE$_{0.5}$ in aqueous solution with and without salt.

covalently bound NOHMs. This may be due to a change in the interaction of the free polymer with the grafted layer in the ionic NOHMs solutions. The addition of salt collapses the free polymer chain and subsequently decreases the interaction of the free polymer with the grafted layer. This allows grafted polymer to relax on the nanoparticle surface; thus, the grafted layer thickness decreases. It is also possible that the ions associated with the salt also compete with the HPE polymer to attach to the functionalized nanoparticle surface.[45,103] This is consistent with the D_2O penetration analysis of ionic NOHMs with the addition of salt, which is determined using Equation 3.2. With the addition of salt, the ionically grafted layer contains ~5% more D_2O than in the unsalted solution, while the covalently grafted layer only contains ~ 2.5% more D_2O than in the unsalted solution. This doubling of excess D_2O near the surface should correlate to more mobility within the grafted polymer layer, which may allow small ionic species to interact with functionalized nanoparticles.

Correlation of structural features of ionic and covalent NOHMs solutions with performance

While the SANS results provide structural information of the NOHM-I-HPE and NOHM-C-HPE solutions, they do not offer direct insight into their performance. To address this shortcoming, the structure of the NOHMs and HPE solutions are correlated to their viscosities. With this in mind, Figure 29 plots the viscosity of HPE polymer solutions, as well as those of the ionic and covalent NOHMs solutions with and without salt as a function of solute (NOHMs or HPE) concentration. These results, unsurprisingly, indicate that the viscosity of NOHMs solutions is higher relative to that of the HPE polymer in an aqueous solution. Previous studies have also found increasing viscosity with the presence of nanoparticles in the solution.[36,56,145] Moreover, the viscosities of the covalent NOHMs solutions are higher relative to that of the ionic NOHMs solutions. This can be correlated to the presence of the fractal aggregates in the covalent NOHMs

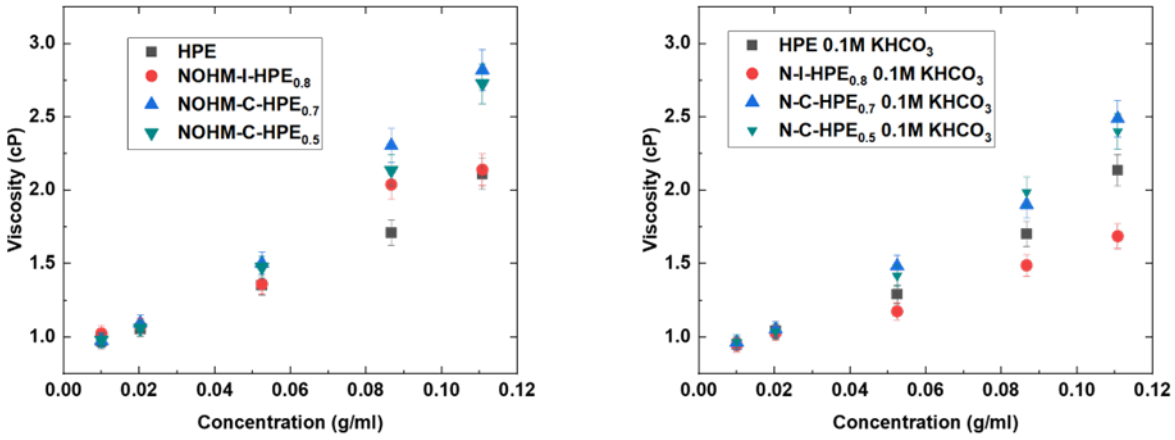

Figure 29. Viscosity of HPE, NOHM-I-HPE$_{0.8}$, NOHM-C-HPE$_{0.7}$, NOHM-C-HPE$_{0.5}$ solutions with (right) and without salt (left) as a function of solution concentration.

solution, where the larger structure exhibits a larger viscosity. It is interesting that as salt is added to the solution, the viscosity of the salted NOHM-I-HPE solution decreases drastically compared to that of the salted NOHM-C-HPE solution and the salted HPE solutions. This drastic decrease in the viscosity of ionic NOHMs may be correlated with the conformational results. The subtle decrease in the viscosity of NOHM-C-HPE correlates to the decrease in the grafted thickness of the polymer. In the case of NOHM-I-HPE, the drastic decrease in viscosity may be due to the collapsed conformation of grafted layer on the silica nanoparticles, resulting in the decrease in the size of NOHMs particle.

To interrogate this possibility, the viscosity of the NOHM-I-HPE solution can be correlated to the size of the NOHM-I-HPE particle, including the grafted layer. The change in NOHM structure can be correlated to the change in the viscosity of the NOHM-I-HPE solutions using Einstein's viscosity equation documented as Equation 3.3.[146]

$$E = E_0 (1 + 2.5V) \quad \textbf{3.3}$$

Here, E is the viscosity of the solution, E_0 is the viscosity of the solvent, and V is the volume of the dispersed particles in the solution. By comparing the viscosities of the unsalted and salted NOHMs solutions for a given concentration, the relative change in size of the NOHM-I-HPE particles can be established. Using Equation 3.3 and the viscosities obtained for the NOHM-I-HPE solutions, this calculation shows that the volume of the NOHM-I-HPE in solution with no added salt is 1.9 times greater than the volume of the NOHM-I-HPE particle in solution in the presence of salt. This change in particle volume must be due to changes in the grafted layer, as the radius of the SiO_2 nanoparticle does not change. According to this analysis, the total grafted layer thickness of the NOHM-I-HPE particle is *ca.* 23Å when no salt is present in the solution, while that of the NOHM-I-HPE particle is ~ 9.5 Å.

This is a little surprising in that the SANS analyses of the grafted layer of NOHM-I-HPE indicate that it is 13-15 Å, significantly less than 23 Å. We reconcile this apparent discrepancy by recalling that the SANS analyses represent the nominal grafted layer, i.e. the portion of the grafted layer that does not interact with the free polymer (See Figure 21). However, clearly, the size of the NOHM-I-HPE that impacts the viscosity is not just this nominal grafted layer. It makes more sense that the size of the SiO_2 nanoparticle, canopy, and free polymer that interacts with the canopy defines the size of the NOHM-I-HPE that impacts the viscosity.

Figure 30 illustrates the structures of the NOHM-I-HPE that impact the flow behavior of the NOHMs solutions with and without salt, emphasizing the impact of the addition of salt on the grafted layer thickness of NOHM-I-HPE particles. The canopy of the NOHM that is important in defining the viscosity includes both the grafted polymer (light green) and interacting free polymer (dark green) to form a larger nanoparticle. The addition of salt collapses the grafted layer thickness, and the R_g of the free polymer, and the extent of interaction between the grafted layer and the free polymer. The result in this case is that the canopy of the salted NOHM that impacts the viscosity of the NOHM solution is dominated by the collapsed grafted layer, with little impact of the free polymer.

Thus, the careful analyses of the SANS data provide crucial insight into the role of the addition of salt on the conformation of the free polymer, on the size of the grafted layer, and correlates these structural characteristics to the viscosity of the salted ionic NOHMs solution. This insight provides important fundamental structure-performance relationships that are needed to rationally design and implement NOHMs solutions in functional applications.

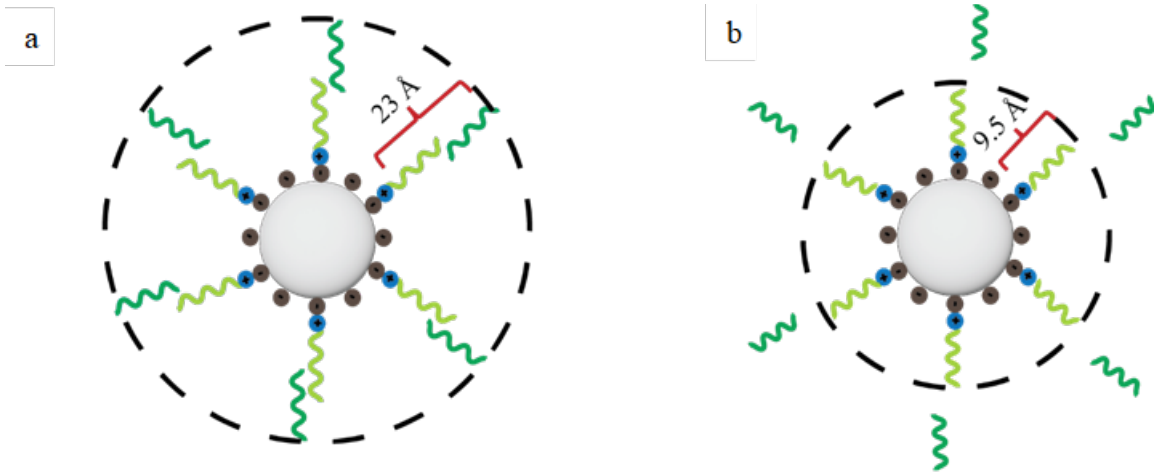

Figure 30. Illustration of the structure of NOHM-I-HPE with and without the presence of 0.1 M $KHCO_3$. 30a. shows the canopy of the NOHM-I-HPE particle that includes both grafted polymer and interacting polymer when no salt is present in the solution, 30b. shows the collapsed canopy of NOHM-I-HPE particle with added 0.1 M $KHCO_3$ salt in solution.

Conclusion

Small-angle neutron scattering experiments provide a critical understanding of the complex assembly and structure of NOHMs in aqueous solutions with a variation in bond type and added supporting electrolyte. Conformational analysis of unbound HPE polymer in aqueous solutions indicates that qualitatively, water is a theta solvent for the polymer and with added electrolyte, the quality of the solvent decreases, corresponding to a decrease in the size of the polymer. Our results highlight that the motif of grafting the HPE polymer to the silica nanoparticles significantly alters the structure, assembly, and performance of NOHMs. At a similar grafting density, the thickness of the grafted layer of ionic NOHMs is altered by the presence of free polymer. In contrast, the grafted layer of covalent NOHMs attains a relaxed state with a canopy thickness that is 1.5 times that of the grafted layer of ionic NOHMs. Moreover, the NOHM-C-HPE solution consists of aggregated particles alongside individually dispersed NOHM-C-HPE, which impacts the flow properties of the solutions, increasing the viscosity.

When salt is added to the NOHMs solutions, the assembly and structure of NOHM-I-HPE solution are altered more significantly than the NOHM-C-HPE solution . The addition of salt decreases the quality of the solvent, leading to a decrease in the size of the free polymer and collapse of the ionically grafted polymer layer on the nanoparticle surface. This results in reduced interaction between grafted and free polymer. These dramatic structural changes correlate to a significant reduction in viscosity. In the case of NOHM-C-HPE, a nominal change in the grafting layer thickness is observed with the addition of salt, corresponding to a slight change in the viscosity of the solutions. Thus, these results provide a holistic understanding of importance of grafting type on the structural features and performance of NOHMs in the presence of electro-

active species that will contribute to improving the functionality of NOHMs in various applications.

Acknowledgment

Research supported as part of the Breakthrough Electrolytes for Energy Storage (BEES), an Energy Frontier Research Center funded by the U.S. Department of Energy (DOE), Office of Science, Basic Energy Sciences (BES), under Award DE-SC0019409 (neutron scattering experiments and analysis). *A portion of this research was also completed at the High Flux Isotope Reactor a DOE Office of Science User Facility operated by the Oak Ridge National Laboratory.* This work benefited from the use of the SasView application, originally developed under NSF award DMR-0520547. SasView contains code developed with funding from the European Union's Horizon 2020 research and innovation program under the SINE2020 project, grant agreement No 654000.

Chapter IV Elucidating the Assembly of Nanoparticle Organic Hybrid Materials (NOHMs) Near an Electrode Interface with Varying Potential Using Neutron Reflectivity

Md Ashraful Haque performed all the neutron reflectivity experiments and analyses. Sara T. Hamilton and Tony G. Feric synthesized the NOHM-I-HPE nanoparticles.

Abstract

A critical concern regarding electrolyte formulation in an electrochemical environment is the impact of the interaction of the multiple components with the electrode surface. Recently, liquid-like neat Nanoparticle Organic Hybrid Materials (NOHMs) have been considered as an electrolyte component to improve the transport of supporting electrolytes to the electrode surface. However, the structure and assembly of the NOHMs near the electrode surface is unknown and could significantly impact the interaction of supporting electrolyte with the electrode surface. Hence, we have investigated the depth profile of polyetheramine (HPE) polymer and NOHM-I-HPE (nanoparticles with ionically bonded HPE polymer) in D_2O in the presence of two different salts ($KHCO_3$ and $ZnCl_2$) near two different electrode surfaces using neutron reflectometry. Moreover, the depth profile of the NOHM-I-HPE near the electrode surface in a potential has also been studied with in-situ reflectivity experiments. Our results indicate that a change in the chemical structure/hydrophilicity of the electrode surface does not significantly impact the ordering of HPE polymer or NOHM-I-HPE near the surface. This study also indicates that the NOHM-I-HPE particles form a clear layer near the electrode surface immediately above an adsorbed layer of free polymer on the electrode surface. The addition of salt does not impact the layering of NOHM-I-HPE, though it does alter the conformation of the polymer grafted to the nanoparticle surface and free polymer sequestered near the surface.

Finally, assembly of the NOHM-I-HPE in presence of $ZnCl_2$ salt also shows a single layer of ordered NOHM-I-HPE particles near the electrode surface at 0V. This ordered layer, however, disappears with the application of -1.1V or -1.5V. At the same time, the applied potential results

in an increased amount of free polymer near the electrode surface. Correlating the depth profile of free polymer and NOHM-I-HPE particles with the electrochemical performance indicates that this assembly of free polymer near the electrode surface in NOHM-I-HPE solutions contributes to the higher current density of the system. Therefore, this holistic study offers insight into the importance of the assembly of NOHM-I-HPE electrolyte and free polymer near the electrode surface in an electrochemical milieu on its performance.

Introduction

The use of Redox Flow Battery (RFB) has been considered as a potential solution to tackle a common renewable energy storage relevant issue, that is the incorporation of this source into grid-scale energy storage infrastructure.[147,148] RFBs possess significant advantages over common lithium-ion batteries, specifically, the ability to separate cathodic and anodic electrolyte, which allows RFB to scale up power delivery and energy density without requiring any effort to change the design for specific applications.[70,149–151] However, the electrolytes used in RFBs still suffer from limited solubility of electro-active species, poor safety and expensive raw materials.[152,153] Recently, deep eutectic solvents,[120–122] microemulsions[116–119] and Nanoparticle Organic Hybrid Materials (NOHMs)[75,130,131,137] have been considered as novel electrolytes for RFBs. Among these novel electrolytes, NOHMs are of particular interest as they have shown great potential to be used in RFBs due to their low volatility,[36] increased thermal stability[37–39] and chemical tunability.[40,124]

Recently, significant research efforts have been undertaken to understand the structure and assembly of NOHMs and correlate this to their transport behavior to provide insight to optimally deploy them in RFBs. Specifically, in our previous study, small-angle neutron scattering (SANS) is used to elucidate the structure and assembly of ionic NOHMs, which highlights that in an aqueous solution, large amount of polymer that is ionically grafted to the nanoparticle can detach

from the grafting site and thus alters the composition of the solvent. Moreover, the *free polymer* can interact with the grafted polymer while altering the conformation of the grafted polymer. Our study also indicates that the addition of salt changes this assembly of polymer as salt competes with the polymer for the grafting site on the nanoparticle. The presence of free polymer and alteration of the polymer conformation and NOHMs assembly with the addition of salt significantly impacts the transport behavior of supporting electrolytes via NOHMs in the bulk and near the electrode.[136]

Literature shows that a very common cause of instable current output is the result of dendrite formation from the uneven deposition of salt.[154–156] The presence of polymeric additives has been shown to improve the process of smooth deposition of salt on the electrode surface.[157,158] A recent study by Hamilton et al. investigated the near surface ordering of ionic NOHMs (NOHM-I-HPE) with polyetheramine or HPE polymer in the presence of Zn salt through various spectroscopic and electrochemical analyses. The study indicates that the presence of HPE polymer and NOHM-I-HPE at a certain composition in relation to Zn salt can maintain a stable current output and assists in the smooth deposition of Zn salt. However, a thorough understanding is still required to understand the packing of NOHM-I-HPE near the electrode surface and its impact on Zn salt deposition. Hence, this study uses Neutron Reflectometry (NR) to investigate the ordering of NOHM-I-HPE and HPE polymer near electrode surface, including the impact of an added potential on this near surface structure.

Neutron Reflectometry is a unique technique that allows the investigation of the depth profile of structures having different composition and densities.[159] Moreover, isotope-specific interaction of neutrons eases the process of discerning protiated species, such as polymers, from deuterated species, such as the deuterated solvent.[160] NR has been used extensively to investigate

the ordering of different ionic liquid-based electrolytes near electrode interfaces.[161–164] The technique is also used to highlight the ordering of nanoparticles near modified surfaces.[165,166] In this study, we investigate the ordering of HPE polymer and NOHM-I-HPE, considered as electrolyte additives, near two different electrode surfaces (SiO_x and Au). Previous studies indicate that surface hydrophilicity alter the ordering of soft materials near a surface.[167] Thus, examining the ordering of the NOHMs near two different surfaces provides insight into the importance of surface hydrophilicity on NOHMs ordering, where the modified SiO_x interface (water contact angle ~40°), is more hydrophilic than Au (water contact angle ~70°). Moreover, we have investigated the near surface ordering of the additives in the presence of supporting electrolyte, 0.1M $KHCO_3$, near both interfaces. Finally, we have examined the ordering of NOHM-I-HPE near the Au electrode in the presence of 0.1M $ZnCl_2$ salt with and without applied potential. At a constant current, applied potential allowed us to provide insight into the impact of the NOHM-I-HPE, and its near surface assembly, on the process of Zn deposition at the electrode surface.

Experimental

NOHM-I-HPE Preparation

NOHM-I-HPE was synthesized using previously reported methods.[40,130,131,137,157] Briefly, 6 wt. % 3-(trihydroxysilyl)-1-propane sulfonic acid (Gelest, Inc.) and 3 wt. % silica nanoparticles (Ludox HS-30, 7 nm, Sigma Aldrich) aqueous solutions were prepared, followed by the addition of the silica suspension to the silane solution in a dropwise manner. This was followed by the addition of 1 M NaOH to adjust the solution pH to 5. The resulting solution was stirred for 24 h at 70 °C, facilitating the grafting reaction between the silica nanoparticle and the linker. Excess linker present was removed via dialysis (SnakeSkin Dialysis Tubing 3500 molecular weight cut-off (MWCO), Thermo Scientific) against deionized water for 48 hours. The linker-grafted solution

was passed through a cation exchange resin column (Dowex HCR-W2, Sigma-Aldrich) for removal of any cations on the functionalized SiO_2 nanoparticles surface and protonation of the linker sulfonate groups. In order to ionically tether the polymer canopy to the surface-modified nanoparticles, a solution of 10 wt.% Jeffamine M2070 (HPE, MW 2000, Huntsman Co.) was prepared and added dropwise to the functionalized nanoparticle suspension until the equivalence point of the solution was reached (pH = 6.5), where all the linker sulfonate groups were neutralized. Finally, the solution was oven dried overnight at 65 °C to remove all water from the prepared mixture. Before sample preparation, NOHM-I-HPE materials were dried again under vacuum at 60 °C for 3 h to ensure the removal of any possible absorbed moisture.

NOHM-I-HPE and HPE Solution Preparation

NOHM-I-HPE and HPE solutions were prepared by mixing previously oven dried NOHM-I-HPE and HPE with D_2O to achieve 10 wt.% in solution using an analytical balance (ML104T, Mettler Toledo) with a precision of 10^{-4} g. For samples containing salt, the solutions were prepared by adding 0.1 M $KHCO_3$ (Sigma-Aldrich, ACS, ≥99.0%) or 0.1 M $ZnCl_2$ (Sigma Aldrich, ACS, ≥99.0%) to the previously prepared NOHM-I-HPE and HPE solutions. Samples were mixed in 10 mL volumetric flasks until complete dissolution of the salt was observed. The pH of the solutions containing $ZnCl_2$ was adjusted to 5.0 using H_3BO_3 (Sigma Aldrich, ACS, ≥99.0%).

Surface Preparations

Au and SiO_x surfaces were prepared in advance of the execution of the neutron scattering experiments. The Au wafer which has a chromium layer for better adhesion of the gold layer, was provided by Oak Ridge National Laboratory's Center for Nanophase Materials Science (CNMS). For the preparation of SiO_x surface, the silicon wafer was first cleaned with a piranha solution prepared using 3:1 sulfuric acid:hydrogen peroxide to remove contaminants from the surface. Then

the wafer was rinsed using nanopure water and dried using air. The wafer was then sealed in air for several days to form oxide layer.

Neutron Reflectivity Measurement and Analysis

Neutron reflectivity experiments were conducted at the BL-4B liquid reflectometer at the Oak Ridge National Lab (ORNL), Spallation Neutron Source (SNS). A solution cell was used to load the samples and then measurements were obtained at 25 °C over a Q range of 0.008-0.2 $Å^{-1}$. The solution cell used for these measurements is detailed by Browning et al.[168] In brief, the cell consists of an aluminum housing in which the experimental wafer (Au or SiO_x) and a 2″ Si wafer are separated by an O-ring. Once the cell is compressed against the O-ring, a space is created that can be filled with ~ 3 ml of the solution. The solution was injected carefully through the liquid inlets created on the Si wafer so that no air bubbles were present. During the sample changeover, the cell was flushed with the sample that is aimed for the next experiment. Before the cell assembly, the parts of the cell were sonicated in hexane and isopropanol for cleaning purposes.

To execute the potential-dependent experiments, a 3-electrode electrochemical cell was prepared that comprised of a counter electrode (platinum), a working electrode (Au) and a reference electrode (Ag/AgCl). Potential dependent analysis at -1.1V and -1.5 (vs Ag/AgCl) was performed using a Biologic VSP potentiostat. When the desired potential was reached, the cell was held for two hours to obtain neutron reflectivity measurements. Before switching the potential from -1.1V to -1.5V, the cell potential was turned off and held at rest for 10 minutes. Figure 50 (pg.183 in Appendix) shows the photo of the electrochemical cell used for the neutron reflectivity measurements.

All reflectivity data was reduced by the instrument scientist and fit using the Motofit package loaded as an extension in the IGOR Pro software.[66] Neutron reflectivity is a sensitive

technique that provides information on the depth profile of a layered structure. The reflectivity fit provides information about the thickness, roughness and scattering length density of the layered structures. The scattering length density (SLD) documents the identity of the specific species probed within the density profile. The SLD of a given species can be calculated using Equation 4.1.

$$\beta\,(z) = \sum b_i\, n_i\,(z) \qquad \textbf{4.1}$$

In Equation 4.1, b_i is the scattering length density of individual nuclei, n_i is the number density of the species and z is the perpendicular distance away from the substrate surface. The calculated scattering length densities of the known components in the systems studied are provided in Table 13 (pg.184 in Appendix). The uncertainties are obtained after multiple fits of the measured neutron reflectivity profiles of each samples.

Discussion and Results

Characterization of SiO_x and Au substrates

The density profile of the Au and SiO_x wafers is first characterized by neutron reflectometry. Figure 51 (pg.185 in Appendix) shows the reflectivity curves and the fit of these curves to a scattering length density profile (Figure 52 pg. 187 in Appendix) for both wafers. The substrates have known composition with unspecified density profiles, which are characterized by thickness (Z) and roughness (R) of layers. Therefore, while fitting the reflectivity profile of the substrates, the SLD of each was not allowed to vary. The results from the reflectivity fitting confirm the formation of an SiO_x layer with an SLD of 2.89 $x10^{-6}$ $Å^{-2}$ with a thickness of ~135Å thick. Two Au-coated wafers are used for reflectivity analysis to minimize the sample change time. The reflectivity analysis of the Au coated Si wafers show a 46-56Å thick chromium layer with a

subsequent Au coated layer of 140Å. Table 14 (pg.186 in Appendix) documents the SLD, thickness and roughness of density profile of the SiO_x and Au coated wafers. The SLD, thickness and roughness of the density profile on these substrates were kept constant in the fitting and analyses of wafers in contact with HPE or NOHMs solutions to increase the confidence of the fit. However, while fitting the NR profiles of HPE sample with the SiO_x substrate, it was realized that the SiO_x surface hydrates in the presence of deuterated water, increasing the SLD from 2.89 $x10^{-6}$ $Å^{-2}$ to 3.49 $x10^{-6}$ $Å^{-2}$. The increase in SLD with the presence of deuterated water molecules of SiO_x surface is previously observed when a microemulsion sample is analyzed for structural variation with a change in hydrophilicity of the surface.[169] The obtained SLD (3.49 $x10^{-6}$ $Å^{-2}$) of the SiO_x surface was then kept constant to obtain a robust fit for the density profile of the HPE polymer with salt and NOHM-I-HPE sample with and without salt.

Density Profile of HPE polymer near Au and SiO_x substrate

To simplify the analysis of the ordering of NOHMs near the Au and SiO_x interfaces, we first investigate the near surface structure of 10 wt.% HPE polymer with and without salt using neutron reflectometry. Figure 31 shows the reflectivity curve and fit of the density profile of HPE polymer in D_2O near the Au surface, where the inset in Figure 31 shows the SLD profile obtained from the fit. Table 3 documents the details of the density profile obtained from reflectivity fit.

The reflectivity results indicate that layers with an SLD of 0.78 and 1.00 (the unit of SLD $x10^{-6}$ $Å^{-2}$ is omitted for simplification) decorate near the Au and SiO_x surfaces, respectively. The SLD of this layer is very close to the SLD of the pure HPE polymer documented in Table 13. Hence, we interpret this to indicate that an HPE-rich layer forms near both surfaces. Moreover, the thickness of the HPE-rich layer near both surfaces is ~38 Å. Small-angle neutron scattering shows that the radius of gyration (R_g) of the HPE polymer is ~15 Å, indicating that two-three layers of

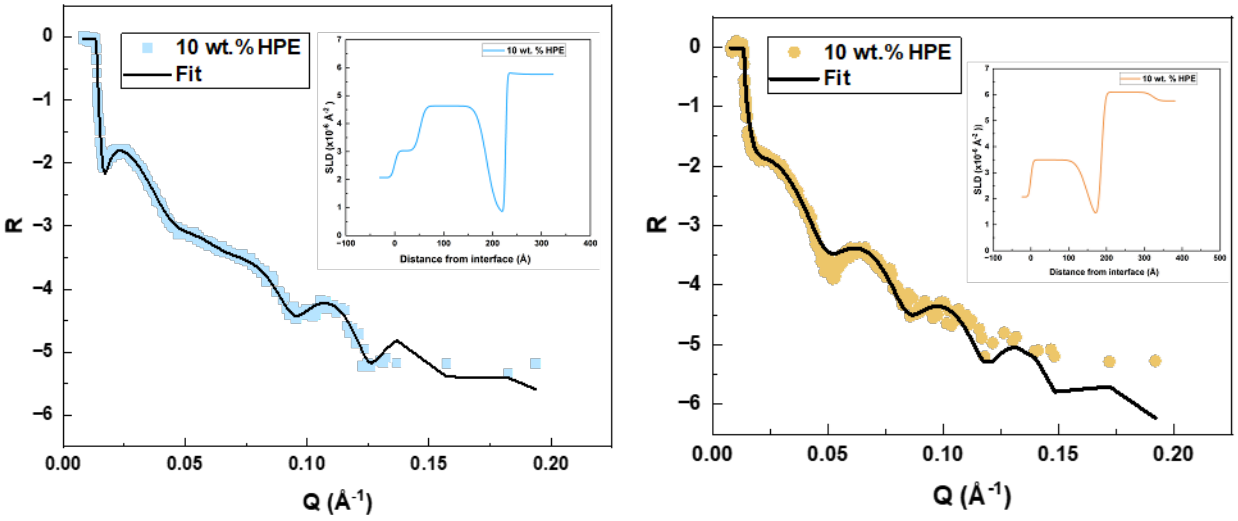

Figure 31. Neutron reflectivity profiles of HPE polymer in D_2O near Au surface (left) and SiO_x surface (right). The inset contains the SLD profile obtained from the fit.

Table 3. SLD profile obtained from fitting of the reflectivity profiles of 10 wt,% HPE polymer and 10 wt.% HPE polymer with 0.1 M $KHCO_3$ in D_2O near Au and SiO_x surfaces.

Sample	Wafers	Parameters	Layer 1	Layer 2	Layer 3	Layer 4	Bulk
10 wt.% HPE	Au	SLD (10^{-6} Å^{-2}) ± error	0.78 ± 0.15	5.85 ± 0.02			5.76
		Z (Å) ± error	36.8 ± 1.63	16.1 ± 2.76			-
		R (Å) ± error	15.9 ± 0.20	2.69 ± 1.90			17.1 ± 5.98
	SiO_x	SLD (10^{-6} Å^{-2}) ± error	1.00 ± 0.04	6.09 ± 0.03			5.76
		Z (Å) ± error	37.8 ± 0.94	135 ± 2.16			-
		R (Å) ± error	21.7 ± 0.92	7.25 ± 0.33			13.3 ± 1.15
10 wt.% HPE 0.1M $KHCO_3$	Au	SLD (10^{-6} Å^{-2}) ± error	0.65 ± 0.03	3.46 ± 0.24	4.37 ± 0.07	5.12 ± 0.08	5.75
		Z (Å) ± error	38.4 ± 0.47	29.1 ± 2.40	45.2 ± 17.3	69.1± 4.58	-
		R (Å) ± error	8.91 ± 1.48	4.73 ± 2.62	11.03 ± 7.22	49.5 ± 12.9	86.1± 49.16
	SiO_x	SLD (10^{-6} Å^{-2}) ± error	0.67 ± 0.15	4.33 ± 0.13	5.28 ± 0.05	5.36 ± 0.01	5.75
		Z (Å) ± error	35.8 ± 2.16	46.1 ± 1.41	97.5 ± 11.5	197 ± 7.40	-
		R (Å) ± error	13.4 ± 0.94	7.47 ± 1.14	5.14 ± 2.46	51.3 ± 11.3	90.9 ± 8.76

HPE polymer assemble near the interfaces.[137] The roughness of the HPE-rich layer is on the length scales of ~16-20Å, where such a high roughness indicates a gradual transition from an HPE rich layer to the subsequent layer. The SLD of this subsequent layer 5.85 on Au and 6.09 on SiO_x, which is approaching the SLD of pure D_2O (6.35). Hence, this layer is a D_2O-rich layer. The thickness of the D_2O-rich layer near Au surface is only 16 Å whereas the D_2O-rich layer near the SiO_x is ~135 Å. The hydrophilic nature of SiO_x could contribute to the broader D_2O layer near the surface.

Impact of $KHCO_3$ salt in the ordering of HPE polymer

Figure 32 shows SLD profile that emerges from the fit of the reflectivity profile (Figure 53 pg. 188 in Appendix) of HPE polymer with added $KHCO_3$ salt neighboring both the Au and SiO_x surfaces. Table 3 documents the details of the SLD density profile that emerge from the fit of the reflectivity data. The SLD of the first layer is ~0.60, where such a low value confirms the presence of an HPE-rich layer near both surfaces. The thickness of the HPE polymer layer is ~37Å on both surfaces, with roughnesses close to 10 Å confirming a multilayer of the HPE polymer. Unlike the sample with no salt solution, the density profile of the subsequent layers near both interfaces is quite interesting. Three layers are observed neighboring the near surface HPE-rich polymer layer in both the Au and SiO_x samples. However, the variation of the SLDs and thicknesses in the density profile are quite different depending on the interfaces.

In the case of the Au surface, the density profile approximates three layers neighboring the HPE polymer-rich layer, where the SLDs of the three layers are 3.46, 4.37, and 5.12. The SLD of 3.46 is well above that of the pure HPE polymer, indicating that this layer is more D_2O rich than the near surface layer, where the amount of D_2O increases with each subsequent layer. However, the SLD of these layers near the SiO_x surface is higher than that observed near the Au surface. This

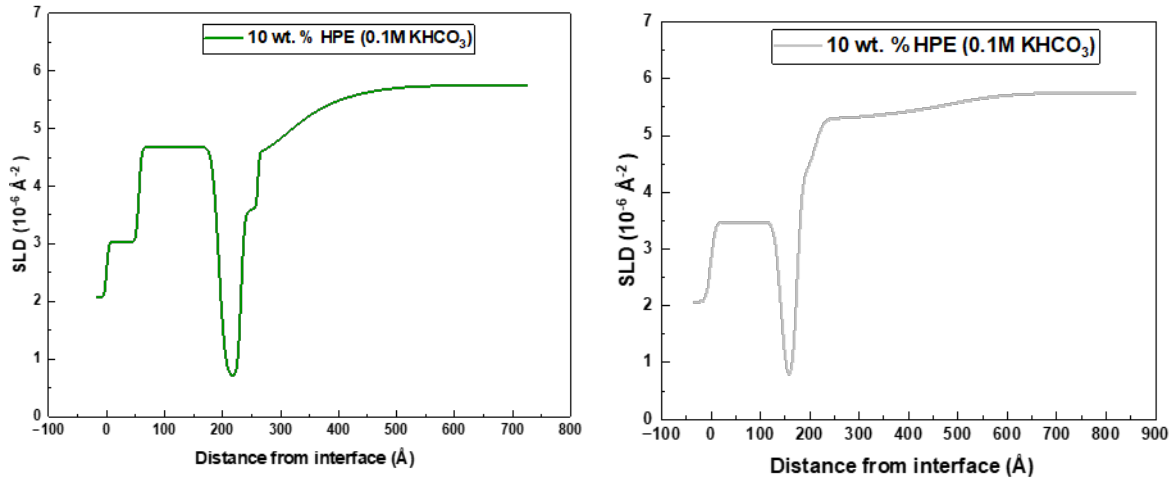

Figure 32. SLD profiles of HPE polymer in D_2O with the presence of $KHCO_3$ salt near Au surface (left) and SiO_x surface (right).

indicates that D_2O aggregates more in the vicinity of the (hydrophilic) SiO_x surface. In fact, the average thickness of the three D_2O rich layers near the SiO_x surface is larger than the same three D_2O rich layers near the Au surface, further documenting the affinity of D_2O to the SiO_x surface. This phenomenon of ordering water molecules in different layers near both substrates can be attributed to the kosmotropic effect of the salt.[170,171] The salt is dissociated to ions in the water , where the electron density of the ions guides the dipolar water molecules to reorient around the ionic species, which results in a structure of water molecules that differs from that of bulk water. Kosmotropic salts promotes the ordering of water, whereas chaotropic salts disrupt the water structure.[172] The kosmotropic behavior of the $KHCO_3$ salt can mediate the ordering of the water by altering arrangement of water molecules around K^+ and HCO_3^- ions.[173] However, it is not clear from the SLD profiles whether the K^+ or HCO_3^- ionic species dominates the water ordering in these layers.

Density profile of NOHM-I-HPE near Au and SiO_x surface

The near surface assembly of NOHM-I-HPE near the Au and SiO_x surface is determined by fitting the reflectivity profile of the 10 wt.% NOHM-I-HPE solutions near the SiO_x and Au surfaces (Figure 54 pg. 188 in Appendix). Figure 33 shows the SLD profile of NOHM-I-HPE near the Au and SiO_x surface resulted from the fit of the reflectivity curves. Table 4 documents the details of the SLD density profile that emerge from the fit of the reflectivity data of NOHM-I-HPE solution near both interfaces.

The results from the reflectivity fit of the NOHM-I-HPE solution show a structure of 5 layers above the Au and SiO_x surfaces and below the bulk NOHM-I-HPE solution. The first layer has a low SLD of ~0.84 near both the Au and SiO_x surface, which is very similar to the SLD obtained from reflectivity profiles of HPE polymer in D_2O. The thickness of the layer varies from

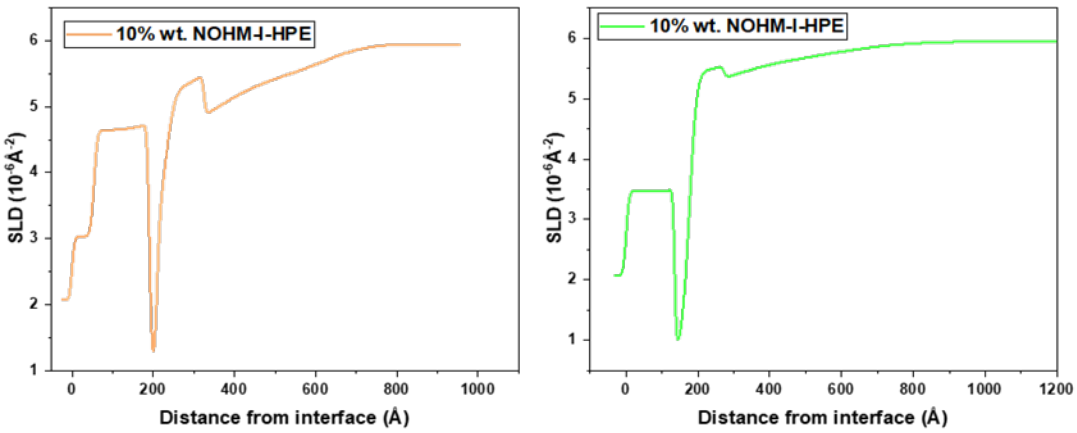

Figure 33. SLD profiles of NOHM-I-HPE in D_2O near Au surface (left) and SiO_x surface (right).

Table 4. Density profile parameters that result from fitting the reflectivity profile of 10 wt.% NOHM-I-HPE and 10 wt.% NOHM-I-HPE with 0.1 M $KHCO_3$ in D_2O.

Sample	Wafer	Parameters	Layer 1	Layer 2	Layer 3	Layer 4	Layer 5	Bulk
10 wt.% NOHM-I-HPE	Au	SLD (10^{-6} Å^{-2}) ± error	0.80 ± 0.15	2.70 ± 0.03	5.01 ± 0.05	4.38 ± 0.08	5.51 ± 0.01	5.95
		Z(Å) ± error	18.7 ± 0.71	18.3 ± 0.56	97.7 ± 0.34	21.9 ± 1.67	285± 22.0	-
		R(Å) ± error	3.54 ± 0.81	5.69 ± 0.27	18.6 ± 2.82	4.95 ± 0.88	117 ± 2.62	80.5± 11.47
	SiO_x	SLD (10^{-6} Å^{-2}) ± error	0.83 ± 0.15	1.21 ± 0.41	5.39 ± 0.01	5.18± 0.11	5.47 ± 0.19	5.95
		Z (Å) ± error	26.6 ± 3.29	19.8± 1.86	105.83 ± 7.10	20.8 ± 0.80	242± 2.62	-
		R (Å) ± error	4.73 ± 0.01	6.89 ± 3.05	16.4 ± 1.20	6.05 ± 2.10	81.5 ± 8.52	188± 10.1
10 wt.% NOHM-I-HPE 0.1M $KHCO_3$	Au	SLD (10^{-6} Å^{-2}) ± error	1.18 ± 0.08	2.94 ± 0.28	4.54 ± 0.01	4.04 ± 0.08	5.35± 0.44	5.9
		Z (Å) ± error	14.9 ± 0.23	14.4 ± 0.42	91.7 ± 1.41	14.6 ± 0.21	221 ± 4.96	
		R (Å) ± error	5.92 ± 1.1	4.77 ± 1.0	21.9 ± 3.80	6.48 ± 0.80	24.41 ± 8.04	60.2± 21.2
	SiO_x	SLD (10^{-6} Å^{-2}) ± error	0.71 ± 0.01	1.03 ± 0.01	5.21± 0.01	4.99 ± 0.01	5.70 ± 0.08	5.9
		Z (Å) ± error	19.8 ± 0.1	17.8 ± 0.04	85.6± 1.5	10.0 ± 1.8	303 ± 9.10	-
		R (Å) ± error	5.40 ± 1.10	8.29 ± 1.27	16.5 ± 0.73	6.95 ± 1.70	30.36 ± 5.71	76.1± 26.84

~15-26 Å, similar to the R_g of the polymer. The second, third, and fourth layers oscillate between a narrow layer (~20 Å) with an SLD of 2.70 (Au surface) and 1.21 (SiO_x surface), followed by a layer with a much larger SLD (5.01 on Au and 5.39 on SiO_x) that is ~100 Å wide, with the fourth layer that is also narrow (~20 Å) with a lower SLD (4.38 on Au and 5.18 on SiO_x).

Given the thicknesses of these layers, and their SLDs, we interpret this SLD profile to indicate the ordering of a single fluctuating layer of NOHMS in D_2O immediately above the HPE rich layer. In this picture, the first layer captures the lower part of the NOHMs layer, which is the grafted HPE on the bottom of the silica nanoparticle; the second layer is the silica nanoparticle dispersed in D_2O, and the fourth layer is the HPE grafted on the top of the nanoparticle. The thickness and SLD of the third layer is consistent with the silica nanoparticle diameter (~90 Å) and scattering length density.[136] The SLD of this layer is higher than the SLD of the pure silica nanoparticle (5.0-5.4 vs ~4.3), which makes sense, as this layer must also include D_2O. The roughness (~17 Å) of this layer is consistent with the fluctuating nature of this NOHMs layer in the z-direction. The fifth layer is a transition layer to the bulk layer that has an SLD of 5.51 and 5.47 near the Au and SiO_x interfaces, respectively. This is the highest SLD among the five layers, which signifies the significant contribution of higher D_2O content in this layer than lower layers.

Overall, the ordering profile of the NOHM-I-HPE near the Au and SiO_x surface shows an interesting assembly, where Figure 34 provides an illustration of the ordering of the NOHMs and HPE near the surface in the NOHM-I-HPE solution from the reflectivity analysis. This cartoon captures the presence of a single HPE-rich layer near both interfaces. This single layer of HPE polymer can be attributed to the *free polymer* that is present in NOHM-I-HPE solution. Then an ordered NOHMs layer is observed above the free polymer layer, a combination that is captured in the second, third and fourth layers from the reflectivity fit. This is capped by a transition layer that

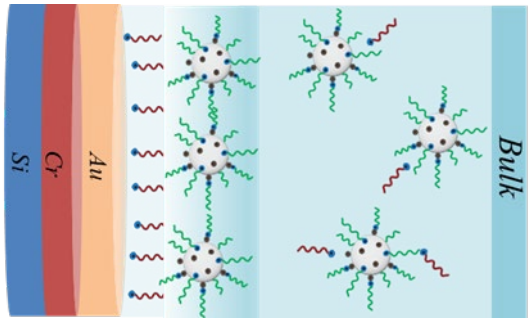

Figure 34. Representative figure illustrating the ordering of free polymer and NOHM-I-HPE near Au surface.

extends to the bulk of the solution.

Impact of $KHCO_3$ salt on the ordering of NOHM-I-HPE near Au and SiO_x surface

The addition of $KHCO_3$ salt to the NOHM-I-HPE does not alter the overall assembly structure of the NOHM-I-HPE near the surface. Analysis of the reflectivity profiles (Figure 55 in pg. 189 Appendix) shows that the density profile of the NOHMs in the presence of the $KHCO_3$ salt forms five layers that mimic the structure in the unsalted NOHMs solutions. Figure 35 shows the SLD profiles of the NOHM-I- HPE solutions with added $KHCO_3$ salt and Table 4 documents the details of the SLD depth profile near both surfaces.

Although the density profile of the NOHMs with solution added salt exhibit similar ordering to those without salt, careful analysis shows notable changes that can be attributed to the role of salt on the nanoscale structure in the solution. For instance, the size of the HPE-rich layer near the surface decreases for both surfaces, while the thickness of the grafted HPE polymer layers decreases from ~19 Å to ~14 Å and ~22 Å to ~15 Å. Thus, the presence of the salt tends to decrease the solvent quality and collapses the HPE polymer in solution. This is consistent with our small-angle neutron scattering results, which quantifies the impact of adding salt on the conformation of the free and grafted HPE polymer.[136,137]

Density profile of NOHM-I-HPE near Au surface with varying potential

The results presented above provide insight into the density profile of NOHM-I-HPE solutions near a quiescent surface. However, it is clear that the application of a potential across this interface can alter the structure of the interface, i.e., by deposition of salt, and it is known that a field can alter the orientation and structure of soft materials. Thus, we completed experiments to monitor the near surface density profile of the NOHMs solutions with $ZnCl_2$ salt in an applied

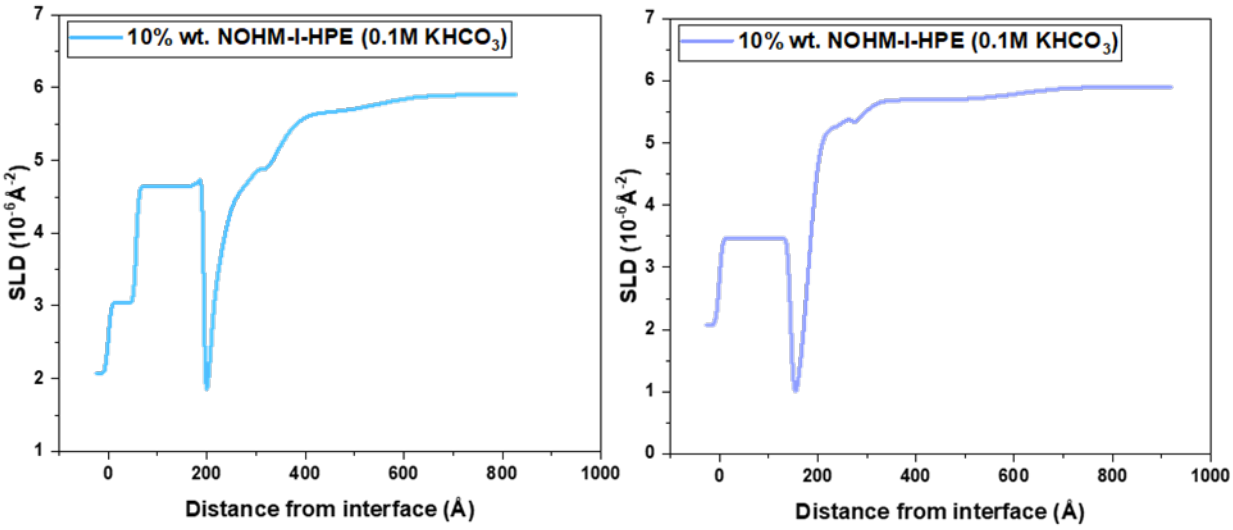

Figure 35. SLD profiles of NOHM-I-HPE in D_2O in the presence of 0.1 M $KHCO_3$ salt near Au surface (left) and SiO_x surface (right).

field. In these experiments, the sample was under the influence of applied potential at 0, -1.1, -1.5 V vs Ag||AgCl. Comparing the reflectivity profile of the NOHM-I-HPE solutions with $ZnCl_2$ with.0V and -1.1 V applied field are presented in Figure 36. Inspection of this figure clearly shows a shift in the fringes with application of -1.1V, indicative of a change in the density profile of the near surface structure of the NOHMs solutions with the applied potential

Figure 37 shows the SLD profiles of NOHM-I-HPE solutions with added $ZnCl_2$ at 0V, -1.1V, and -1.5V, from the fits of the data. Table 5 provides the details of the density profile of the SLD that emerge from the fit.

The ordering of NOHM-I-HPE with the presence of $ZnCl_2$ salt without any potential shows a similar structure to those observed in NOHM-I-HPE solutions with $KHCO_3$ salt. The profile shows the presence of 5 layers between the Au surface and bulk solution. The SLD of the layer neighboring the Au surface is 2.88, while its thickness is ~15 Å. It is interesting that this layer has a higher SLD than that of the NOHM-I-HPE solution with $KHCO_3$ salt, indicating that this layer contains more than just HPE polymer. An increased amount of D_2O in this layer or the coordination of the Zn ion with the ether oxygen of the HPE polymer would increase the SLD of this layer. Previous work by Hamilton et al. indicates that Zn weakly interacts with the ether group of HPE polymer.[157] Thus, we ascribe the increased SLD of the first layer of NOHM-I-HPE with added $ZnCl_2$ salt to be due to the sequestration of Zn ions in this HPE layer. While the potential of increased D_2O loading in this layer cannot be discounted, the absence of this level of D_2O in the $KHCO_3$ solutions supports the presence of Zn ions as the dominant factor. Similarly, this increase in SLD is also observed in NOHMs layer sequestered above the free polymer layer indicating the interaction of Zn ions with HPE polymer grafted to silica nanoparticles.

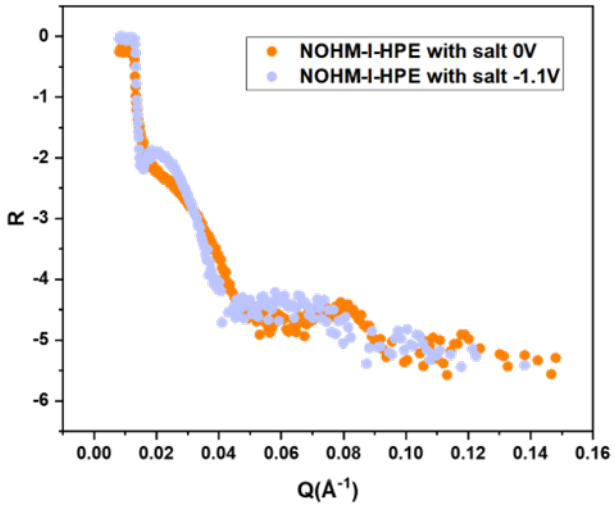

Figure 36. Neutron reflectivity profile showing change in features in reflectivity profile when potential is applied to NOHM-I-HPE solution in presence of $ZnCl_2$ salt.

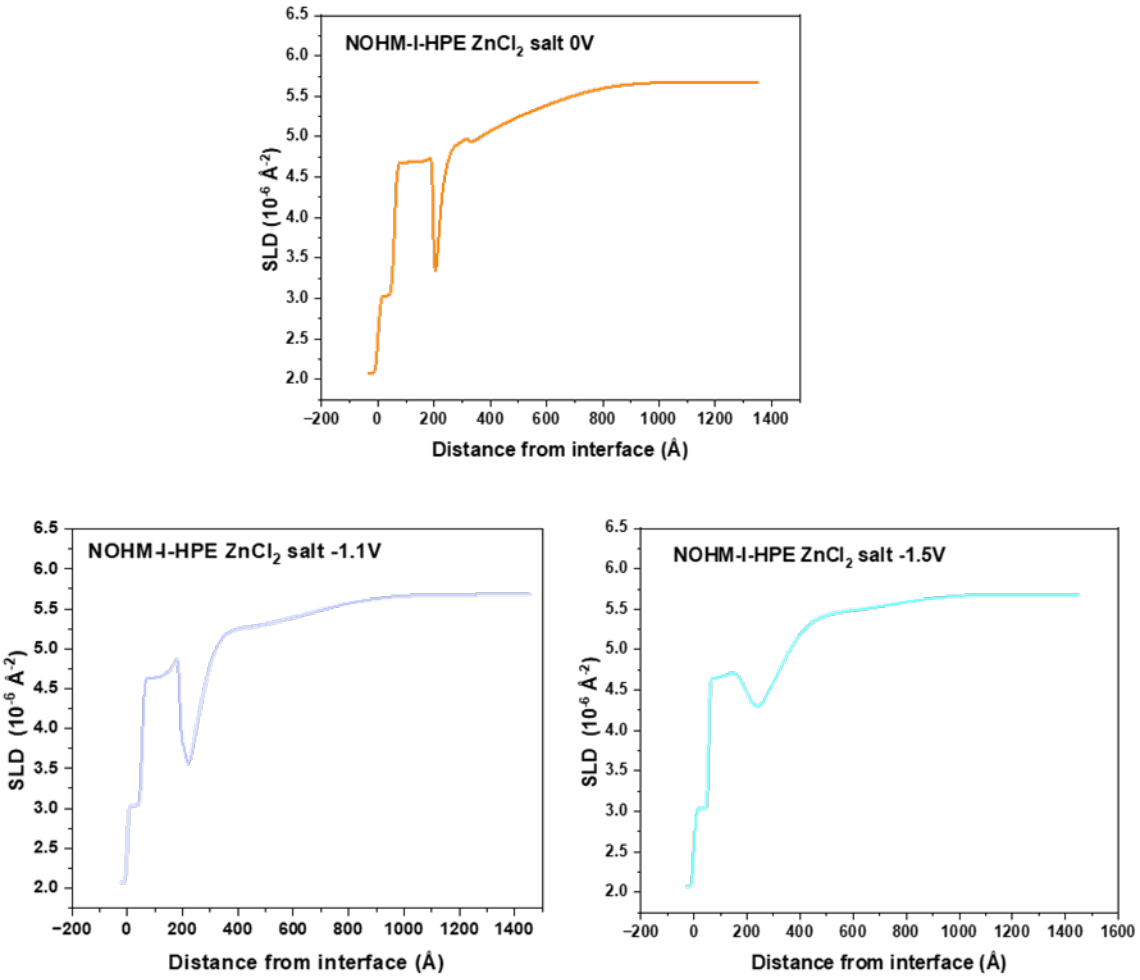

Figure 37. SLD profile of NOHM-I-HPE in presence of $ZnCl_2$ salt in D_2O near Au surface at 0V (top), -1.1V (bottom left), -1.5V (bottom right).

Table 5. SLD density profile that emerge the fit of the reflectivity of NOHM-I-HPE solution in the presence of $ZnCl_2$ salt at 0, -1.1, -1.5V.

Sample	Potential	Parameters	Layer 1	Layer 2	Layer 3	Layer 4	Layer 5	Bulk
10 wt.% NOHM-I-HPE with $ZnCl_2$	**0V**	SLD (10^{-6} Å^{-2}) ± error	2.88 ± 0.13	3.71 ± 0.27	4.95 ± 0.07	4.69 ± 0.04	5.06 ± 0.01	5.68
		Z(Å) ± error	15.5± 1.69	13.9 ± 0.82	98.62 ± 3.5	16.1 ± 2.44	234 ± 6.80	-
		R(Å) ± error	7.43 ± 1.25	9.73 ± 2.01	29.5 ± 5.10	5.32 ± 1.02	43.8 ± 34.0	182± 7.20
	-1.1V	SLD (10^{-6} Å^{-2}) ± error	3.39 ± 0.15	2.40 ± 0.14	5.25 ± 0.05	-	-	5.68
		Z(Å) ± error	16.4 ± 2.62	38.3± 1.50	411± 15.57	-	-	-
		R(Å) ± error	8.30 ± 1.1	17.8 ± 3.68	54.2 ± 5.35	-	-	198± 7.0
	-1.5V	SLD (10^{-6} Å^{-2}) ± error	3.94 ± 0.04	3.76 ± 0.02	5.50 ± 0.10	-	-	5.68
		Z(Å) ± error	39.5 ± 1.10	69.2 ± 4.78	466 ± 19.8	-	-	
		R(Å) ± error	24.8 ± 1.10	17.9 ± 2.20	98.8 ± 10.20	-	-	172± 7.20

The fitting of the reflectivity curves shows that the near surface density profile of the NOHMs solutions with the applied potential, the ordering of the structures near the surface changes from 5 layers to 3 layers before transitioning to bulk. Under the applied potential of -1.1V, the first layer has an SLD of 3.39 with a thickness of ~16 Å. At 0V, the SLD of the first layer is lower than this layer, but the thickness remains similar. This indicates that the HPE polymer is not affected by the applied potential, however, more deuterated water molecule migrates in this layer. The loss of two layers in the SLD profile strongly suggests that the NOHMs nanoparticle no longer order at the surface in an applied potential. Rather, the SLD and thickness that emerge from the density profile suggest that the second layer is also dominated by a broad layer of HPE free polymer. The sequestration of free polymer towards the electrode surface could be due to the attractive interaction between free polymer and the negative potential at the electrode surface. The HPE polymers possess positively charged end groups that are meant to graft to the negatively charged Si nanoparticle surface. Thus, this polymer will be attracted to the negatively charged electrode, driving its migration towards the electrode surface. Similar potential-dependent ordering is a common phenomenon in ionic liquid-based electrolytes where the ordering of cations and anions can be tuned by altering the potential.[162]

Finally, the SLD and thickness of the upper (3^{rd}) layer in the samples with applied potential is similar to the upper (5^{th}) layer of the samples with no applied potential. Thus, we assign this layer to a transition layer from the ordered surface layers to the bulk.

Thus, the near surface ordering of the NOHMs changes dramatically when an applied potential is present. In the absence of an applied field, the reflectivity shows the presence of a fluctuating layer of NOHMs near the Au surface, however upon application of a potential, this near surface ordering is eliminated. This phenomenon is quite unique, however, not surprising

considering that the surface of the silica nanoparticles is functionalized with negatively charged linkers. Consequently, when a negative potential is applied to the electrode surface, we expect that there is a repulsion of the negatively charged NOHM surface and the electrode, disrupting the ordering of NOHMs near the surface. The loss of an ordered NOHMs layer frees that area to promote the assembly of additional free polymer near the surface. The freedom of movement of free polymer and the applied potential also facilitates the accumulation of Zn salt in close proximity to the surface.

Moreover, this data is also consistent with previous work by Hamilton et al. which shows that the deposition of Zn salt at the electrode surface starts at -1.3V. In our reflectivity study, the SLD of the first layer further increases to 3.94 and its thickness by ~240% with the application of a potential of -1.5V. The increase in SLD and roughness is consistent with the deposition of Zn salt on the Au surface. The SLD of the profile decreases with distance from the Au surface, which we ascribe to the assembly of the protonated HPE polymer immediately above the HPE/Zn layer on the electrode. With the increase in potential from -1.1V to -1.5V, the increased SLD of this layer suggests that the increased HPE loading also includes interacting Zn (II) ions in this layer. The upper most layer is again a transition layer between the ordered structure near the electrode surface and the bulk layer. The SLD of the transition layer is higher (5.50) at -1.5V than the SLD of the transition layer (5.25) at -1.1V, emphasizing the diffusion of protonated polymer from the transition layer to the first and second layer, which results in an increase the SLD of the transition layer.

Figure 38 provides an illustration of the density profile of the components in the NOHM-I-HPE solutions at 0V and -1.5V potential in the presence of $ZnCl_2$ salt. At 0V, the free polymer assembles near the surface as the primary first layer, followed by a fluctuating NOHM-I-HPE layer

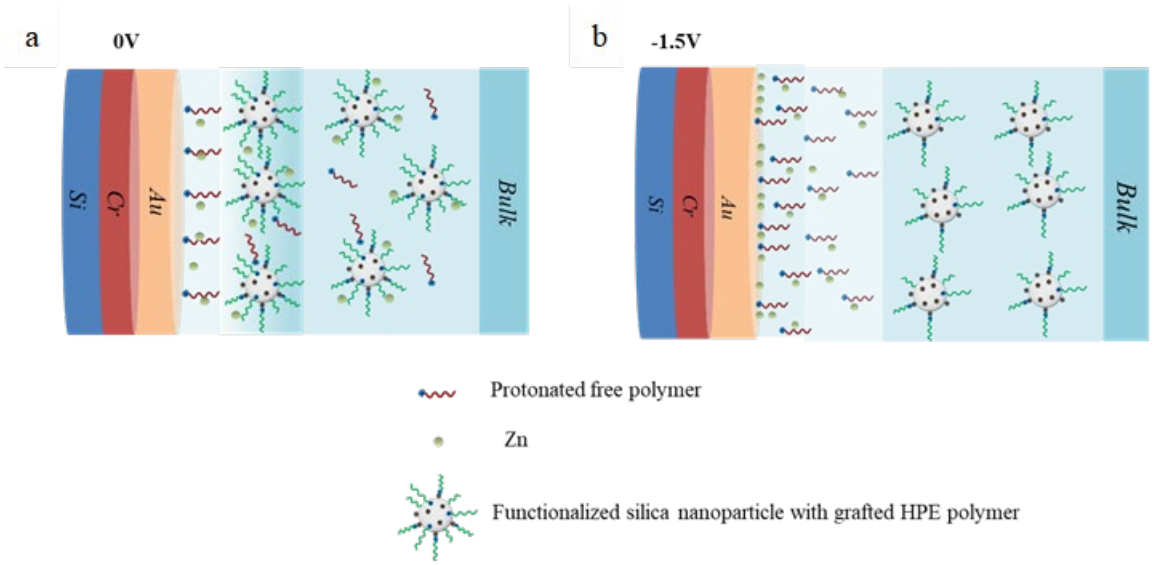

Figure 38. Ordering of free polymer and NOHM-I-HPE near the Au surface at 0 and -1.1V. Figure 38a shows the ordering of free polymer and NOHM-I-HPE near the surface that interacts with Zn (II). Figure 38b shows the deposition of Zn, more ordering of free polymer and disordering of NOHM-I-HPE near Au surface.

immediately above that. The coordination of Zn (II) with the free polymer and the grafted layer manifests as an increase in the SLD of the free and grafted polymer layers. Application of 1.5V potential drives the Zn salt to sequester to the surface in the primary first layer. The ordering of the Zn at the surface is in agreement with the study by Hamilton et al. that observed the segregation of Zn to the electrode surface in similar NOHM-I-HPE samples. Above this near surface layer resides a free polymer-rich layer, which differs from the second layer of the NOHM-I-HPE sample at -1.1V. This layer has a higher SLD and is thicker. The higher SLD indicates that this layer contains more D_2O, which also translates to a larger roughness, signifying a broader gradient to the transition layer. These analyses offer structural insight into the role of the HPE and/or NOHM-I-HPE on the deposition of Zn in these solutions as observed by Hamilton et al. In these studies, it was observed that the presence of HPE or NOHM-I-HPE in $ZnCl_2$ solutions drives a smooth deposition of Zn on the electrode surface and limits dendrite formation. The results presented here show that the ordering of free polymer and the interaction of free polymer with Zn provides an assembly of all components near the surface that benefits the smooth deposition of Zn on the electrode surface at the applied potential.

Impact of ordering of HPE and NOHM-I-HPE on Electrochemical performance

Neutron reflectivity results show that when unbound HPE polymer is in the aqueous solution in the presence of supporting electrolyte, at least two-three layers of unbound HPE polymer assembles near the Au and SiO_x surface (both surfaces will be considered as electrode surfaces for rest of the section). This assembly of unbound HPE polymer can passivate the electrode surface and decrease available surface area for the electro-active species near the electrode surface, decreasing the probability of the redox reaction. Thus, this ordering of unbound HPE polymer could eventually decrease the current density of an electrochemical system by

decreasing the active sites near the electrode surface. In the case of the NOHM-I-HPE, a single layer of free polymer adsorbs near the electrode surface. Moreover, the supporting electrolyte may coordinate with the HPE polymer providing additional pathways for the ion to reach the electrode. This offers pathways for the supporting electrolyte to access the surface of the electrode, to increase current output relative to a solution with only to unbound HPE polymer. This hypothesis is supported by the results presented by Hamilton et al. where $ZnCl_2$ solution showed increased current density with the presence of NOHM-I-HPE additive relative to the sample with just HPE polymer.[157]

Conclusion

In this study, neutron reflectometry has been used to carefully monitor the ordering of the polymeric and nanoparticle components, HPE and NOHM-I-HPE, of a promising electrolyte near electrode surfaces with varying surface chemistry and potential. The study indicates that a change in the hydrophilicity of the surface does not alter the ordering of the free polymer or NOHM-I-HPE near the electrode surface. The addition of $KHCO_3$ salt in the HPE solution causes a kosmotropic effect, forcing layers of varying water composition to assemble near the surfaces. The results show that free polymer segregates to the electrode surface with a neighboring single layer of NOHM-I-HPE. Interestingly, the ordering of the NOHM-I-HPE layer does not significantly change with the addition of salt. Rather, the addition of salt collapses the grafted HPE polymer with little change in the depth profile of free polymer or NOHM-I-HPE. The application of a potential appear to disrupt the single layer of NOHM-I-HPE assembled near the Au surface. Additionally, more free polymer sequesters to the surface with the applied potential. At the highest negative potential examined (-1.5V), the near surface structure of the NOHM-I-HPE remains disordered with an increase in the amount of free polymer and Zn sequestered near the electrode

surface. Correlating this assembly of free polymer and Zn on the electrode surface in a potential with a previous study by Hamilton et al., which shows a smooth deposition of Zn on the electrode surface in the presence of NOHM-I-HPE, suggests that the assembly of the free polymer near the electrode surface promotes the smooth deposition of Zn.[157] Moreover, the higher current density measurements reported in the same study infers that the increased coordination of free polymer near the electrode surface and its interaction with Zn (II) contributes to the high current output.[157] Therefore, the results presented in this study provide fundamental insight into the impact of the near surface assembly of free polymer and NOHM-I-HPE nanoparticles on the ultimate performance of NOHM-based electrochemical systems.

Acknowledgment

This work was supported as part of the Breakthrough Electrolytes for Energy Storage (BEES), an Energy Frontier Research Center funded by the U.S. Department of Energy, Office of Science, Basic Energy Sciences under Award # DE-SC0019409. This research used resources used at the *Spallation Neutron Source, a DOE Office of Science User Facility operated by the Oak Ridge National Laboratory.*

Chapter V Variation of the Conformation of Tempo-based Organic Radical Polymers with Radical Loading, Solvent and Temperature in Battery Relevant Solvents

Md Ashraful Haque performed all the SANS analyses and experiments. Joshua G. Moncada helped with the PTMA polymer solution preparation. Alexandra Easley synthesized and characterized all PTMA polymer and performed all electrochemical measurements and analyses.

Abstract

Organic radical polymers containing a polymer backbone and radical pendant group have been of recent interest as organic electronics. In particular, poly(2,2,6,6-tetramethylpiperidinyloxy-4-yl methacrylate) (PTMA), an organic radical polymer has been extensively studied due to its ease of synthesis and fast transport properties. These features of PTMA make it especially suitable in organic radical batteries as electrodes. Moreover, the conformation of PTMA impacts charge transfer in these applications. For instance, PTMA-based electrodes are often fabricated by casting the polymer from solution, where the conformation of the polymer in solution guides the structure in the final film. However, the conformation of the polymer in battery relevant solvents is not well understood. Hence, we have determined the conformation and thermodynamics of PTMA in battery relevant solvents using small-angle neutron scattering (SANS). More precisely, SANS data were carefully analyzed to elucidate the structure and polymer-solvent interactions of PTMA solutions in N-methyl-2-pyrrolidone (NMP) and a 50:50 (wt.%) ethylene carbonate:dimethyl carbonate (EC:DMC) mixture with varying radical content (68% vs. 98%) and temperature (25 °C and 60 °C). These results indicate that both solvents are theta solvents for the PTMA polymer irrespective of radical loading and temperature. Further investigation shows that PTMA attains an expanded chain conformation in NMP and a more compact polymer chain conformation in EC:DMC, demonstrating the importance of choice solvents on the conformation of PTMA. More importantly, this study clearly shows that the conformation of PTMA is dominated by the radical loading, where a higher radical loading

corresponds to a more rigid and expanded structure, while solvent choice and temperature are also important, but subordinate factors.

These results also highlight that the calculation of polymer-solvent interaction parameter using Hansen solubility parameter must account for the presence of counter-ion in the solvent, or the calculation overestimates the quality of the solvents for the PTMA polymer. Finally, the electrochemical performance of PTMA films formed from each solvent shows improved performance of PTMA films cast from EC:DMC relative to those cast from NMP, where the compact conformation of PTMA in EC:DMC enables improved inter- and intrachain charge diffusion. Therefore, these results demonstrate the importance of understanding the conformation and assembly of PTMA polymer with variation of radical loading, solvent and temperature and provide key insights that can be used to rationally improve the performance of PTMA-based organic electronics.

Introduction

Recently, the demand for all organic batteries and polymer-based energy storage systems (ESS) has been rapidly increasing as a sustainable replacement to the frequently used Li-ion batteries.[174,175] In current Li-ion batteries, the cathode usually consists of inorganic transition metal oxide such as manganese, nickel and cobalt, which are found in a finite quantity in nature. Moreover, these materials suffer from supply chain issues, poor recyclability, and toxicity.[15,176,177] Hence, it has become imperative to look for potential replacements of these traditional materials used in Li-ion batteries. Materials based on organic redox-active moieties can serve as a potential replacement in Li-ion batteries due to their superior performance as conductive materials in organic radical batteries, solid state batteries and flow batteries.[25,28,178]

Organic radical polymers often consist of a redox-active pendant group with a stable free radical that controls the charge transport and a polymer backbone, which in turn controls the thermal and mechanical properties of the polymer.[179] The redox active pendant group of the organic radical polymer can undergo reversible redox reactions allowing them to serve as alternative materials to the inorganic materials used in lithium-ion batteries.[25] Among a myriad of organic radical polymers, poly(2,2,6,6-tetramethylpiperidinyloxy-4-yl methacrylate) (PTMA) is commonly studied for its ease of synthesis, fast charge transport kinetics, and high theoretical capacity of 111 mAh g^{-1}.[30] Unique structural features of the PTMA redox-active moiety, 2,2,6,6-tetramethyl-1-piperidinyloxy (TEMPO), include its stable nitroxide radical state that, during the charging process, can convert to either oxoammonium cation or to the aminoxyl anion. The discharging process allows the PTMA polymer to revert to its stable radical form. This functionality of PTMA has been capitalized to observe an operational capacity at almost 100%, matching to its theoretical capacity.[180]

PTMA has been used as a redox-active material for organic batteries and ESS, however, there is a lack of knowledge related to the conformation of this non-conjugated material and charge transfer mechanisms. With this in mind, the conformation of PTMA during the fabrication and operation of batteries is of interest to further understand the factors impacting charge transfer in organic radical polymers. Previously, small-angle neutron scattering (SANS) has been used to reveal the structure of various amorphous polymers in solution and the melt.[181–183] Using SANS, our previous study examined the conformation of PTMA in acetonitrile, documenting the change in PTMA conformation and assembly as a function of radical loading and the oxidation level.[51] However, the conformational changes can also impact the performance of PTMA-based electrodes. Therefore, we seek to expand these studies to provide more direct information on the

conformation and structure of PTMA in battery relevant solvents. For example, the performance of a PTMA-cathode in a commonly used battery solvent such as carbonates fades after a certain number of cycles resulting in poor battery efficiency.[184] Moreover, in order to construct the PTMA cathode for an organic radical battery, the PTMA must be dissolved in a suitable solvent. N-methyl-2-pyrrolidone (NMP) is commonly used to process PTMA as an electrode due to its low volatility and thermal stability.[185–187] Frequent use of NMP as a solvent to fabricate PTMA-based cathodes further motivates the examination of PTMA conformation in NMP to provide molecular level insight into the correlation of its performance in a battery to molecular conformation.

Here, we use SANS to elucidate the conformation and thermodynamic interactions of PTMA in NMP and a 50:50 mixture of ethylene carbonate and dimethyl carbonate (EC:DMC). We utilized deuterated solvents to improve the contrast between polymer and solvent thus enabling the investigation of the conformation of PTMA in dilute solution using SANS. In this current study, the radical loading of PTMA is varied by using different oxidizing agents (meta-chloroperoxybenzoic acid and H_2O_2). The conformation and polymer solvent interactions of PTMA in deuterated NMP and a 50:50 mixture of deuterated ethylene carbonate and deuterated dimethyl carbonate (EC:DMC) at room temperature (RT) and at 60°C were investigated. Analysis of the scattering data by a Zimm plot analysis quantifies the thermodynamic interaction of PTMA and the solvents of interest. Additionally, fractal dimension analysis complements the Zimm analysis. Comparison of the experimentally determined and theoretically calculated Flory-Huggins interaction parameters emphasizes the importance of accounting for counter-ions to understand the thermodynamic interactions between the organic radical polymer and solvents. Our analyses also indicate that solvent, radical loading, and temperature all impact the final conformation of PTMA.

Finally, an electrochemical study of PTMA as a thin film that is cast from both solvents establishes a correlation between the conformation in solution and the performance of PTMA.

Experimental

Materials

The following materials were received from Sigma Aldrich and used without further purification: toluene, sodium tungstate dihydrate (Na_2WO_4•$2H_2O$), ethylenediaminetetraacetic acid disodium salt dihydrate (Na_2EDTA•$2H_2O$), methanol, and magnesium sulfate. 2,2′-azobis(2-methylpropionitrile) (AIBN) was received from Sigma Aldrich and was recrystallized from ethanol before use. The following materials were received from VWR BDH Chemicals and used without any further purification: hexanes, dichloromethane (DCM), hydrogen peroxide solution (30 wt.%), methanol. 2,2,6,6-tetramethyl-4-piperidyl methacrylate (TMPM) was received from TCI America and used without purification. 4-cyano-4-(((dodecylthio)carbonothioyl)thio)pentanoic acid (CTA) was used as received from Boron Molecular. Ultrapure water (water) was collected from a Milli-Q® water purification system (18 MΩ·cm).

Synthesis of PTMA-X-R

The synthetic conditions for the different molar mass PTMA-X-R produced are found in Table 6, where X is the estimated degree of polymerization and R is the radical loading obtained from electron paramagnetic resonance (EPR) spectroscopy. The synthesis of PTMA-276-68 and PTMA-277-98 followed the protocol described Easley *et al.*[186] For the remaining PTMA-X-R polymers, the synthetic protocol was modified to use 4-cyano-4-(((dodecylthio)carbonothioyl)thio)pentanoic acid as the CTA (**Scheme 1**).[186,188] A summary of the synthetic procedure to synthesize PTMA-15-72 is provided as an example. In a 50 mL Schlenk

Table 6. Summary of the synthetic conditions, degree of polymerization, molar mass, dispersity, and radical loading for the synthesized PTMA samples.

Polymer Name	**TMPM: CTA: AIBN[a]**	**Oxidation Method**	**DP[c]**	**M_n (kDa)[c]**	**Đ[c]**	**Radical Loading (%)[d]**
PTMA-15-72	13: 1: 0.3	H_2O_2	15	3.5	1.2	72
PTMA-44-87	33: 1 : 0.3		44	10.6	1.2	87
PTMA-122-95	98: 1 : 0.3		122	29.2	1.2	95
PTMA-277-98[b]	330: 1 :0.7		277	66.6	1.7	98
PTMA-276-68[b]	330: 1 :0.7	mCPBA	276	66.2	2.1	68

[a]Molar ratio

[b]Synthesized using 2-phenyl-2-propyl benzodithioate as a CTA.

[c]Determined using SEC in THF against a polystyrene standard.

[d]Determined using EPR.

flask, 5 g (22.2 mmol) of TMPM, 83.9 mg (0.5 mmol) of AIBN, 0.69 g (1.7 mmol) of CTA, and 7.7 mL of toluene were combined at ambient conditions. The flask was sealed, and three freeze-pump-thaw cycles were performed. The flask was left under nitrogen, heated to 75 °C, and left to react for 24 h. The reaction was cooled to room temperature and exposed to air to terminate the reaction. The reaction solution was precipitated in hexanes. The resulting polymer, PTMPM-15-CTA, was collected and dried under vacuum for 24 h. The CTA end groups were removed as previously described, by combining 2 g of PTMPM-15-CTA (8.9 mmol of repeat unit) with 2 g (12 mol) of AIBN in 80 mL of toluene.[186,188] The reaction solution was then heated to 75 °C, and left to react for 24 h. After 24h, the reaction was allowed to reach room temperature before being precipitated in hexanes. The precipitated polymer, PTMPM-15, was collected and vacuum dried for 24 h. Finally, PTMPM was oxidized using H_2O_2 by reacting 0.6 g of PTMPM-15 (2.6 mmol of repeat unit), 218.8 mg (0.7 mmol) of $Na_2WO_4 \cdot 2H_2O$, 115.8 mg (0.3 mmol) of $Na_2EDTA \cdot 2H_2O$ in 30 mL of methanol in a 250-mL round-bottom flask equipped with a condenser. The reaction was carried out at 60 °C for 5 min, before 3.0 mL of 30 wt.% H_2O_2 was added dropwise. After the addition was complete, the reaction was left at 60 °C for 24 h. The solid precipitate was dissolved in DCM, washed with MQ water three times, and dried over magnesium sulfate for 12 h. The magnesium sulfate was filtered out followed by precipitation of the resulting solution into hexanes. The resulting orange solid (PTMA-15-72) was collected and vacuum dried overnight.

Scheme 1. Synthetic route for PTMA-X-R samples using 4-cyano-4 (((dodecylthio)carbonothioyl)thio)pentanoic acid as the CTA.

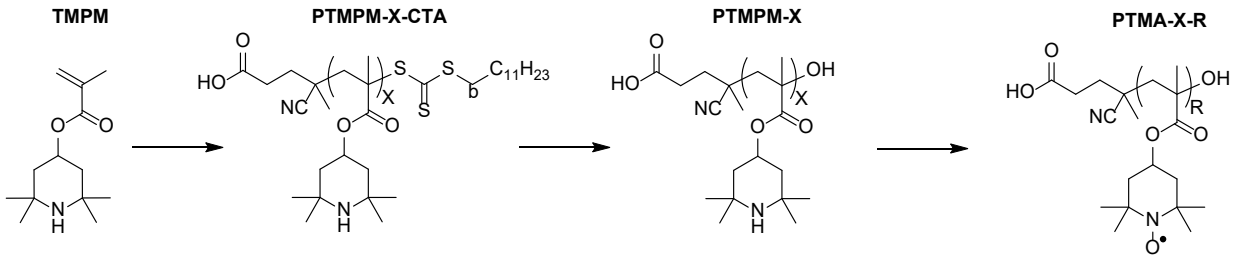

Chemical Characterization

For NMR, 10 mg of PTMPM-X-CTA or PTMPM-X, was dissolved in 1 mL of deuterated chloroform and a 400 MHz Bruker NMR was used to collect the ^{1}H-NMR spectra. Size exclusion chromatography (SEC) was performed on a TOSOH EcoSEC (HLC-8320GPC) with UV (254 nm) and RI detectors at 40 °C with THF as the eluent with a flow rate of 0.35 mL min^{-1}. The SEC sample was prepared by dissolving 5 mg of PTMA-X-R in 1.5 mL of THF. The molecular weights were calculated using a calibration curve based on polystyrene standards. The SEC columns were TSKgel SuperHM-M and TSKgel SuperH-RC. Electron paramagnetic resonance (EPR) spectroscopy was performed on a Bruker Elexsys at room temperature. For EPR, a reference solution of 1 mM of 4-OH-TEMPO and a sample solution of 1 mM of polymer repeat unit (PTMA-X) were prepared in chloroform. Using the UV-Vis calibration curve previously reported by Easley *et al*., the radical loading of each PTMA-X-R sample solution, prepared at a concentration of 0.03 M (repeat unit basis) in chloroform, was calculated at 462 nm.[186] Finally, XPS spectra were collected on powder samples of the PTMA-X-R samples using an Omicron XPS with an Argus detector using a monochromated Mg X-ray source (hm = 1253.6 eV). Survey scans were performed with an analyzer pass energy of 150 – 1150 eV (1.0 eV steps, 50 ms dwell time). High-resolution scans of nitrogen (N 1s), chlorine (Cl 2p), and fluorine (F 1s) were collected with a pass energy of 150 eV (0.05 eV steps, 200 ms dwell time). All spectra were calibrated using the C 1s photoemission peak (sp^{2}-hybridized carbons) at 284.5 eV. Curve fitting of N 1s spectra was

conducted using a Gaussian-Lorentzian peak shape after a Shirley-type background correction and the FWHM of the deconvoluted peaks was constrained.

Small Angle Neutron Scattering (SANS) Experiments

The solvents used for SANS experiments are N-methyl-2-pyrrolidinone-d9 (d-NMP), d6-dimethyl carbonate (Cambridge Isotope Lab) and d4-ethylene carbonate (CDN Isotopes, Inc). SANS experiments of PTMA-276-68 polymer in N-methyl-2-pyrrolidinone-d9 (d-NMP) and a 1:1 (w/w) mixture of d4-ethylene carbonate and d6-dimethyl carbonate (d-EC:d-DMC) were performed at the National Institute for Standards and Technology's Center for Neutron Research using the NG-7 beamline with a q range of 0.0042 $Å^{-1}$ to 0.41 $Å^{-1}$. The SANS experiments of PTMA-15-72, PTMA-44-87, PTMA-122-95, PTMA-277-98 polymers in N-methyl-2-pyrrolidinone-d9 (d-NMP) were performed at the high flux isotope reactor (HFIR) at the Oak Ridge National Laboratory on the CG-2 GP-SANS beamline with a q range of 0.003 $Å^{-1}$ to 0.7 $Å^{-1}$. Here, $q = 4\pi/\lambda \sin(\theta)$, where, q is the momentum transfer vector, λ is the neutron wavelength and θ is the scattering angle. The raw data obtained at NIST was reduced using NCNR SANS reduction package,[95] whereas the raw data from HFIR was reduced using the reduction protocol prepared by the instrument scientist. The scattering data of PTMA-X-R was corrected for sample transmission, and the scattering of the empty cell, solvent scattering, and the background. The fitting procedure was performed using SasView software.[138]

Group Contribution and Flory-Huggins Interaction Parameter

The Hansen solubility parameters (HSPs) for PTMA-276-68 and PTMA-277-98 are reported in Table 7 and were estimated using the Hansen group contribution method and values previously published by our group for the nitroxide radical and oxoammonium cation.[186,189] not alter the Hansen solubility parameters. Previous studies also showed that small polarizability

Table 7. Dispersion (δ_d), polar (δ_p), hydrogen bonding (δ_h), and total (δ_{total}) Hansen solubility parameters for the polymers and solvents utilized.

Material	**δ_d (MPa$^{1/2}$)**	**δ_p (MPa$^{1/2}$)**	**δ_h (MPa$^{1/2}$)**	**δ_{total} (MPa$^{1/2}$)**
PTMA-276-68	19.2	4.7	7.5	21.2
PTMA-277-98	19.1	4.7	7.8	21.1
NMP[a]	18.0	12.3	7.2	22.9
EC[a]	19.4	21.7	5.1	29.6
DMC[a]	15.5	3.9	9.7	18.7
EC:DMC (1:1)[b]	17.5	12.8	7.4	24.1

[a]Values from ref.[190]

[b]Estimated as a 50:50 mixture.

Additionally, the Hansen solubility parameter values for NMP, EC, and DMC were taken from Hansen and are summarized in Table 7 below.[191] It was assumed that the solvent deuteration did and vibration energy difference in C-D and C-H results in little to no impact on the solubility parameter of solvents.[192,193]

Using the total Hansen solubility parameters, the Flory-Huggins (polymer-solvent) interaction parameter, χ, is determined for each polymer-solvent combination using Equation 5.1.

$$\chi = \frac{V_s}{RT}\left(\delta_{total,s} - \delta_{total,p}\right)^2 + 0.34 \quad \textbf{5.1}$$

In Equation 5.1, V_s is the molar volume of the solvent (in cm^3/mol), R is the gas constant (8.314 cm^3 MPa/mol K), T is the temperature (in K), and $\delta_{total,s}$ and $\delta_{total,p}$ are the total Hansen solubility parameters for the solvent and polymer, respectively. The molar volumes of NMP, EC, and DMC are 96.5, 66.0, and 84.2 cm^3/mol, respectively. Using these values, the molar volume of the EC:DMC mixture is 75.1 cm^3/mol.

In addition to estimating χ from the total Hansen solubility parameters, it may also be experimentally determined using the second virial coefficient (A_2) from Zimm analysis of the SANS data, following Equation 5.2.[194]

$$\chi = 0.5 - A_2 V_s \rho_p^2 \quad \textbf{5.2}$$

where ρ_p is the density of the polymer (in g/cm^3).

Electrochemical Characterization

PTMA-276-68 and PTMA-277-98 were dissolved in NMP at 2 mg/mL and PTMA-276-68 was also dissolved in EC:DMC (1:1, w:w) at 2 mg/mL. 20 µL of the polymer solution was drop

casted onto a glassy carbon electrode and allowed to dry at ambient conditions for 48 hours. After 48 hours, the samples were dried under vacuum for an additional 24 hours before electrochemical testing. The polymer coated glassy carbon acted as the working electrode in a 3-electrode beaker cell with a Pt wire counter electrode and an Ag/AgCl (sat.) reference electrode. The supporting electrolyte was 0.5 M tetraethylammonium tetrafluoroborate ($TEABF_4$) in water. The polymer thin film was conditioned by cyclic voltammetry (CV) (50 cycles at 50 $mV \cdot s^{-1}$) before conducting two CV cycles each at varying scan rates (10, 25, 50, and 100 $mV \cdot s^{-1}$). Chronoamperometry was performed by a potential step from 0.3 V to 1.1 V and retuning to 0.3 V *vs.* Ag/AgCl (all voltages were held for 60 seconds). Additionally, galvanostatic charge/discharge was performed for 5 cycles at both 20 $\mu A/cm^2$ and 40 $\mu A/cm^2$. All electrochemical measurements were performed using a Solartron Electrochemical Interface 1287 potentiostat/galvanostat. The slope for determining the kinetic parameters from the Cottrell plots was determined as a tangent line with an intercept of zero.[195,196]

Results

Synthesis and characterization of PTMA-X-R

The precursor to PTMA-X-R, PTMPM-X, was synthesized using reversible addition–fragmentation chain transfer (RAFT) polymerization, where X is the degree of polymerization and R is the radical loading from electron paramagnetic resonance (EPR) spectroscopy (Scheme 1, Table 6). The resulting PTMPM-X contained RAFT chain transfer agent (CTA) end groups (PTMPM-X-CTA). The end groups were removed before oxidation to prevent crosslinking.[188] Figures 57-59 (pg. 184-186 in Appendix) show the ^{1}H-NMR for PTMPM-X-CTA and PTMPM-X. The spectra for all polymers show a decrease in the peaks associated with the CTA (between 3 and 3.5 ppm), confirming the successful removal of the CTA end group.

After removing the CTA end group, the PTMPM-X precursors were oxidized with meta-chloroperoxybenzoic acid (mCPBA) or hydrogen peroxide, following previously reported methods to form the PTMA-X-R radical polymers.[188,197,198] The molar mass (and thus degree of polymerization) and dispersity were determined for each polymer using size exclusion chromatograph (SEC), where the results are shown in Table 6. Following oxidation, the radical loading was determined using X-ray photoelectron spectroscopy (XPS) and electron paramagnetic resonance (EPR) spectroscopy. Table 6 and 7 document the amount of radical loading and pendant group distribution in each PTMA-X-R sample. The EPR and XPS plots are also documented in Figures 60 (pg. 187 in Appendix) and 61 (pg. 188 in Appendix). XPS was critical for determining the distribution of functional groups, amine, nitroxide radical, and oxoammonium cation groups, for each PTMA-X-R sample. The different groups result from no oxidation, oxidation, and over-oxidation of the polymer, respectively.

Utilizing the above PTMA-X-R samples various analyses were considered to determine the structural characteristics of PTMA-X-R in d-NMP and d-EC:d-DMC using small angle neutron scattering. The structural parameters are determined from analyses of the scattering patterns, including Guinier and Zimm analyses to illuminate the size and conformation of the polymer and Zimm analysis to gain insights on the thermodynamic interaction parameter between the solvent and the polymer. The molecular weight dependence of the radius of gyration for the synthesized PTMA-X-R is determined to elucidate the effect of radical content on the polymer conformation. Finally, a fractal analysis quantitively reveals the compactness of the PTMA-X-R chain, highlighting the variation of the polymer chain conformation in different solvents at 25 °C and 60 °C.

Guinier & Zimm analysis of PTMA-X-R in solution

Small-angle neutron scattering (SANS) scattering profiles of PTMA-276-68 in d-NMP and d-EC:d-DMC and PTMA-277-98 in d-NMP at room temperature and 60 °C are shown in Figure 39.

To determine the radius of gyration of the PTMA-X-R polymer in individual solvents, the Guinier model, documented as Equation 5.3 is used.

$$ln[I(q)] = ln[I(0)] - \frac{q^2 \times {R_g}^2}{3} \quad \textbf{5.3}$$

Here, R_g is the radius of gyration, q is the wave vector and I(0) is the forward scattering intensity.[52,63] Moreover, the molecular weight of the PTMA-X-R polymer can be determined from the forward scattering intensity of the PTMA-X-R polymer solutions using Equation 5.4.

$$I(0) = \frac{M_w \times d \times N_A}{\varphi \times \Delta\rho^2} \quad \textbf{5.4}$$

In Equation 5.4, M_w is the weight average molecular weight of PTMA-X-R polymer, d is the density of the PTMA-X-R polymer, N_A is Avogadro's number, ϕ is the volume fraction of the PTMA-X-R polymer in solution and Δρ is the difference in scattering cross-section of the polymer and solvent. The radius of gyrations and molecular weights of all the PTMA-X-R studied as obtained from the Guinier analysis are listed in Table 15 (pg. 196 in Appendix).

To elucidate the quality of the NMP and EC:DMC as solvents for PTMA under different conditions, a Zimm analysis using Equation 5.5 was also considered.[199] An example of a Zimm plot is shown in Figure 62 (pg. 197 in Appendix).

$$\frac{K\varphi}{I(q)} = \frac{1}{M_w}\left(1 + \frac{q^2 {R_g}^2}{3}\right) + 2A_2\varphi \quad \textbf{5.5}$$

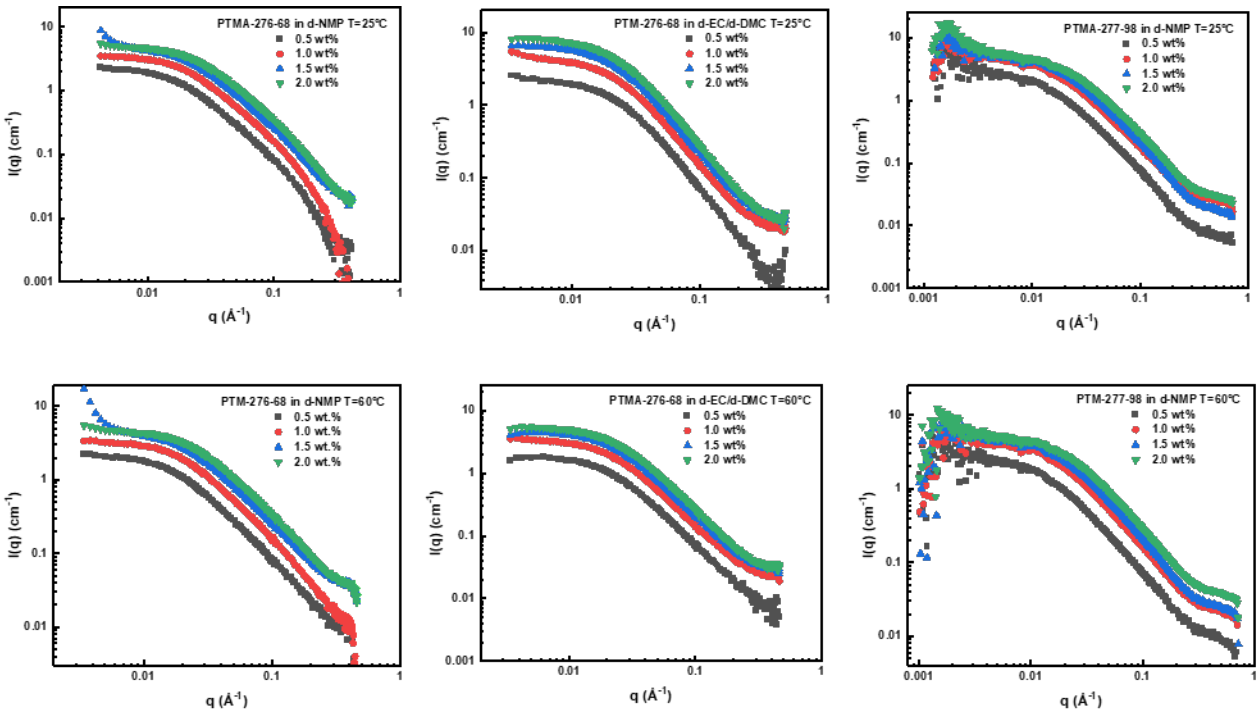

Figure 39. Small-angle neutron scattering profile of PTMA-276-68 in d-NMP(left) and d-EC:d-DMC (center) and PTMA-277-98 in d-NMP (right)

In Equation 5.5, $K = \Delta\rho^2 V_m \phi / N_A$ is the contrast factor, V_m is the molar volume of PTMA-X-R (202.5 cm^3/mol), Φ is the volume fraction of PTMA-X-R in solution, N_A is the Avogadro's constant, M_w is the PTMA weight average molecular weight, A_2 is the second virial coefficient which describes the polymer-solvent interactions. Therefore, Zimm analysis provides information on the quality of the solvent, as well as serves as a supplement to the Guinier analysis by providing the M_w and R_g of the polymer. However, in our initial Zimm analysis, the results of which are tabulated in Table 16 (pg. 198 in Appendix), shows a significant variation in the molecular weight of PTMA-X-R in different solvent conditions. This is physically unreasonable and must be an artifact of the analysis. To identify this artifact, the concentration dependence of the scattering of PTMA-X-R in each solvent was investigated. Equation 5.6 shows that the scattering of individual scattering particles in solution scales with concentration.

$$I(q) \sim \Delta\rho^2 \times c \times F(q) \times S(q) \qquad \textbf{5.6}$$

In Equation 5.6, $\Delta\rho^2$ is the difference in the scattering length density of the solvent and the polymer. The scattering length density (SLD) of each atomic species can be calculated from its density and atomic composition. Initially, the SLD of PTMA-X-R, and the solvents d-NMP and d-EC:d-DMC are calculated to be 0.918E-06 $Å^{-2}$, 6.20E-06 $Å^{-2}$, 5.40E-06 $Å^{-2}$ respectively. F(q) in Equation 5.6 is the form factor that depends on the structure/conformation of the PTMA polymer. In these experiments the conformation of the PTMA-X-R polymer does not change with solution composition, thus F(q) does not change. Lastly, S(q) is the structure factor that details the particle-to-particle interaction, and, in this case, since the polymer solution is dilute, the S(q) is 1.

Therefore, if the coherent scattering of PTMA-X-R in a given solvent is normalized by the concentration of the polymer, Equation 5.6 shows that the scattering profiles should overlap. When

normalized to concentration, the PTMA-276-68 dissolved in d-EC:d-DMC at 25°C shows the expected collapse of all scattering curves, as shown in Figure 40. In contrast, the normalization of the scattering curves with concentration of all other solutions showed a decrease in scattering intensity with an increase in concentration, as shown in Figure 63 (pg. 199 in Appendix).

Equation 5.6 shows that the most likely parameter that could account for this unexpected result is an incorrect value of the scattering length density of the solvent, which translates to an incorrect value of $\Delta\rho^2$ in Equation 5.6. We interpret this to indicate that the molecular composition of the solvent is not pure NMP or EC:DMC, but must include the presence of counterions associated with the PTMA.[186] These counter-ions alter the SLD of the solvent and must be accounted for. Moreover, this also emphasizes that the scattering length densities of the solvent for a series of concentrations are not constant; rather, it varies with the amount of counter ion in the solvent. The results show that the SLD of the solvent decreases with increasing PTMA (and counter ion). To account for this deviation of the solvent SLD from the SLD of the pure solvent, the corrected SLD, which accounts for counterion present, is determined from Equation 5.7.

$$\Delta\rho^2{}_{corrected} = \frac{\Delta\rho^2{}_{theoretical} \times I(0)_{experiment}}{I(0)_{theoretical}} \qquad \textbf{5.7}$$

In Equation 5.7, $\Delta\rho^2_{corrected}$ is the corrected contrast between solvent and polymer to account for the presence of the counter-ion whereas $\Delta\rho^2_{theoretical}$ is the theoretical contrast between the pure solvent and polymer, $I(0)_{experimental}$ is the forward scattering of the experimental SANS profile of PTMA-X-R polymer and $I(0)_{theoretical}$ is the forward scattering of the SANS profile obtained using Equation 5.3, where M_w= molecular weight of the PTMA-X-R polymer obtained from Guinier analysis= ~142 kg/mol, d=density of the polymer, N_A= Avogadro's number, φ= volume fraction of the polymer. The fact that the scattering of the room temperature solution of PTMA-276-68 in d-

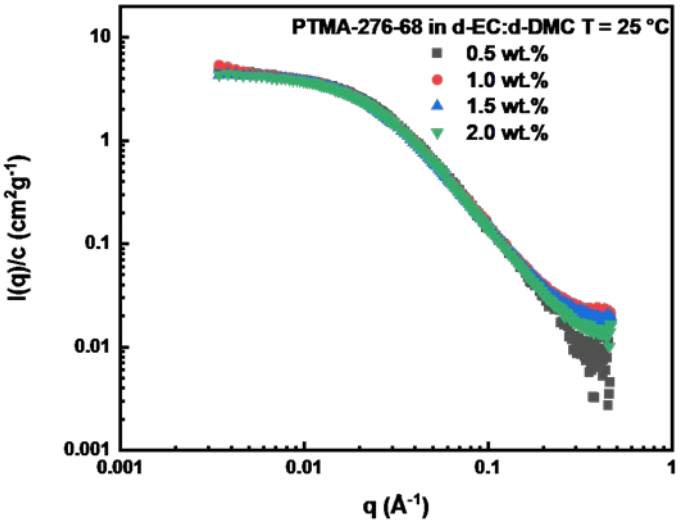

Figure 40. Normalized SANS scattering profile of PTMA-276-68 in d-EC:d-DMC provides a master curve.

EC:d-DMC scales with concentration enables the use of the molecular weight value obtained from the Guinier analysis of this sample in these calculations.

Following this approach provides the proper contrast parameter $\Delta\rho^2$ of all the polymer solutions, resulting in scattering patterns that scale with concentration, and can be analyzed by the Zimm analysis.

Figure 64 (pg. 200 in Appendix) plots the SLD of the solvent as a function of PTMA concentration for the d-EC:d-DMC solutions at 60 °C, where extrapolation of the SLD to zero PTMA concentration gives a value of the SLD (5.20 E-06 $Å^{-2}$) that is very similar to that of the estimated SLD of the pure d-EC:d-DMC mixture (5.40E-06 $Å^{-2}$). Therefore, the SLD of the solvent is corrected to account for counter-ions for all samples, and the data is then re-analyzed. For example, Figure 41 shows the scattering curves of the PTMA-276-68 in d-EC:d-DMC at 60 °C normalized to concentration, where the data collapse to a single curve. The results of the Zimm analyses of the SLD corrected data for all solutions are presented in Table 8.

Inspection of the Zimm analyses results presented in Table 8 shows consistent molecular weights of the PTMA for all solutions. The modest variation in molecular weight of PTMA-277-68 in d-NMP with temperature is attributed to the low signal-to-noise ratio of the scattering profile. Although the second virial coefficient shows variation with the change in solvents and temperature, these values are at least an order of magnitude smaller than A_2 of a polymer in a good solvent (10^{-4}-10^{-5} mol cm^3 g^{-2}), and are therefore close to 0. This indicates that all the solvents are marginal solvents for the PTMA polymer under all conditions. However, the subtle variation in second virial coefficients resonates with the variation of the radius of gyration of the PTMA polymer in d-NMP and d-EC:d-DMC. For instance, the radius of gyration of PTMA-276-68 is 90 Å in d-NMP at 25°C, whereas in d-EC:d-DMC the radius of gyration decreases to 80 Å, which corresponds to

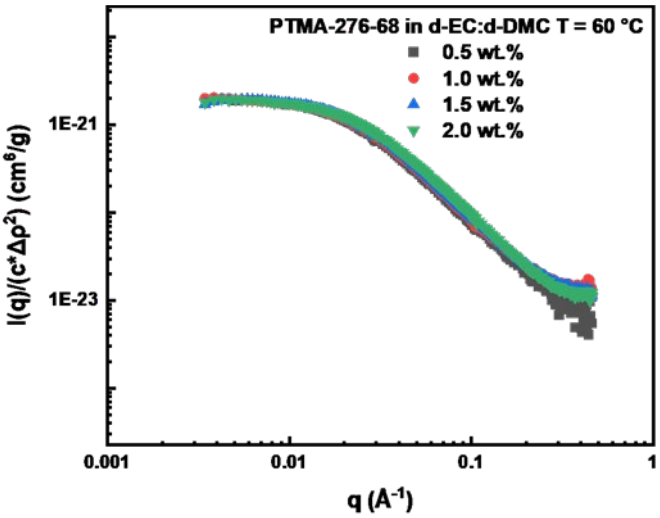

Figure 41. Corrected scattering profile of PTMA276-68 in d-EC:d-DMC at 60 °C

Table 8. Summary of second virial coefficients (A_2), radius of gyration (R_g) and molecular weights (M_w) of PTMA-276-68 in d-NMP and d-EC:d-DMC and PTMA-277-98 in d-NMP at 25°C and 60°C

Sample Name	Solvent, Temperature	A_2 ± error (mol cm^3 g^{-2})	M_w (kg/mol)	R_g ± error (Å)
PTMA-276-68	d-NMP, T = 25 °C	3.09E-06 ± 2.015E-06	141	90 ± 5
PTMA-276-68	d-NMP, T = 60 °C	7.69E-06 ± 9.05E-07	143	85 ± 4
PTMA-276-68	d-EC:d-DMC, T = 25 °C	-2.37E-06 ± 3.60E-06	144	80 ± 4
PTMA-276-68	d-EC:d-DMC, T = 60 °C	9.64E-07 ± 3.93E-07	142	75 ± 4
PTMA-277-98	d-NMP, T = 25 °C	6.20E-06 ± 4.71E-06	143	117 ± 6
PTMA-277-98	d-NMP, T = 60 °C	1.56E-05 ±1.41E-05	150	111 ± 6

a slight decrease in the A_2 and the quality of the solvent.

Similarly, the A_2 of PTMA-277-98 in d-NMP is marginally higher than that of the PTMA-276-68 in d-NMP, suggesting that NMP is a slightly better solvent (though still marginal) for the polymer with higher radical content. It is interesting that although the A_2 of the PTMA-277-98 in d-NMP is modestly greater than that of PTMA-276-68 in d-NMP, the radius of gyration of the PTMA-277-98 increases by *ca.* 27 Å. We interpret this to indicate that the repulsion between radicals on the same chain dominates the conformation more than the polymer-solvent interaction, where the increase in radical content from 68% to 98% forces the PTMA chain to expand in the d-NMP. This repulsion is an important consideration in the electron transfer rate within a solvent swollen polymer electrode.

Polymer-solvent interaction parameters for PTMA solutions

To compare the conformation determined using SANS to other indicators of solvent quality, the Flory Huggins (polymer-solvent) interaction parameter, χ, was determined from the experimentally determined second virial coefficient. χ larger than 0.5 indicates a "poor" solvent, whereas values smaller than 0.5 indicate a "good" solvent, and χ values of 0.5 typically indicate a theta solvent. In a good solvent, an expanded chain is expected due to favorable interactions between the polymer and solvent. In contrast, in a poor solvent, a collapsed chain is expected to minimize interactions between the polymer and solvent. Using the total Hansen solubility parameters for the polymers and solvents, χ was calculated for both polymers in d-NMP and PTMA-276-68 in d-EC:d-DMC using Equation 5.1 (summarized as group contributions in Table 9). Additionally, the A_2 values from Zimm analysis were used to calculate the experimentally determined interaction parameters from Equation 5.2.

As expected, as the temperature increases from 25 °C to 60 °C, the calculated χ value decreases, indicating more favorable interactions between the polymer and solvent, which should correlate to a more expanded chain conformation. Overall, χ values obtained from group contribution analysis indicate that NMP is a good solvent for the polymer ($\chi < 0.5$) and EC:DMC is a poor solvent ($\chi > 0.5$) for the polymer. However, the experimentally determined χ values do not show this same solvent and temperature dependence. All of the SANS determined χ values indicate a marginal solvent that is very close to a theta solvent, regardless of temperature or solvent. These results strongly suggest that the approximations that are used in calculating the χ values using group contribution analysis overestimate the similarity of the Hansen Solubility parameters of the polymer and solvent. Given the importance of the presence of counter-ions in the analyses of the scattering curves, we suspect that not accounting for the presence of the counter-ion in estimating the polymer-solvent thermodynamic interactions is a significant source of error. Therefore, future attempts to estimate χ values of radical polymers must account presence of the counter-ion in group contribution analysis.

Fractal Dimension Analysis

The scattering curve can also be used to determine the fractal dimension, D, of the polymer chain by focusing on the scattering over the q range $1/R_g < q < 1/b$, which focuses on the length scales below the radius of gyration (R_g) and above the statistical length (b) of the polymer. The scattering of a fractal object is related to its fractal dimension by the following relationship-

$$I(q) \propto q^{-D} \quad \textbf{5.8}$$

Therefore, analysis of a log I(q) vs. log (q) plot provides a quantitative measure of the fractal dimension of a polymer in solution.[139,200–202] The Fractal dimension, D, of a polymer is related to its Flory exponent, υ, as $D = 1/\upsilon$.[203] Therefore, a Fractal dimension (D) of 2 corresponds to

Table 9. The polymer-solvent interaction parameters (χ) calculated from the second virial coefficient (SANS) and from group contribution estimates of the polymer solubility parameters (group contribution).

Polymer	Solvent	Group Contribution		SANS	
		$\chi_{25\ °C}$	$\chi_{60\ °C}$	$\chi_{25\ °C}$	$\chi_{60\ °C}$
PTMA-276-68	d-NMP	0.38	0.37	0.50	0.50
	d-EC:d-DMC	0.64	0.60	0.50	0.50
PTMA-277-98	d-NMP	0.36	0.35	0.50	0.50

Flory exponent, $\upsilon = 0.5$, which indicates that the polymer chain attains a random walk conformation. This condensed chain corresponds to the conformation of a coiled polymer in a theta solvent. A fractal dimension in the range of $1.66 < D < 2$ corresponds to a polymer chain with a Flory exponent, $0.5 < \upsilon < 0.60$, which is the expected conformation in a better solvent. In a good solvent, the polymer will follow a self-avoiding walk, $\upsilon = 0.6$, which corresponds to $D = 1.66$. A polymer chain with a fractal dimension of less than 1.66 ($\upsilon < 0.6$) corresponds to a polymer chain that is semi-flexible and more swollen than that of a polymer in a good solution.[204]

Figure 65 (pg. 201 in Appendix) shows a representative fractal dimension fit, in this case for the 0.5 wt.% PTMA-276-68 in d-NMP. Table 10 summarizes the Fractal dimensions of all 0.5 wt.% solutions of PTMA-X-R at different temperatures. The fractal dimension of PTMA-276-68 in NMP is 1.66 and 1.58 at 25 °C and 60° C, which corresponds to a self-avoiding walk at room temperature that expands to a semi-flexible conformation at 60 °C. The fractal dimension of the same polymer in d-EC:d-DMC at room temperature is 2.0 ($\upsilon = 0.5$), signifying a more collapsed conformation that mimics a random walk. This analysis is consistent with the Zimm analysis that showed that the R_g of this polymer in d-EC:d-DMC is about 10 Å smaller than in d-NMP. At 60 °C, the fractal dimension of the PTMA-276-68 in d-EC:d-DMC is 1.78 ($\upsilon = 0.56$), indicating that polymer chain has expanded, but has not yet attained the conformation of a self-avoiding walk that would be expected in a good solvent. The fractal dimensions of the PTMA with higher radical loading, PTMA-277-98, in d-NMP are 1.47 and 1.41 at 25 °C and 60 °C respectively. This corresponds to $\upsilon \sim 0.68\text{-}0.70$, further quantifying the increase in semi-flexibility of the PTMA with increased radical loading, which also correlates to an increased R_g of this polymer over that of the PTMA with lower radical loading, PTMA-276-68.

Table 10. Fractal dimension of 0.5 wt.% PTMA-X-R at 25 °C and 60 °C.

Sample Name	Fractal dimension T=25 °C	Flory Exponent T=25 °C	Fractal dimension T= 60 °C	Flory Exponent T=60 °C
PTMA-276-68 in d-NMP	1.66	0.60	1.58	0.63
PTMA-276-68 in d-EC:d-DMC	2.0	0.50	1.78	0.56
PTMA-277-98 in d-NMP	1.47	0.68	1.41	.70

Molecular weight dependence of R_g

Figure 42 plots the molecular weight dependence of the radius of gyration of PTMA-X-R oxidized using H_2O_2 in d-NMP. This analysis provides further insight into the effect of radical loading on the conformation of the PTMA chain. The R_g of PTMA-15-72, PTMA-44-87, PTMA-122-95, and PTMA-277-98 in 1 wt.% as determined from the Guinier model fit of the scattering profiles is plotted as a function of the I(q=0), which is proportional to the polymer molecular weight in Figure 42. The plot in Figure 42 shows that the dependence of $R_g \propto I(0)^{0.63}$. This is slightly larger exponent than is expected from an ideal Gaussian chain that follows self-avoiding walk statistics.[204] The observed exponent of 0.63 further quantifies the extent to which the PTMA polymer with higher radical content can be thought of semi flexible, as it is slightly more rigid than a Gaussian coil.

Electrochemistry of PTMA

The electrochemical properties of PTMA thin films were investigated using cyclic voltammetry (Figure 43) and galvanostatic charge/discharge in a 3-electrode beaker cell with the PTMA thin film on glassy carbon working electrodes, Pt wire counter electrode, Ag/AgCl (sat.) reference electrode, and 0.5 M $TEABF_4$ in water as supporting electrolyte. The cyclic voltammograms demonstrate that regardless of oxidation method and casting solvent PTMA-X-R exhibited similar half-wave ($E_{1/2}$) redox potentials of 0.78 V *vs.* Ag/AgCl at 10 mV/s. Similarly, all of the films exhibited a linear relationship between peak current and the square root of scan rate, which is indicative of a diffusion limited reaction.

In contrast, there were distinct differences in the slope of the linear relationship between peak current and the square root of scan rate for the three samples. In oxidation, the PTMA-276-68 thin film cast from EC:DMC had the largest slope, followed by PTMA-276-68 cast from NMP,

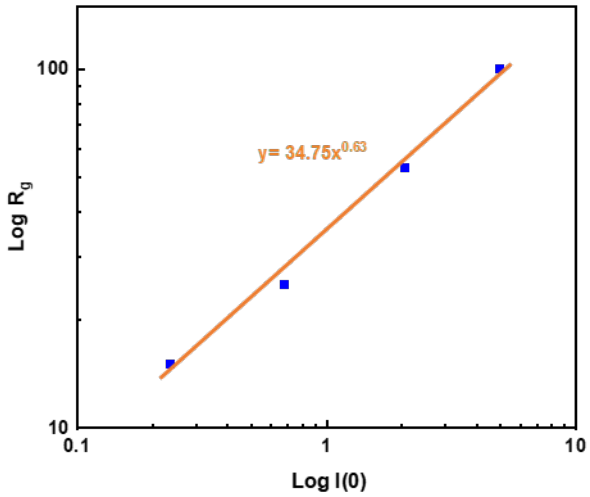

Figure 42. log R_g vs Log I(0) plot of PTMA-X-R oxidized by H_2O_2 with similar oxidation level (~98%)

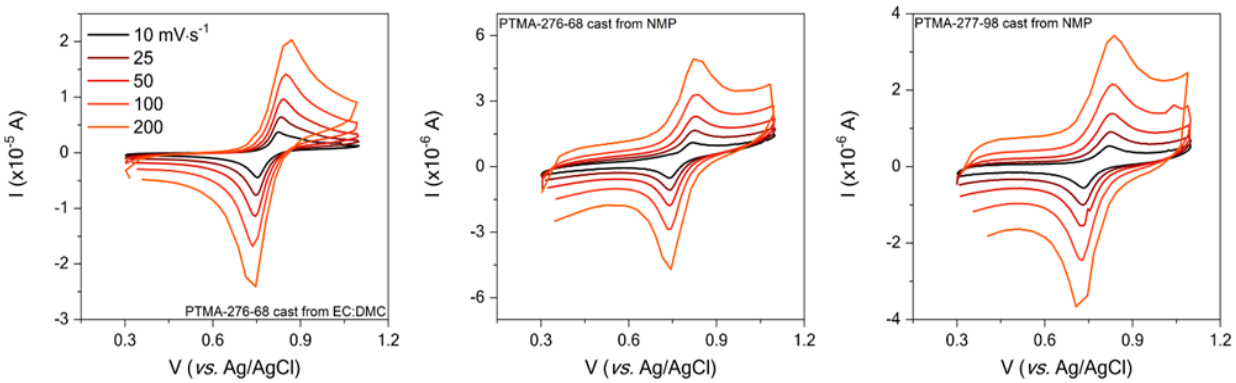

Figure 43. Cyclic voltammograms for PTMA-276-68 thin films cast from (left) EC:DMC solution and (center) NMP solution and for (right) PTMA-277-98 cast from NMP solution. The cyclic voltammograms were obtained in a three-electrode beaker cell with the PTMA-X-R thin films on glassy carbon working electrodes, Pt wire counter electrode, Ag/AgCl (sat.) reference electrode, and 0.5 M $TEABF_4$ as supporting electrolyte in water.

and PTMA-277-98 cast from NMP. These slope values, from Figure 67 (pg. 202 in Appendix), were used to determine the diffusion coefficient following the Randles-Sevcik equation (Equation 5.9).

$$i_p = (2.69 \times 10^5) n^{3/2} A C D^{1/2} v^{1/2} \quad \textbf{5.9}$$

where I_p is the peak current (A), n is the number of electrons, A is the electrode area (cm^2), C is the concentration of redox-active sites (mol/mL), v is the scan rate (V/s), and D is the diffusion coefficient (cm^2/s). This analysis results in D of 3.0×10^{-13} cm^2/s for the PTMA-276-68 EC:DMC cast film and 1.5×10^{-14} cm^2/s for the PTMA-276-68 NMP and PTMA-277-98 cast films. This variation could be due to the more extended conformation for PTMA-276-68 and PTMA-277-98 in NMP, which leads to a more densely packed thin film and a reduced diffusion within the film relative to the EC:DMC cast film.

These results are similar for the kinetic parameters obtained from chronoamperometry documented in Table 11 and the charge-discharge performance that is shown in Figure 69 (pg. 204 in Appendix). The more compact structure of PTMA-276-68 in EC:DMC suggest that the films contain globular compact coils, which could facilitate intra- and inter- transport in the amorphous polymers, as compared to the extended conformation compact films favoring inter-chain transport to the glassy carbon surface.

Discussion

To understand the charge transport of non-conjugated PTMA polymer, it is imperative to understand the conformation of the polymer in solvents that are frequently used in fabrication and operation of batteries. Moreover, previous theoretical and experimental studies have shown that the PTMA polymer conformation and assembly varies with radical loading.[47,51] Therefore, to

Table 11. Electron transfer rate constants for PTMA-X-R thin films cast from two different solvents.

Polymer	Casting Solvent	$\log (k_{eff})$	$\log (D_{et})$	$\log (k^0)$
PTMA-276-68	EC:DMC	2.6	-12.4	-6.1
	NMP	1.0	-14.0	-7.0
PTMA-277-98		0.8	-14.2	-7.3

rationally guide the design and fabrication of organic radical polymers, a more thorough understanding of the impact of polymer molecular weight, radical loading, and temperature in battery relevant solvents is needed. Small-angle neutron scattering experiments provide the structure, assembly, and thermodynamic interactions of PTMA-X-R chains in battery-relevant solvents. Interestingly, the initial Zimm analysis clearly indicates that the solvent is more complex than initially thought. Careful consideration revealed that the counter-ions that are present in the solution must be accounted for in further analyses of the scattering data. With this correction, the Zimm analysis provides second virial coefficients that quantify the polymer solvent thermodynamic interactions, which indicates that all the solvents are marginal for the PTMA chains regardless of solvent, temperature, molecular weight, or radical loading. Moreover, comparison of the estimated Flory-Huggins interaction parameter from Hansen parameter group contributions and the SANS derived experimental values shows significant discrepancies. These inconsistencies are attributed to the assumption that the counter-ion does not impact the polymer-solvent interaction in the calculated estimation of χ.

The Zimm analysis also provides the radius of gyration of the polymers as a function of solvent, temperature, and radical loading, which are consistent with the fractal dimension analysis. These analyses demonstrate that the PTMA polymer chains expands in d-NMP more than it does in the d-EC:d-DMC, where the radius of gyration of the PTMA with more radical loading, PTMA-277-98, is significantly larger than that of the PTMA with lower radical loading, PTMA-276-68. This indicates that the molecular conformation of the organic radical polymer is dominated by the amount of radical loading present in the polymer backbone more than the solvent type and temperature. These results clearly indicate that increasing the radical loading increases the stiffness

in the backbone of PTMA-X-R polymer. The increase in rigidity in the polymer backbone with increased radical loading has also been observed by Martin et al. in deuterated acetonitrile.[51]

This information on the conformation and thermodynamic interactions of PTMA-X-R polymer in different solvents correlates with the electrochemical performance of the polymer in solid state formed from these solvents. The higher diffusion coefficient in the PTMA-276-68 film cast from EC:DMC is consistent with the compact shape of the polymer in solution, which forces the TEMPO radicals to assemble close to each other, allowing for more rapid charge transfer in the system. Previous theoretical studies have also provided evidence of increased charge diffusion in PTMA films when the PTMA chains are more collapsed to ease the hopping of the electron from one radical to another.[47] This work suggests that use of a processing solvent that results in a collapsed chain conformation when casting electrodes will help to enhance the rate of charge transfer and improve the capacity performance.

Conclusion

Small-angle neutron scattering results document the conformation, assembly, and thermodynamic interactions of PTMA-X-R in battery relevant solvents. These results document the impact of solvent, radical loading, and temperature on polymer conformation. Careful Zimm analysis demonstrates that the presence of counter ions in the solvent must be accounted for in the analyses. When these are accounted for, it is clear that the NMP and EC:DMC are marginal solvents for the PTMA. Moreover, comparison of these experimental χ values to those found from Hansen parameter group calculations emphasizes the need to account for the presence of the counter-ion in determining the polymer-solvent interaction parameter, χ using Hansen parameter group calculations.

Further correlation of the SANS determined second virial coefficients to the R_g indicates the NMP is a marginally good solvent and EC:DMC is a marginally poor solvent for the PTMA chains. This corresponds to a slightly swollen PTMA chain in d-NMP and a slightly collapsed PTMA chain in d-EC:d-DMC. The fractal dimensional analysis further quantifies the change in the PTMA conformation with a change in solvent or radical loading. These results show that the PTMA chain with lower radical loading, PTMA-276-68 attains a self-avoiding walk conformation while the PTMA chain with the higher radical loading, PTMA-277-98, expands and attains a more semi-rigid conformation. Similarly, for both radical loadings fractal dimension analysis shows that an increase in temperature contributes to further expansion of the polymer chain. A holistic interpretation of the entire analyses presented emphasizes that the conformation of the organic radical PTMA chain is primarily driven by the radical loading, while solvent choice and temperature are important, but secondary governing factors.

Moreover, the electrochemical performance of PTMA films formed from each solvent are consistent with these conformations. The electrochemical results suggest that the radicals of PTMA-276-68 in EC:DMC are more closely packed, as would be expected with a more compact conformation, which drives improved inter and intrachain charge diffusion. Finally, future efforts should focus on the identification of electrode processing solvents that result in a collapsed chain conformation of the organic radical polymer leading to improved capacity performance in organic batteries.

Acknowledgment

Research supported as part of the Breakthrough Electrolytes for Energy Storage (BEES), an Energy Frontier Research Center funded by the U.S. Department of Energy (DOE), Office of Science, Basic Energy Sciences (BES), under Award DE-SC0019409 (neutron scattering

experiments and analysis). We acknowledge the support of the National Institute of Standards and Technology, U.S. Department of Commerce, in providing the neutron research facilities used in this work. A portion of this research was also completed at the High Flux Isotope Reactor a DOE Office of Science User Facility operated by the Oak Ridge National Laboratory. This work benefited from the use of the SasView application, originally developed under NSF award DMR-0520547. SasView contains code developed with funding from the European Union's Horizon 2020 research and innovation program under the SINE2020 project, grant agreement No 654000. An acknowledgment is made to the Donors of the American Chemical Society Petroleum Research Fund for partial support of this work (solubility parameter). This work was supported by grant DE-SC0014006 funded by the US Department of Energy, Office of Science (electrochemistry). A.D.E. acknowledges support by the National Science Foundation Graduate Research Fellowship under Grant No. DGE:1746932.

Chapter VI Conclusion and Future Work

Conclusion

The application of soft materials in energy storage systems can be a vital solution for a sustainable future. The functionality of soft materials greatly depends on the structure, conformation and assembly of soft structures in solutions. Thus, neutron scattering is applied to investigate the structure and conformation of energy relevant polymeric materials for potential application in energy storage systems. Small angle neutron scattering is used to investigate the molecular level assembly and structure of Nanoparticle Organic Hybrid Materials (NOHMs) in solution with and without the presence of supporting electrolytes. Neutron reflectivity is used to understand the impact of the ordering of NOHMs near electrode surfaces. Finally, small angle neutron scattering is used to elucidate the conformation and thermodynamic interaction of poly(2,2,6,6-tetramethylpiperidinyloxy-4-yl methacrylate) or PTMA in application relevant solvents with varying radical loading.

Structure and assembly of NOHM-I-HPE in aqueous solutions

The successful implementation of NOHMs in an energy storage system requires a thorough understanding of the structure and assembly of the NOHMs in solution with and without supporting electrolyte. Small angle neutron scattering results showed that with increasing concentration of NOHM-I-HPE (10-40 wt.%), the amount of free polymer in solution increases due to the detachment of grafted polymer from the nanoparticle surface. These free polymer interact with the grafted polymer, which impacts the structure of the NOHM-I-HPE and creates an assembly that consists of functionalized silica nanoparticles with grafted polymer, interacting polymer and free polymer in solution. The addition of supporting electrolyte 0.1M $KHCO_3$ in the solution further alters the assembly of NOHMs by collapsing the size of the free polymer. Consequently, a reduction in the interaction of the free polymer with the grafted polymer occurs

which increases the effective thickness of the grafted polymer. Moreover, the results also suggest that the salt ions (K^+) act as a counter-ion and compete with the HPE polymer canopy for the functionalized silica surfaces. This results in further the detachment of grafted polymer from the nanoparticle surface. Comparison of the conformational results with the rheology of the solution shows that the dramatic reduction of the viscosity of ionic NOHMs is consistent with the slippage of grafted polymer layer from the nanoparticle surface.

Impact of bond type on the structure and assembly of NOHMs in aqueous solutions

The unique opportunity to alter the grafting bond type in NOHMs provides pathways to tune the functionalities of NOHMs. Small angle neutron scattering is used to investigate the impact of altering the bonding motif on the structure and assembly of unbound HPE polymer, NOHM-I-$HPE_{0.8}$, NOHM-C-$HPE_{0.5}$, and NOHM-C-$HPE_{0.7}$ in aqueous solution with and without the presence of supporting electrolyte 0.1M $KHCO_3$. Our results highlight that free polymer exists in the solution even at low concentrations (1-3 wt.%) in the NOHM-I-HPE solutions. Comparison of the size of the free polymer with the size of the unbound HPE polymer in NOHM solutions indicates that the addition of nanoparticles decreases the size of the HPE polymer. Moreover, the free polymer in the NOHM-I-HPE solution interacts with the grafted layer and decreases the effective thickness of the grafted layer. With the change in the bonding motif of the grafted layer to a covalent moiety, both aggregated and dispersed NOHM-C-HPE particles are observed. Moreover, the exclusion of the detachment of the grafted polymer through the introduction of covalent grafting resulted in a grafted layer thickness that is higher for NOHM-C-HPE than in the NOHM-I-HPE particles. The addition of 0.1M $KHCO_3$ supporting electrolyte in the NOHMs solutions show a collapse of the free polymer and grafted polymer of NOHM-I-HPE on the nanoparticle surface resulting in a significant decrease in the thickness of the grafted layer.

Consequently, a decrease in the overall size of the NOHM-I-HPE nanoparticle is observed. In contrast, a nominal decrease in grafted layer thickness is observed for NOHM-C-HPE particles with the presence of supporting electrolyte. Comparison of the viscosity results with the structure and assembly of ionic and covalent NOHMs shows an increased viscosity of covalent NOHMs consistent with the aggregated particles observed in the solution. Additionally, a dramatic decrease in the viscosity of the NOHM-I-HPE solution is observed with the addition of 0.1M $KHCO_3$ supporting electrolyte, which is a direct result of the decrease in the global size of the ionic NOHMs particle with the collapse of the grafted polymer on the nanoparticle surface.

Assembly of HPE and NOHM-I-HPE near an electrode surface

In order to understand the electrochemical performance of HPE and NOHM-I-HPE as components in an electrochemical environment, it is essential to understand their assembly and ordering near the surface of an electrode. Neutron reflectivity is used to investigate the ordering of unbound HPE and NOHM-I-HPE in aqueous solution in the presence of supporting electrolyte near electrode surfaces that are modified with varying surface chemistry/hydrophilicity. The results indicate multiple layers of unbound HPE polymer sequester near an electrode surface with and without supporting electrolyte. In the presence of NOHM-I-HPE, along with a layer of free polymer, a layer of NOHM-I-HPE particle assembles near the electrode surface. This ordering of unbound HPE polymer, free polymer and NOHM-I-HPE particles does not vary with change in hydrophilicity of the electrode. Additional experiments of NOHM-I-HPE solution in the presence of $ZnCl_2$ with varying potential shows that the ordering of free polymer NOHM-I-HPE particle does not vary with addition of $ZnCl_2$ at 0V; however, the thickness of the free polymer and grafted layers decrease in the z direction. In contrast, with the application of potential the ordered layer of NOHM-I-HPE particle near the electrode surface disappears. Along with deposition of Zn salt, a

higher amount of free polymer assembles on the surface. These results highlight that the assembly of increased free polymer near the electrode surface is consistent with the smooth deposition of Zn salt on the electrode surface, which may inhibit dendrite formation. Furthermore, the assembly of free polymer in NOHM-I-HPE contributes to the increased current density compared to the assembly of unbound HPE polymer near the electrode surface.

Conformation of PTMA with variation in solvent, temperature, and radical loading

The introduction of PTMA in organic radical batteries broadens the opportunities to achieve sustainable energy storage systems that require less dependency on costly materials such as lithium, cobalt, and nickel. To achieve an improved and functional PTMA-based organic energy storage systems, it is important to understand the conformation and assembly of PTMA in battery relevant solvents with varying radical loading and temperature. Small angle neutron scattering results show that N-methyl-2-pyrrolidone (NMP) and a 50:50 (wt.%) ethylene carbonate:dimethyl carbonate (EC:DMC) mixture are considered theta solvents for the PTMA polymer due to the presence of counter-ion associated with PTMA polymer. Comparison of the polymer-solvent interaction parameter, χ values obtained using Hansen group contribution calculation with the experimental results also emphasizes the importance of accounting for counter-ion to understand the quality of the solvents. Further results indicate that the PTMA polymer collapses in the EC:DMC solvents and swells in the NMP solvents. The extent of swelling of PTMA depends on the amount of radical loading (68% vs. 98%) on the polymer chain, where an increased radical loading shows an increase in the size of the polymer due to backbone rigidity. While the size of PTMA polymer with 68% radical loading increases at higher temperature, careful analysis of the SANS results indicates that a higher amount (98%) of radical loading attains a swollen conformation of the PTMA, thus indicating that solvent choice and/or temperature are the

secondary driving factors for a change in conformation of PTMA polymer. Finally, correlating the conformation results of PTMA with the electrochemical performance of thin films of PTMA shows that the collapsed nature of PTMA in solvent contributes to higher charge transfer in the electrochemical process.

Future Work

The results presented in this work show that SANS and NR are powerful characterization tools to examine the structure and assembly of NOHMs in an aqueous solution in the presence of a supporting electrolyte and conformation of PTMA in two different solvents at two different temperatures and radical loading. Further experiments would benefit our understanding of the structure and conformation of these polymeric materials to correlate their performance in energy storage systems.

Impact of unbound polymer in the assembly and dispersion of NOHM-C-HPE

Our results show that NOHM-I-HPE consists of free polymer in the solution that interacts with the grafted polymer and changes the assembly of the neat NOHMs structure. In NOHM-C-HPE, the polymer is covalently grafted; hence polymer cannot detach from the functionalized nanoparticle surface. It is hypothesized that the presence of free polymer in the NOHM-I-HPE solution can be a potential solution to inhibit the aggregation observed in NOHM-C-HPE solution. Hence, further experiments with the addition of unbound HPE polymer into the NOHM-C-HPE solution will be performed to investigate the assembly and structure of NOHM-C-HPE in presence of free polymer. This will potentially answer the fundamental question of the contribution of the unbound polymer to the uniform dispersion of NOHM-C-HPE. Selective deuteration of unbound HPE polymer will be beneficial to distinguish grafted polymer from unbound polymer to clearly

understand the conformation of free polymer and the conformation of grafted polymer NOHM-C-HPE. Hence, SANS must be used as a characterization tool to perform these experiments.

Ordering of unbound HPE polymer and NOHM-C-HPE in an electric field

Small-angle neutron scattering results in Chapter 2 and Chapter 3 showed that the structure of NOHM-I-HPE in an aqueous solution is quite complex, consisting of grafted polymer, interacting polymer and free polymer. This complex assembly of the NOHMs-based fluid can impact the performance of NOHMs in an electrochemical environment. The reflectivity results in Chapter 4 showed that in NOHM-I-HPE aqueous solution, the free polymer first adsorbs on the Au surface and then a layer of NOHMs orders near the surface. When a negative potential is applied, the ordering of the structure drastically changes and the ordered NOHMs are disrupted but more protonated HPE polymer approaches the surface. To better understand the effect of potential on NOHM-I-HPE, it is essential to investigate the ordering of unbound HPE polymer near the surface with an applied potential. Moreover, investigating the ordering of NOHM-C-HPE will provide a holistic understanding of the impact of bond type on the electrochemical performance of NOHMs. Thus, neutron reflectivity should be used to monitor the ordering of HPE and NOHM-C-HPE in a similar experimental approach followed for the NOHM-I-HPE solution with and without the presence of supporting electrolyte with varying potential ranging from 0V to -1.5V.

Conformation of PTMA in the bulk

Small angle neutron scattering studies of PTMA in Chapter 5 shows that the collapsed polymer chain of PTMA in dilute solutions contributes to the increased charge transfer in thin film structures of PTMA. Previous molecular dynamics study has shown that in thin films, PTMA can organize itself in three different molecular arrangements that contribute to charge transfer.[47]

Moreover, a similar nitroxide radical-based polymer with a polyethylene oxide backbone, poly(4-glycidyloxy-2,2,6,6-tetramethylpiperidine-1-oxyl) or PTEO posits that a percolating structure of the polymer chain at a small length scales in bulk (thin films) contributes to the increased conductivity.[205] However, no such experimental studies have been reported that investigate the conformation of PTMA or PTEO polymer chains in the bulk material. Hence, future studies will be conducted to investigate the molecular rearrangement of PTMA in the bulk material. To conduct these studies, a deuterated version of PTMA polymer (d-PTMA), a protonated version of the PTMA polymer (H-PTMA) and a PTMA polymer with protonated backbone and deuterated TEMPO group (d-TEMPO PTMA) will be synthesized. The blends of these synthesized polymer will be used to conduct small angle neutron scattering experiments that will provide a fundamental understanding of the charge transfer process in the non-conjugated amorphous polymer chains.

References

(1) Renewable Energy Agency, I. Global Energy Transformation: A Roadmap to 2050. **2018**.

(2) *U.S. Energy Information Administration. Annual Energy Outlook 2022*; 2022.

(3) Rodby, K. E.; Perry, M. L.; Brushett, F. R. Assessing Capacity Loss Remediation Methods for Asymmetric Redox Flow Battery Chemistries Using Levelized Cost of Storage. **2020**. https://doi.org/10.26434/CHEMRXIV.13260233.V1.

(4) Rodby, K. E.; Carney, T. J.; Ashraf Gandomi, Y.; Barton, J. L.; Darling, R. M.; Brushett, F. R. Assessing the Levelized Cost of Vanadium Redox Flow Batteries with Capacity Fade and Rebalancing. *J. Power Sources* **2020**, *460*, 227958. https://doi.org/10.1016/J.JPOWSOUR.2020.227958.

(5) Hunter, C. A.; Penev, M. M.; Reznicek, E. P.; Eichman, J.; Rustagi, N.; Baldwin, S. F. Techno-Economic Analysis of Long-Duration Energy Storage and Flexible Power Generation Technologies to Support High-Variable Renewable Energy Grids. *Joule* **2021**, *5* (8), 2077–2101. https://doi.org/10.1016/J.JOULE.2021.06.018.

(6) Akhil, A. A.; Huff, G.; Currier, A. B.; Hernandez, J.; Bender, D. A.; Kaun, B. C.; Rastler, D. M.; Chen, S. B.; Cotter, A. L.; Bradshaw, D. T.; Gauntlett, W. D.; Eyer, J.; Olinsky-Paul, T.; Ellison, M.; Schoenung, S. DOE/EPRI Electricity Storage Handbook in Collaboration with NRECA. **2016**. https://doi.org/10.2172/1431469.

(7) Rahman, M. M.; Oni, A. O.; Gemechu, E.; Kumar, A. Assessment of Energy Storage Technologies: A Review. *Energy Convers. Manag.* **2020**, *223*, 113295. https://doi.org/10.1016/J.ENCONMAN.2020.113295.

(8) *U.S. Hydropower Market Report.*; 2021.

(9) Mai, T.; Wiser, R.; Sandor, D.; Brinkman, G.; Heath, G.; Denholm, P.; Hostick, D. J.; Darghouth, N.; Schlosser, A.; Strzepek, K. Renewable Electricity Futures Study. Volume 1: Exploration of High-Penetration Renewable Electricity Futures. **2012**. https://doi.org/10.2172/1046880.

(10) *U. S. Grid Energy Storage Factsheet.*; 2021.

(11) Weber, A. Z.; Mench, M. M.; Meyers, J. P.; Ross, P. N.; Gostick, J. T.; Liu, Q. Redox Flow Batteries: A Review. *J. Appl. Electrochem.* **2011**, *41* (10), 1137–1164. https://doi.org/10.1007/S10800-011-0348-2.

(12) Manthiram, A. An Outlook on Lithium Ion Battery Technology. *ACS Cent. Sci.* **2017**, *3* (10), 1063–1069. https://doi.org/10.1021/ACSCENTSCI.7B00288.

(13) Lu, L.; Han, X.; Li, J.; Hua, J.; Ouyang, M. A Review on the Key Issues for Lithium-Ion Battery Management in Electric Vehicles. *J. Power Sources* **2013**, *226*, 272–288. https://doi.org/10.1016/J.JPOWSOUR.2012.10.060.

(14) Diouf, B.; Pode, R. Potential of Lithium-Ion Batteries in Renewable Energy. *Renew. Energy*

2015, *76*, 375–380. https://doi.org/10.1016/j.renene.2014.11.058.

(15) Li, M.; Lu, J. Cobalt in Lithium-Ion Batteries. *Science (80-.).* **2020**, *367* (6481), 979–980. https://doi.org/10.1126/SCIENCE.ABA9168.

(16) Lee, S.; Manthiram, A. Can Cobalt Be Eliminated from Lithium-Ion Batteries? *ACS Energy Lett.* **2022**, *7* (9), 3058–3063. https://doi.org/10.1021/ACSENERGYLETT.2C01553.

(17) Liang, Y.; Tao, Z.; Chen, J. Organic Electrode Materials for Rechargeable Lithium Batteries. *Adv. Energy Mater.* **2012**, *2* (7), 742–769. https://doi.org/10.1002/AENM.201100795.

(18) Oyaizu, K.; Kawamoto, T.; Suga, T.; Nishide, H. Synthesis and Charge Transport Properties of Redox-Active Nitroxide Polyethers with Large Site Density. *Macromolecules* **2010**, *43* (24), 10382–10389. https://doi.org/10.1021/MA1020159.

(19) Oyaizu, K.; Suga, T.; Yoshimura, K.; Nishide, H. Synthesis and Characterization of Radical-Bearing Polyethers as an Electrode-Active Material for Organic Secondary Batteries. *Macromolecules* **2008**, *41* (18), 6646–6652. https://doi.org/10.1021/MA702576Z.

(20) Zhao, Y.; Ding, Y.; Li, Y.; Peng, L.; Byon, H. R.; Goodenough, J. B.; Yu, G. A Chemistry and Material Perspective on Lithium Redox Flow Batteries towards High-Density Electrical Energy Storage. *Chem. Soc. Rev.* **2015**, *44* (22), 7968–7996. https://doi.org/10.1039/C5CS00289C.

(21) Park, M.; Ryu, J.; Wang, W.; Cho, J. Material Design and Engineering of Next-Generation Flow-Battery Technologies. *Nat. Rev. Mater. 2016 21* **2016**, *2* (1), 1–18. https://doi.org/10.1038/natrevmats.2016.80.

(22) Soloveichik, G. L. Flow Batteries: Current Status and Trends. *Chem. Rev.* **2015**, *115* (20), 11533–11558. https://doi.org/10.1021/cr500720t.

(23) Wang, X.; Gautam, R. K. Strategies for Improving Solubility of Redox-Active Organic Species in Aqueous Redox Flow Batteries: A Review. *Batter. Supercaps* **2022**, *2022*, 202200298–202200299. https://doi.org/10.1002/batt.202200298.

(24) Sánchez-Díez, E.; Ventosa, E.; Guarnieri, M.; Trovò, A.; Flox, C.; Marcilla, R.; Soavi, F.; Mazur, P.; Aranzabe, E.; Ferret, R. Redox Flow Batteries: Status and Perspective towards Sustainable Stationary Energy Storage. *J. Power Sources* **2021**, *481*, 228804. https://doi.org/10.1016/j.jpowsour.2020.228804.

(25) Wei, X.; Xu, W.; Vijayakumar, M.; Cosimbescu, L.; Liu, T.; Sprenkle, V.; Wang, W. TEMPO-Based Catholyte for High-Energy Density Nonaqueous Redox Flow Batteries. *Adv. Mater.* **2014**, *26* (45), 7649–7653. https://doi.org/10.1002/adma.201403746.

(26) Shirakawa, H.; Louis, E. J.; MacDiarmid, A. G.; Chiang, C. K.; Heeger, A. J. Synthesis of Electrically Conducting Organic Polymers: Halogen Derivatives of Polyacetylene, (CH)X.

J. Chem. Soc. Chem. Commun. **1977**, No. 16, 578–580. https://doi.org/10.1039/C39770000578.

(27) Nakahara, K.; Iwasa, S.; Satoh, M.; Morioka, Y.; Iriyama, J.; Suguro, M.; Hasegawa, E. Rechargeable Batteries with Organic Radical Cathodes. *Chem. Phys. Lett.* **2002**, *359* (5–6), 351–354. https://doi.org/10.1016/S0009-2614(02)00705-4.

(28) Nishide, H.; Iwasa, S.; Pu, Y. J.; Suga, T.; Nakahara, K.; Satoh, M. Organic Radical Battery: Nitroxide Polymers as a Cathode-Active Material. In *Electrochimica Acta*; Elsevier Limited, 2004; Vol. 50, pp 827–831. https://doi.org/10.1016/j.electacta.2004.02.052.

(29) Janoschka, T.; Hager, M. D.; Schubert, U. S.; Janoschka, T.; Hager, M. D.; Schubert, U. S. Powering up the Future: Radical Polymers for Battery Applications. *Adv. Mater.* **2012**, *24* (48), 6397–6409. https://doi.org/10.1002/ADMA.201203119.

(30) Wang, S.; Easley, A. D.; Lutkenhaus, J. L. 100th Anniversary of Macromolecular Science Viewpoint: Fundamentals for the Future of Macromolecular Nitroxide Radicals. *ACS Macro Lett.* **2020**, *9* (3), 358–370. https://doi.org/10.1021/acsmacrolett.0c00063.

(31) Nugent, J. L.; Moganty, S. S.; Archer, L. A. Nanoscale Organic Hybrid Electrolytes. *Adv. Mater.* **2010**, *22* (33), 3677–3680. https://doi.org/10.1002/ADMA.201000898.

(32) Bourlinos, A. B.; Chowdhury, S. R.; Herrera, R.; Jiang, D. D.; Zhang, Q.; Archer, L. A.; Giannelis, E. P. Functionalized Nanostructures with Liquid-Like Behavior: Expanding the Gallery of Available Nanostructures. *Adv. Funct. Mater.* **2005**, *15* (8), 1285–1290. https://doi.org/10.1002/ADFM.200500076.

(33) Bourlinos, A. B.; Stassinopoulos, A.; Anglos, D.; Herrera, R.; Anastasiadis, S. H.; Petridis, D.; Giannelis, E. P. Functionalized ZnO Nanoparticles with Liquidlike Behavior and Their Photoluminescence Properties. *Small* **2006**, *2* (4), 513–516. https://doi.org/10.1002/SMLL.200500411.

(34) Rodriguez, R.; Herrera, R.; Archer, L. A.; Giannelis, E. P. Nanoscale Ionic Materials. *Adv. Mater.* **2008**, *20* (22), 4353–4358. https://doi.org/10.1002/ADMA.200801975.

(35) Rodriguez, R.; Herrer, R.; Bourlinos, A. B.; Li, R.; Amassian, A.; Archer, L. A.; Giannelis, E. P. The Synthesis and Properties of Nanoscale Ionic Materials. *Appl. Organomet. Chem.* **2010**, *24* (8), 581–589. https://doi.org/10.1002/AOC.1625.

(36) Petit, C.; Bhatnagar, S.; Park, A. H. A. Effect of Water on the Physical Properties and Carbon Dioxide Capture Capacities of Liquid-like Nanoparticle Organic Hybrid Materials and Their Corresponding Polymers. *J. Colloid Interface Sci.* **2013**, *407*, 102–108. https://doi.org/10.1016/J.JCIS.2013.05.065.

(37) Andrew Lin, K. Y.; Park, Y.; Petit, C.; Park, A. H. A. Thermal Stability, Swelling Behavior and CO2 Absorption Properties of Nanoscale Ionic Materials (NIMs). *RSC Adv.* **2014**, *4* (110), 65195–65204. https://doi.org/10.1039/c4ra10722e.

(38) Petit, C.; Lin, K.-Y. A. Y. A.; Park, A.-H. A. H. A. Design and Characterization of Liquidlike Poss-Based Hybrid Nanomaterials Synthesized via Ionic Bonding and Their Interactions with Co2. *Langmuir* **2013**, *29* (39), 12234–12242. https://doi.org/10.1021/la4007923.

(39) Moon, S.; Lee, Y.; Choi, S.; Hong, S.; Lee, S.; Park, A.-H. A.; Park, Y. Spectroscopic Investigation of Thermochemical Depolymerization of Lignin Model Compounds in the Presence of Novel Liquidlike Nanoparticle Organic Hybrid Solvents for Efficient Biomass Valorization. **2018**. https://doi.org/10.1021/acs.oprd.8b00282.

(40) Lin, K.-Y. A. Y. A.; Park, A. H. A. Effects of Bonding Types and Functional Groups on CO2 Capture Using Novel Multiphase Systems of Liquid-like Nanoparticle Organic Hybrid Materials. *Environ. Sci. Technol.* **2011**, *45* (15), 6633–6639. https://doi.org/10.1021/es200146g.

(41) Kim, D.; Archer, L. A. Nanoscale Organic-Inorganic Hybrid Lubricants. *Langmuir* **2011**, *27* (6), 3083–3094. https://doi.org/10.1021/la104937t.

(42) Lin, K. Y. A.; Yang, H.; Lee, W. Der; Tsao, K. Y. A Magnetic Fluid Based on Covalent-Bonded Nanoparticle Organic Hybrid Materials (NOHMs) and Its Decolorization Application in Water. *J. Mol. Liq.* **2015**, *204*, 50–59. https://doi.org/10.1016/J.MOLLIQ.2015.01.020.

(43) Park, Y.; Petit, C.; Han, P.; Alissa Park, A. H. Effect of Canopy Structures and Their Steric Interactions on CO2 Sorption Behavior of Liquid-like Nanoparticle Organic Hybrid Materials. *RSC Adv.* **2014**, *4* (17), 8723–8726. https://doi.org/10.1039/C3RA46801A.

(44) Fernandes, N. J.; Akbarzadeh, J.; Peterlik, H.; Giannelis, E. P. Synthesis and Properties of Highly Dispersed Ionic Silica-Poly(Ethylene Oxide) Nanohybrids. *ACS Nano* **2013**, *7* (2), 1265–1271. https://doi.org/10.1021/NN304735R.

(45) Yu, Z.; Yang, F.; Dai, S.; Qiao, R. Structure and Dynamics of Polymeric Canopies in Nanoscale Ionic Materials: An Electrical Double Layer Perspective. *Sci. Reports 2018 81* **2018**, *8* (1), 1–11. https://doi.org/10.1038/s41598-018-23493-1.

(46) Mcdonald, S.; Wood, J. A.; Fitzgerald, P. A.; Craig, V. S. J.; Warr, G. G.; Atkin, R. Interfacial and Bulk Nanostructure of Liquid Polymer Nanocomposites. **2015**. https://doi.org/10.1021/acs.langmuir.5b00255.

(47) Kemper, T. W.; Larsen, R. E.; Gennett, T. Relationship between Molecular Structure and Electron Transfer in a Polymeric Nitroxyl-Radical Energy Storage Material. *J. Phys. Chem. C* **2014**, *118* (31), 17213–17220. https://doi.org/10.1021/jp501628z.

(48) Oyaizu, K.; Nishide, H. Radical Polymers for Organic Electronic Devices: A Radical Departure from Conjugated Polymers? *Adv. Mater.* **2009**, *21* (22), 2339–2344. https://doi.org/10.1002/ADMA.200803554.

(49) Nakahara, K.; Oyaizu, K.; Nishide, H. Electrolyte Anion-Assisted Charge Transportation

in Poly(Oxoammonium Cation/Nitroxyl Radical) Redox Gels. *J. Mater. Chem.* **2012**, *22* (27), 13669–13673. https://doi.org/10.1039/C2JM31907A.

(50) Bobela, D. C.; Hughes, B. K.; Braunecker, W. A.; Kemper, T. W.; Larsen, R. E.; Gennett, T. Close Packing of Nitroxide Radicals in Stable Organic Radical Polymeric Materials. *J. Phys. Chem. Lett* **2015**, *6*, 1414–1419. https://doi.org/10.1021/acs.jpclett.5b00259.

(51) Martin, H. J.; Hughes, B. K.; Braunecker, W. A.; Gennett, T.; Dadmun, M. D. The Impact of Radical Loading and Oxidation on the Conformation of Organic Radical Polymers by Small Angle Neutron Scattering. *J. Mater. Chem. A* **2018**, *6* (32), 15659–15667. https://doi.org/10.1039/c8ta04583f.

(52) Hammouda, B. Probing Nanoscale Structures- The SANS Toolbox; 2008.

(53) Roe, R.-J. *Methods of Neutron and X-Ray Scattering in Polymer Science*; 2000.

(54) Shull, C. G.; Wollan, E. O. X-Ray, Electron, and Neutron Diffraction. *Science (80-.).* **1948**, *108* (2795), 69–75. https://doi.org/10.1126/SCIENCE.108.2795.69.

(55) Bragg, W. H. and W. L. *The Crystalline State*; The Macmillan company, 1933.

(56) Wei, Y.; Hore, M. J. A. Characterizing Polymer Structure with Small-Angle Neutron Scattering: A Tutorial. *J. Appl. Phys.* **2021**, *129* (17), 171101. https://doi.org/10.1063/5.0045841.

(57) Xie, S.; Zhang, B.; Mao, Y.; He, L.; Hong, K.; Bates, F. S.; Lodge, T. P. Influence of Added Salt on Chain Conformations in Poly(Ethylene Oxide) Melts: SANS Analysis with Complications. *Macromolecules* **2020**, *53* (16), 7141–7149. https://doi.org/10.1021/ACS.MACROMOL.0C01194.

(58) Griffin, L. R.; Browning, K. L.; Clarke, S. M.; Smith, A. M.; Perkin, S.; Skoda, M. W. A.; Norman, S. E. Direct Measurements of Ionic Liquid Layering at a Single Mica–Liquid Interface and in Nano-Films between Two Mica–Liquid Interfaces. *Phys. Chem. Chem. Phys.* **2017**, *19* (1), 297–304. https://doi.org/10.1039/c6cp05757h.

(59) Hayes, D. G.; Gomez Del Rio, J. A.; Ye, R.; Urban, V. S.; Pingali, S. V.; O'neill, H. M. Effect of Protein Incorporation on the Nanostructure of the Bicontinuous Microemulsion Phase of Winsor-III Systems: A Small-Angle Neutron Scattering Study. *Langmuir* **2015**, *31*, 2023. https://doi.org/10.1021/la504606x.

(60) Cabry, C. P.; D'Andrea, L.; Shimizu, K.; Grillo, I.; Li, P.; Rogers, S.; Bruce, D. W.; Canongia Lopes, J. N.; Slattery, J. M. Exploring the Bulk-Phase Structure of Ionic Liquid Mixtures Using Small-Angle Neutron Scattering. *Faraday Discuss.* **2017**, *206* (0), 265–289. https://doi.org/10.1039/C7FD00167C.

(61) Laver, M. Small-Angle Scattering of Nanostructures and Nanomaterials. *Encycl. Nanotechnol.* **2012**, 2437–2450. https://doi.org/10.1007/978-90-481-9751-4_118.

(62) Sears, V. F. Neutron Scattering Lengths and Cross Sections. *Neutron News* **2006**, *3* (3), 26–37. https://doi.org/10.1080/10448639208218770.

(63) Fournet, A. G. and G. *Small-Angle Scattering of X-Rays*; John Wiley & Sons, Inc, New York, 1955.

(64) Redfern, S. Elementary Scattering Theory For X-Ray and Neutron Users, by D.S. Sivia. *http://dx.doi.org/10.1080/00107514.2011.582162* **2011**, *52* (5), 498–498. https://doi.org/10.1080/00107514.2011.582162.

(65) Cousin, F.; Fadda, G. An Introduction to Neutron Reflectometry. *EPJ Web Conf.* **2020**, *236*, 04001. https://doi.org/10.1051/EPJCONF/202023604001.

(66) Nelson, A. Co-Refinement of Multiple-Contrast Neutron/X-Ray Reflectivity Data Using MOTOFIT. *J. Appl. Crystallogr.* **2006**, *39* (2), 273–276. https://doi.org/10.1107/S0021889806005073.

(67) Nguyen, T.; Savinell, R. F. Flow Batteries. *Electrochem. Soc. Interface* **2010**, *19* (3), 54–56. https://doi.org/10.1149/2.F06103if.

(68) Wei, X.; Pan, W.; Duan, W.; Hollas, A.; Yang, Z.; Li, B.; Nie, Z.; Liu, J.; Reed, D.; Wang, W.; Sprenkle, V. Materials and Systems for Organic Redox Flow Batteries: Status and Challenges. *ACS Energy Letters*. 2017, pp 2187–2204. https://doi.org/10.1021/acsenergylett.7b00650.

(69) Winsberg, J.; Hagemann, T.; Janoschka, T.; Hager, M. D.; Schubert, U. S. Redox-Flow Batteries: From Metals to Organic Redox-Active Materials. *Angew. Chemie - Int. Ed.* **2017**, *56* (3), 686–711. https://doi.org/10.1002/anie.201604925.

(70) Ding, Y.; Zhang, C.; Zhang, L.; Zhou, Y.; Yu, G. Molecular Engineering of Organic Electroactive Materials for Redox Flow Batteries. *Chem. Soc. Rev.* **2018**, *47* (1), 69–103. https://doi.org/10.1039/c7cs00569e.

(71) Gong, K.; Fang, Q.; Gu, S.; Li, S. F. Y.; Yan, Y. Nonaqueous Redox-Flow Batteries: Organic Solvents, Supporting Electrolytes, and Redox Pairs. *Energy Environ. Sci.* **2015**, *8* (12), 3515–3530. https://doi.org/10.1039/c5ee02341f.

(72) Leung, P.; Shah, A. A.; Sanz, L.; Flox, C.; Morante, J. R.; Xu, Q.; Mohamed, M. R.; Ponce de León, C.; Walsh, F. C. Recent Developments in Organic Redox Flow Batteries: A Critical Review. *J. Power Sources* **2017**, *360*, 243–283. https://doi.org/10.1016/j.jpowsour.2017.05.057.

(73) Su, L.; Darling, R. M.; Gallagher, K. G.; Xie, W.; Thelen, J. L.; Badel, A. F.; Barton, J. L.; Cheng, K. J.; Balsara, N. P.; Moore, J. S.; Brushett, F. R. An Investigation of the Ionic Conductivity and Species Crossover of Lithiated Nafion 117 in Nonaqueous Electrolytes. *J. Electrochem. Soc.* **2016**, *163* (1), A5253–A5262. https://doi.org/10.1149/2.0321601jes.

(74) Amanchukwu, C. V. The Electrolyte Frontier: A Manifesto. *Joule* **2020**, *4* (2), 281–285.

https://doi.org/10.1016/j.joule.2019.12.009.

(75) Cantillo, N.; Bruce, M.; Hamilton, S.; Feric, T.; Park, A.-H. A.; Zawodzinski, T. Electrochemical Behavior of Copper Ion Complexed with Nanoparticle Organic Hybrid Materials. *J. Electrochem. Soc.* **2020**, *167* (11), 116508. https://doi.org/10.1149/1945-7111/aba158.

(76) Chang, L.; Bard, A. J. Electrochemical Characterization of Bromine Reduction to Tribromide in Individual Nitrobenzene-in-Water Emulsion Droplets. *J. Electrochem. Soc.* **2020**, *167* (6), 066505. https://doi.org/10.1149/1945-7111/ab80ab.

(77) Shen, D.; Steinberg, K.; Akolkar, R. Avoiding Pitfalls in the Determination of Reliable Electrochemical Kinetics Parameters for the Cu 2+ → Cu 1+ Reduction Reaction in Deep Eutectic Solvents . *J. Electrochem. Soc.* **2018**, *165* (14), E808–E815. https://doi.org/10.1149/2.1011814jes.

(78) Gurkan, B.; Squire, H.; Pentzer, E. Metal-Free Deep Eutectic Solvents: Preparation, Physical Properties, and Significance. *Journal of Physical Chemistry Letters*. 2019, pp 7956–7964. https://doi.org/10.1021/acs.jpclett.9b01980.

(79) Petit, C.; Park, Y.; Lin, K. Y. A.; Park, A. H. A. Spectroscopic Investigation of the Canopy Configurations in Nanoparticle Organic Hybrid Materials of Various Grafting Densities during CO 2 Capture. *J. Phys. Chem. C* **2012**, *116* (1), 516–525. https://doi.org/10.1021/JP210391C.

(80) Park, Y.; Shin, D.; Jang, Y. N.; Park, A.-H. A. CO2 Capture Capacity and Swelling Measurements of Liquid-like Nanoparticle Organic Hybrid Materials via Attenuated Total Reflectance Fourier Transform Infrared Spectroscopy. *J. Chem. Eng. Data* **2012**, *57* (1), 40–45. https://doi.org/10.1021/je200623b.

(81) Park, Y.; Lin, K.-Y. A.; Park, A.-H. A.; Petit, C. Recent Advances in Anhydrous Solvents for CO2 Capture: Ionic Liquids, Switchable Solvents, and Nanoparticle Organic Hybrid Materials. *Front. Energy Res.* **2015**, *3* (October), 1–14. https://doi.org/10.3389/fenrg.2015.00042.

(82) Lin, K.-Y. A.; Petit, C.; Park, A.-H. A. Effect of SO2 on CO2 Capture Using Liquid-like Nanoparticle Organic Hybrid Materials. *Energy & Fuels* **2013**, *27* (8), 4167–4174. https://doi.org/10.1021/ef400374q.

(83) Agrawal, A.; Choudhury, S.; Archer, L. A. A Highly Conductive, Non-Flammable Polymer–Nanoparticle Hybrid Electrolyte. *RSC Adv.* **2015**, *5* (27), 20800–20809. https://doi.org/10.1039/C5RA01031D.

(84) Choudhury, S.; Agrawal, A.; Wei, S.; Jeng, E.; Archer, L. A. Hybrid Hairy Nanoparticle Electrolytes Stabilizing Lithium Metal Batteries. *Chem. Mater.* **2016**, *28* (7), 2147–2157. https://doi.org/10.1021/acs.chemmater.6b00029.

(85) Tikekar, M. D.; Archer, L. A.; Koch, D. L. Stability Analysis of Electrodeposition across a

Structured Electrolyte with Immobilized Anions. *J. Electrochem. Soc.* **2014**, *161* (6), A847–A855. https://doi.org/10.1149/2.085405jes.

(86) Park, Y.; Petit, C.; Han, P.; Alissa Park, A.-H. H. Effect of Canopy Structures and Their Steric Interactions on CO2 Sorption Behavior of Liquid-like Nanoparticle Organic Hybrid Materials. *RSC Adv.* **2014**, *4* (17), 8723–8726. https://doi.org/10.1039/c3ra46801a.

(87) Park, Y.; Decatur, J.; Lin, K.-Y. A.; Park, A.-H. A. Investigation of CO2 Capture Mechanisms of Liquid-like Nanoparticle Organic Hybrid Materials via Structural Characterization. *Phys. Chem. Chem. Phys.* **2011**, *13* (40), 18115. https://doi.org/10.1039/c1cp22631b.

(88) Wei, Y.; Xu, Y.; Faraone, A.; Hore, M. J. A. Local Structure and Relaxation Dynamics in the Brush of Polymer-Grafted Silica Nanoparticles. **2020**, *26*, 20. https://doi.org/10.1021/acsmacrolett.8b00223.

(89) Chevigny, C. E.; Dalmas, F.; Cola, E. Di; Gigmes, D.; Bertin, D.; Bou, F.-O.; Jestin, J. Polymer-Grafted-Nanoparticles Nanocomposites: Dispersion, Grafted Chain Conformation, and Rheological Behavior. *Macromolecules* **2011**, *44*, 122–133. https://doi.org/10.1021/ma101332s.

(90) Jouault, N.; Crawford, M. K.; Chi, C.; Smalley, R. J.; Wood, B.; Jestin, J.; Melnichenko, Y. B.; He, L.; Guise, W. E.; Kumar, S. K. Polymer Chain Behavior in Polymer Nanocomposites with Attractive Interactions. *ACS Macro Lett.* **2016**, *5* (4), 523–527. https://doi.org/10.1021/acsmacrolett.6b00164.

(91) Robbes, A. S.; Cousin, F.; Meneau, F.; Dalmas, F.; Boué, F.; Jestin, J. Nanocomposite Materials with Controlled Anisotropic Reinforcement Triggered by Magnetic Self-Assembly. *Macromolecules* **2011**, *44* (22), 8858–8865. https://doi.org/10.1021/ma201096u.

(92) Buenning, E.; Jestin, J.; Huang, Y.; Benicewicz, B. C.; Durning, C. J.; Kumar, S. K. Location of Imbibed Solvent in Polymer-Grafted Nanoparticle Membranes. **2020**, *26*, 42. https://doi.org/10.1021/acsmacrolett.8b00472.

(93) Jespersen, M. L.; Mirau, P. A.; Von Meerwall, E.; Vaia, R. A.; Rodriguez, R.; Giannelis, E. P. Canopy Dynamics in Nanoscale Ionic Materials. **2010**. https://doi.org/10.1021/nn100112h.

(94) Choi, S.; Moon, S.; Park, Y. Spectroscopic Investigation of Entropic Canopy-Canopy Interactions of Nanoparticle Organic Hybrid Materials. *Langmuir* **2020**, *36* (32), 9626–9633. https://doi.org/10.1021/ACS.LANGMUIR.0C01784.

(95) SANS and USANS Data Reduction and Analysis Software | NIST https://www.nist.gov/ncnr/data-reduction-analysis/sans-software (accessed Oct 26, 2020).

(96) SasView - Small Angle Scattering Analysis https://www.sasview.org/ (accessed Oct 26, 2020).

(97) Sharma, R. V.; Sharma, K. C. The Structure Factor and the Transport Properties of Dense Fluids Having Molecules with Square Well Potential, a Possible Generalization. *Phys. A Stat. Mech. its Appl.* **1977**, *89* (1), 213–218. https://doi.org/10.1016/0378-4371(77)90151-0.

(98) Menon, S. V. G.; Manohar, C.; Srinivasa Rao, K. A New Interpretation of the Sticky Hard Sphere Model. *J. Chem. Phys.* **1991**, *95* (12), 9186–9190. https://doi.org/10.1063/1.461199.

(99) Hammouda, B. SANS from Homogeneous Polymer Mixtures: A Unified Overview. *Adv. Polym. Sci.* **1993**, *106*, 86–133. https://doi.org/10.1007/BFB0025862/COVER.

(100) Lange, F.; Judeinstein, P.; Franz, C.; Hartmann-Azanza, B.; Ok, S.; Steinhart, M.; Saalwächter, K. Large-Scale Diffusion of Entangled Polymers along Nanochannels. *ACS Macro Lett.* **2015**, *4* (5), 561–565. https://doi.org/10.1021/acsmacrolett.5b00213.

(101) Martin, H. J.; Tyler White, B.; Yuan, G.; Saito, T.; D. Dadmun, M. Relative Size of the Polymer and Nanoparticle Controls Polymer Diffusion in All-Polymer Nanocomposites. *Macromolecules* **2019**, *52* (7), 2843–2852. https://doi.org/10.1021/acs.macromol.8b02596.

(102) Gam, S.; S. Meth, J.; G. Zane, S.; Chi, C.; A. Wood, B.; E. Seitz, M.; I. Winey, K.; Clarke, N.; J. Composto, R. Macromolecular Diffusion in a Crowded Polymer Nanocomposite. *Macromolecules* **2011**, *44* (9), 3494–3501. https://doi.org/10.1021/ma102463q.

(103) Jespersen, M. L.; Mirau, P. A.; von Meerwall, E. D.; Koerner, H.; Vaia, R. A.; Fernandes, N. J.; Giannelis, E. P. Hierarchical Canopy Dynamics of Electrolyte-Doped Nanoscale Ionic Materials. **2013**, *46*, 31. https://doi.org/10.1021/ma402002a.

(104) Yang, R.; Fan, W.; Zheng, Y.; Wang, T.; Wang, Y.; Shi, T.; Yao, D.; Chen, L.; Zhang, A. Effects of the Core of Liquid-like SiO2 Nanoparticle Organic Hybrid Materials on CO2 Capture. *J. Mater. Sci.* **2018**, *53* (7), 5172–5182. https://doi.org/10.1007/s10853-017-1772-4.

(105) Dunn, B.; Kamath, H.; Tarascon, J. M. Electrical Energy Storage for the Grid: A Battery of Choices. *Science* **2011**, *334* (6058), 928–935. https://doi.org/10.1126/SCIENCE.1212741.

(106) Szetela, B.; Majewska, A.; Jamroz, P.; Djalilov, B.; Salahodjaev, R. Renewable Energy and CO2 Emissions in Top Natural Resource Rents Depending Countries: The Role of Governance. *Front. Energy Res.* **2022**, *10*, 242. https://doi.org/10.3389/FENRG.2022.872941.

(107) Yang, Z.; Zhang, J.; Kintner-Meyer, M. C. W.; Lu, X.; Choi, D.; Lemmon, J. P.; Liu, J. Electrochemical Energy Storage for Green Grid. *Chem. Rev.* **2011**, *111* (5), 3577–3613. https://doi.org/10.1021/CR100290V.

(108) Chu, S.; Cui, Y.; Liu, N. The Path towards Sustainable Energy. *Nat. Mater.* **2016**, *16* (1), 16–22. https://doi.org/10.1038/NMAT4834.

(109) Soloveichik, G. L. Flow Batteries: Current Status and Trends. *Chem. Rev.* **2015**, *115* (20),

11533–11558. https://doi.org/10.1021/CR500720T.

(110) Chakrabarti, M. H.; Mjalli, F. S.; Alnashef, I. M.; Hashim, M. A.; Hussain, M. A.; Bahadori, L.; Low, C. T. J. Prospects of Applying Ionic Liquids and Deep Eutectic Solvents for Renewable Energy Storage by Means of Redox Flow Batteries. *Renew. Sustain. Energy Rev.* **2014**, *30*, 254–270. https://doi.org/10.1016/J.RSER.2013.10.004.

(111) Wei, X.; Hollas, A.; Yang, Z.; Huang, J.; Murugesan, V.; Walter, E.; Li, B.; Nie, Z.; Reed, D.; Zhang, Z.; Wang, W.; Sprenkle, V. Materials Development for Aqueous Organic Redox Flow Batteries. *ECS Meet. Abstr.* **2018**, *MA2018-01* (2), 239. https://doi.org/10.1149/MA2018-01/2/239.

(112) Nguyen, T.; Savinell, R. F. Flow Batteries. *Electrochem. Soc. Interface* **2010**, *19* (3), 54–56. https://doi.org/10.1149/2.F06103if.

(113) Lu, Y.; Chen, J. Prospects of Organic Electrode Materials for Practical Lithium Batteries. *Nat. Rev. Chem. 2020 43* **2020**, *4* (3), 127–142. https://doi.org/10.1038/s41570-020-0160-9.

(114) Huang, Z.; Kay, C. W. M.; Kuttich, B.; Rauber, D.; Kraus, T.; Li, H.; Kim, S.; Chen, R. An "Interaction-Mediating" Strategy towards Enhanced Solubility and Redox Properties of Organics for Aqueous Flow Batteries. *Nano Energy* **2020**, *69*, 104464. https://doi.org/10.1016/J.NANOEN.2020.104464.

(115) Ejigu, A.; Greatorex-Davies, P. A.; Walsh, D. A. Room Temperature Ionic Liquid Electrolytes for Redox Flow Batteries. *Electrochem. commun.* **2015**, *54*, 55–59. https://doi.org/10.1016/J.ELECOM.2015.01.016.

(116) Imel, A. E.; Barth, B.; Hayes, D. G.; Dadmun, M.; Zawodzinski, T. Microemulsions as Emerging Electrolytes: The Correlation of Structure to Electrochemical Response. *ACS Appl. Mater. Interfaces* **2022**, *14* (17), 20179–20189. https://doi.org/10.1021/acsami.2c00181.

(117) Barth, B. A.; Imel, A.; Nelms, K. M. K.; Goenaga, G. A.; Zawodzinski, T. Microemulsions: Breakthrough Electrolytes for Redox Flow Batteries. *Front. Chem.* **2022**, *10*. https://doi.org/10.3389/FCHEM.2022.831200.

(118) Peng, J.; Xiao, Y.; Imel, A.; Barth, B. A.; Cantillo, N. M.; Nelms, K. M. K.; Zawodzinski, T. A. Electrolyte Effects on the Electrochemical Performance of Microemulsions. *Electrochim. Acta* **2021**, *393*, 139048. https://doi.org/10.1016/J.ELECTACTA.2021.139048.

(119) Peng, J.; Cantillo, N. M.; Nelms, K. M. K.; Roberts, L. S.; Goenaga, G.; Imel, A.; Barth, B. A.; Dadmun, M.; Heroux, L.; Hayes, D. G.; Zawodzinski, T. Electron Transfer in Microemulsion-Based Electrolytes. *ACS Appl. Mater. Interfaces* **2020**, *12* (36), 40213–40219. https://doi.org/10.1021/ACSAMI.0C07028.

(120) Wang, Y.; Niu, Z.; Zheng, Q.; Zhang, C.; Ye, J.; Dai, G.; Zhao, Y.; Zhang, X. Zn-Based

Eutectic Mixture as Anolyte for Hybrid Redox Flow Batteries OPEN. https://doi.org/10.1038/s41598-018-24059-x.

(121) Xu, Q.; Qin, L. Y.; Ji, Y. N.; Leung, P. K.; Su, H. N.; Qiao, F.; Yang, W. W.; Shah, A. A.; Li, H. M. A Deep Eutectic Solvent (DES) Electrolyte-Based Vanadium-Iron Redox Flow Battery Enabling Higher Specific Capacity and Improved Thermal Stability. *Electrochim. Acta* **2019**, *293*, 426–431. https://doi.org/10.1016/J.ELECTACTA.2018.10.063.

(122) Kawase, K.; Abe, J.; Tenjimbayashi, M.; Kobayashi, Y.; Takahashi, K.; Shiratori, S. Novel Deep-Eutectic-Solvent-Infused Carbon Nanofiber Networks as High Power Density Green Battery Cathodes. *ACS Appl. Mater. Interfaces* **2018**, *10* (18), 15742–15750. https://doi.org/10.1021/ACSAMI.8B03099.

(123) Petit, C.; Lin, K. Y. A.; Park, A. H. A. Design and Characterization of Liquidlike POSS-Based Hybrid Nanomaterials Synthesized via Ionic Bonding and Their Interactions with CO2. *Langmuir* **2013**, *29* (39), 12234–12242. https://doi.org/10.1021/LA4007923.

(124) Rim, G.; Feric, T. G.; Moore, T.; Park, A. H. A. Solvent Impregnated Polymers Loaded with Liquid-Like Nanoparticle Organic Hybrid Materials for Enhanced Kinetics of Direct Air Capture and Point Source CO2 Capture. *Adv. Funct. Mater.* **2021**, *31* (21), 2010047. https://doi.org/10.1002/ADFM.202010047.

(125) Agrawal, A.; Choudhury, S.; Archer, L. A. A Highly Conductive, Non-Flammable Polymer–Nanoparticle Hybrid Electrolyte. *RSC Adv.* **2015**, *5* (27), 20800–20809. https://doi.org/10.1039/C5RA01031D.

(126) Tikekar, M. D.; Archer, L. A.; Koch, D. L. Stability Analysis of Electrodeposition across a Structured Electrolyte with Immobilized Anions. *J. Electrochem. Soc.* **2014**, *161* (6), A847–A855. https://doi.org/10.1149/2.085405JES.

(127) Park, Y.; Shin, D.; Jang, Y. N.; Park, A. H. A. CO2 Capture Capacity and Swelling Measurements of Liquid-like Nanoparticle Organic Hybrid Materials via Attenuated Total Reflectance Fourier Transform Infrared Spectroscopy. *J. Chem. Eng. Data* **2011**, *57* (1), 40–45. https://doi.org/10.1021/JE200623B.

(128) Park, Y.; Decatur, J.; Lin, K. Y. A.; Park, A. H. A. Investigation of CO2 Capture Mechanisms of Liquid-like Nanoparticle Organic Hybrid Materials via Structural Characterization. *Phys. Chem. Chem. Phys.* **2011**, *13* (40), 18115–18122. https://doi.org/10.1039/C1CP22631B.

(129) Feric, T. G.; Hamilton, S. T.; Ko, B. H.; Lee, G. A.; Verma, S.; Jiao, F.; Park, A. H. A. Highly Tunable Syngas Product Ratios Enabled by Novel Nanoscale Hybrid Electrolytes Designed for Combined CO2 Capture and Electrochemical Conversion. *Adv. Funct. Mater.* **2023**, 2210017. https://doi.org/10.1002/ADFM.202210017.

(130) Feric, T. G.; Hamilton, S. T.; Cantillo, N. M.; Imel, A. E.; Zawodzinski, T. A.; Park, A. H. A. Dynamic Mixing Behaviors of Ionically Tethered Polymer Canopy of Nanoscale Hybrid Materials in Fluids of Varying Physical and Chemical Properties. *J. Phys. Chem. B* **2021**,

125 (32), 9223–9234. https://doi.org/10.1021/ACS.JPCB.1C00935.

(131) Hamilton, S. T.; Feric, T. G.; Bhattacharyya, S.; Cantillo, N. M.; Greenbaum, S. G.; Zawodzinski, T. A.; Park, A. A. Nanoscale Hybrid Electrolytes with Viscosity Controlled Using Ionic Stimulus for Electrochemical Energy Conversion and Storage. *JACS Au* **2022**. https://doi.org/10.1021/jacsau.1c00410.

(132) Zhang, Y.; Poe, D.; Heroux, L.; Squire, H.; Doherty, B. W.; Long, Z.; Dadmun, M.; Gurkan, B.; Tuckerman, M. E.; Maginn, E. J. Liquid Structure and Transport Properties of the Deep Eutectic Solvent Ethaline. *J. Phys. Chem. B* **2020**, *124* (25), 5251–5264. https://doi.org/10.1021/ACS.JPCB.0C04058.

(133) Klein, J. M.; Squire, H.; Dean, W.; Gurkan, B. E. From Salt in Solution to Solely Ions: Solvation of Methyl Viologen in Deep Eutectic Solvents and Ionic Liquids. **2020**. https://doi.org/10.1021/acs.jpcb.0c03296.

(134) Liu, S.; Tyagi, M.; Akcora, P. Polymer-Coupled Local Dynamics Enhances Conductivity of Ionic Liquids. *Macromolecules* **2020**, *53* (15), 6538–6546. https://doi.org/10.1021/ACS.MACROMOL.0C01434.

(135) Jayakody, N. K.; Fraenza, C. C.; Greenbaum, S. G.; Ashby, D.; Dunn, B. S. NMR Relaxometry and Diffusometry Analysis of Dynamics in Ionic Liquids and Ionogels for Use in Lithium-Ion Batteries. *J. Phys. Chem. B* **2020**, *124* (31), 6843–6856. https://doi.org/10.1021/acs.jpcb.0c02755.

(136) Haque, M. A.; Feric, T.; Hamilton, S.; Park, A.-H.; Dadmun, M. Structure and Dispersion of Free and Grafted Polymer in Nanoparticle Organic Hybrid Materials-Based Solutions by Small-Angle Neutron Scattering. *J. Phys. Chem. C 125* (9), 5327–5334. https://doi.org/10.1021/acs.jpcc.0c10790.

(137) Feric, T. G.; Hamilton, S. T.; Haque, M. A.; Jeddi, J.; Sangoro, J.; Dadmun, M. D.; Park, A. H. A. Impacts of Bond Type and Grafting Density on the Thermal, Structural, and Transport Behaviors of Nanoparticle Organic Hybrid Materials-Based Electrolytes. *Adv. Funct. Mater.* **2022**, *32* (36). https://doi.org/10.1002/adfm.202203947.

(138) SasView - Small Angle Scattering Analysis https://www.sasview.org/ (accessed Dec 8, 2021).

(139) Beaucage, G. Small-Angle Scattering from Polymeric Mass Fractals of Arbitrary Mass-Fractal Dimension. *J. Appl. Crystallogr.* **1996**, *29* (2), 134–146. https://doi.org/10.1107/S0021889895011605.

(140) Lodge, T. P.; Hiemenz, P. C. Polymer Chemistry. **2020**. https://doi.org/10.1201/9780429190810.

(141) Mildner, D. F. R.; Hall, P. L. Small-Angle Scattering from Porous Solids with Fractal Geometry. *J. Phys. D. Appl. Phys.* **1986**, *19* (8), 1535. https://doi.org/10.1088/0022-3727/19/8/021.

(142) Tomchuk, O. V.; Avdeev, M. V.; Bulavin, L. A. Modeling Fractal Aggregates of Polydisperse Particles with Tunable Dimension. *Colloids Surfaces A Physicochem. Eng. Asp.* **2020**, *605*, 125331. https://doi.org/10.1016/J.COLSURFA.2020.125331.

(143) Fernandes, N. J.; Koerner, H.; Giannelis, E. P.; Vaia, R. A. Hairy Nanoparticle Assemblies as One-Component Functional Polymer Nanocomposites: Opportunities and Challenges. *MRS Commun.* **2013**, *3* (1), 13–29. https://doi.org/10.1557/MRC.2013.9.

(144) Mahbubul, I. M.; Saidur, R.; Amalina, M. A. Latest Developments on the Viscosity of Nanofluids. *Int. J. Heat Mass Transf.* **2012**, *55* (4), 874–885. https://doi.org/10.1016/J.IJHEATMASSTRANSFER.2011.10.021.

(145) Olayiwola, S. O.; Dejam, M. Experimental Study on the Viscosity Behavior of Silica Nanofluids with Different Ions of Electrolytes. *Ind. Eng. Chem. Res.* **2020**, *59* (8), 3575–3583. https://doi.org/10.1021/ACS.IECR.9B06275.

(146) Sheppard, S. E.; Vanselow, W.; Happ, G. P.; Kameyama, N.; Fukumoto, T.; ; • Von Hippe, !; Eggert, A.; Biltz, J. Viscosity of Suspensions and the Einstein Equation. *Nat. 1940 1453686* **1940**, *145* (3686), 970–970. https://doi.org/10.1038/145970a0.

(147) Yan, W.; Wang, C.; Tian, J.; Zhu, G.; Ma, L.; Wang, Y.; Chen, R.; Hu, Y.; Wang, L.; Chen, T.; Ma, J.; Jin, Z. All-Polymer Particulate Slurry Batteries. *Nat. Commun. 2019 101* **2019**, *10* (1), 1–11. https://doi.org/10.1038/s41467-019-10607-0.

(148) Janoschka, T.; Martin, N.; Martin, U.; Friebe, C.; Morgenstern, S.; Hiller, H.; Hager, M. D.; Schubert, U. S. An Aqueous, Polymer-Based Redox-Flow Battery Using Non-Corrosive, Safe, and Low-Cost Materials. https://doi.org/10.1038/nature15746.

(149) Luo, J.; Hu, B.; Hu, M.; Zhao, Y.; Liu, T. L. Status and Prospects of Organic Redox Flow Batteries toward Sustainable Energy Storage. *ACS Energy Lett.* **2019**, *4* (9), 2220–2240. https://doi.org/10.1021/ACSENERGYLETT.9B01332.

(150) Li, Z.; Lu, Y. C. Material Design of Aqueous Redox Flow Batteries: Fundamental Challenges and Mitigation Strategies. *Adv. Mater.* **2020**, *32* (47), 2002132. https://doi.org/10.1002/ADMA.202002132.

(151) Liu, Y.; Chen, Q.; Sun, P.; Li, Y.; Yang, Z.; Xu, T. Organic Electrolytes for Aqueous Organic Flow Batteries. *Mater. Today Energy* **2021**, *20*, 100634. https://doi.org/10.1016/J.MTENER.2020.100634.

(152) Wang, W.; Xu, W.; Cosimbescu, L.; Choi, D.; Li, L.; Yang, Z. Anthraquinone with Tailored Structure for a Nonaqueous Metal–Organic Redox Flow Battery. *Chem. Commun.* **2012**, *48* (53), 6669–6671. https://doi.org/10.1039/C2CC32466K.

(153) Wang, X.; Chai, J.; Devi, N.; Lashgari, A.; Chaturvedi, A.; Jiang, J. "Jimmy." Two-Electron-Active Tetracyanoethylene for Nonaqueous Redox Flow Batteries. *J. Mater. Chem. A* **2021**, *9* (24), 13867–13873. https://doi.org/10.1039/D1TA01365C.

(154) Zhang, Y.; Chen, Z.; Qiu, H.; Yang, W.; Zhao, Z.; Zhao, J.; Cui, G. Pursuit of Reversible Zn Electrochemistry: A Time-Honored Challenge towards Low-Cost and Green Energy Storage. *NPG Asia Mater. 2020 121* **2020**, *12* (1), 1–24. https://doi.org/10.1038/s41427-019-0167-1.

(155) Zhao, Q.-Y.; Yin, G.-Y.; Liu, Y.-F.; Tang, R.-R.; Wu, X.-W.; Zeng, X.-X.; Xian-Xiang Zeng, C. Recent Advances in Material Chemistry for Zinc Enabled Redox Flow Batteries. *Carbon Neutralization* **2023**, *2* (1), 90–114. https://doi.org/10.1002/CNL2.43.

(156) Ma, L.; Pollard, T. P.; Zhang, Y.; Schroeder, M. A.; Ding, M. S.; Cresce, A. V.; Sun, R.; Baker, D. R.; Helms, B. A.; Maginn, E. J.; Wang, C.; Borodin, O.; Xu, K. Functionalized Phosphonium Cations Enable Zinc Metal Reversibility in Aqueous Electrolytes. *Angew. Chemie - Int. Ed.* **2021**, *60* (22), 12438–12445. https://doi.org/10.1002/anie.202017020.

(157) Hamilton, S. T.; Feric, T. G.; Gładysiak, A.; Cantillo, N. M.; Zawodzinski, T. A.; Park, A. H. A. Mechanistic Study of Controlled Zinc Electrodeposition Behaviors Facilitated by Nanoscale Electrolyte Additives at the Electrode Interface. *ACS Appl. Mater. Interfaces* **2021**. https://doi.org/10.1021/acsami.1c23781.

(158) Zhang, D.; Warren, A. J.; Li, G.; Cheng, Z.; Han, X.; Zhao, Q.; Liu, X.; Deng, Y.; Archer, L. A. Electrodeposition of Zinc in Aqueous Electrolytes Containing High Molecular Weight Polymers. https://doi.org/10.1021/acs.macromol.0c00037.

(159) X-Ray and Neuron Reflectivity: Principles and Applications. *X-ray Neuron Reflectivity Princ. Appl.* **1999**. https://doi.org/10.1007/3-540-48696-8.

(160) Sears, V. F. Special Feature Neutron Scattering Lengths and Cross Sectioirn.

(161) Griffin, L. R.; Browning, K. L.; Clarke, S. M.; Smith, A. M.; Perkin, S.; Skoda, M. W. A.; Norman, S. E. Direct Measurements of Ionic Liquid Layering at a Single Mica–Liquid Interface and in Nano-Films between Two Mica–Liquid Interfaces. *Phys. Chem. Chem. Phys.* **2016**, *19* (1), 297–304. https://doi.org/10.1039/C6CP05757H.

(162) Nishi, N.; Uchiyashiki, J.; Ikeda, Y.; Katakura, S.; Oda, T.; Hino, M.; Yamada, N. L. Potential-Dependent Structure of the Ionic Layer at the Electrode Interface of an Ionic Liquid Probed Using Neutron Reflectometry. *J. Phys. Chem. C* **2019**, *123* (14), 9223–9230. https://doi.org/10.1021/acs.jpcc.9b01151.

(163) Lauw, Y.; Horne, M. D.; Rodopoulos, T.; Lockett, V.; Akgun, B.; Hamilton, W. A.; Nelson, A. R. J. Structure of [C 4 Mpyr][NTf 2] Room-Temperature Ionic Liquid at Charged Gold Interfaces. **2012**, *28*, 7381. https://doi.org/10.1021/la3005757.

(164) Klein, J. M.; Wang, H.; Sacci, R. L.; Browning, J. F.; Gurkan, B. Smooth Modified Surfaces of Silicon for the Study of Ionic Liquid Interfaces by Neutron Reflectometry. *ACS Appl. Electron. Mater.* **2021**. https://doi.org/10.1021/acsaelm.1c01351.

(165) Al-Shatty, W.; Campana, M.; Alexander, S.; Barron, A. R. Interaction of Surface-Modified Alumina Nanoparticles and Surfactants at an Oil/Water Interface: A Neutron Reflectometry,

Scattering, and Enhanced Oil Recovery Study. *ACS Appl. Mater. Interfaces* **2022**, *14* (17), 19505–19514. https://doi.org/10.1021/ACSAMI.2C02228.

(166) Chung, E.; Yiacoumi, S.; Halbert, C.; Ankner, J.; Wang, W.; Kim, C.; Tsouris, C. Interaction of Silica Nanoparticles with a Flat Silica Surface through Neutron Reflectometry. *Environ. Sci. Technol.* **2012**, *46* (8), 4532–4538. https://doi.org/10.1021/es203992b.

(167) Vargas-Ruiz, S.; Soltwedel, O.; Micciulla, S.; Sreij, R.; Feoktystov, A.; Von Klitzing, R.; Hellweg, T.; Wellert, S. Sugar Surfactant Based Microemulsions at Solid Surfaces: Influence of the Oil Type and Surface Polarity. *Langmuir* **2016**, *32* (45), 11928–11938. https://doi.org/10.1021/ACS.LANGMUIR.6B03441.

(168) Browning, K. L.; Sacci, R. L.; Doucet, M.; Browning, J. F.; Kim, J. R.; Veith, G. M. The Study of the Binder Poly(Acrylic Acid) and Its Role in Concomitant Solid-Electrolyte Interphase Formation on Si Anodes. *ACS Appl. Mater. Interfaces* **2020**, *12* (8), 10018–10030. https://doi.org/10.1021/acsami.9b22382.

(169) Heroux, L. Structure Analysis of Soft Energy Materials Using Neutron Scattering. *Dr. Diss.* **2021**.

(170) Berton, P.; Kelley, S. P.; Bridges, N. J.; Klingshirn, M. A.; Huddleston, J. G.; Willauer, H. D.; Baldwin, J. W.; Moody, M. L.; Rogers, R. D. Water in Solutions of Chaotropic and Kosmotropic Salts: A Differential Scanning Calorimetry Investigation. *J. Chem. Eng. Data* **2019**, *64* (11), 4781–4792. https://doi.org/10.1021/acs.jced.9b00222.

(171) Collins, K. D.; Washabaugh, M. W. The Hofmeister Effect and the Behaviour of Water at Interfaces. *Q. Rev. Biophys.* **1985**, *18* (4), 323–422. https://doi.org/10.1017/S0033583500005369.

(172) Marcus, Y. Effect of Ions on the Structure of Water: Structure Making and Breaking. *Chem. Rev.* **2009**, *109* (3), 1346–1370. https://doi.org/10.1021/CR8003828/.

(173) Hughey, J. R.; Keen, J. M.; Miller, D. A.; Kolter, K.; Langley, N.; McGinity, J. W. The Use of Inorganic Salts to Improve the Dissolution Characteristics of Tablets Containing Soluplus®-Based Solid Dispersions. *Eur. J. Pharm. Sci.* **2013**, *48* (4–5), 758–766. https://doi.org/10.1016/J.EJPS.2013.01.004.

(174) Helms, B. A.; Seferos, D. S. Virtual Issue: Designing Polymers for Use in Electrochemical Energy Storage Devices. *Macromolecules*. American Chemical Society February 26, 2019, pp 1349–1353. https://doi.org/10.1021/acs.macromol.9b00035.

(175) Kim, J. K.; Cheruvally, G.; Choi, J. W.; Ahn, J. H.; Lee, S. H.; Choi, D. S.; Song, C. E. Effect of Radical Polymer Cathode Thickness on the Electrochemical Performance of Organic Radical Battery. *Solid State Ionics* **2007**, *178* (27–28), 1546–1551. https://doi.org/10.1016/J.SSI.2007.09.009.

(176) Li, W.; Lee, S.; Manthiram, A. High-Nickel NMA: A Cobalt-Free Alternative to NMC and

NCA Cathodes for Lithium-Ion Batteries. *Adv. Mater.* **2020**, *32* (33), 2002718. https://doi.org/10.1002/adma.202002718.

(177) Kang, D. H. P.; Chen, M.; Ogunseitan, O. A. Potential Environmental and Human Health Impacts of Rechargeable Lithium Batteries in Electronic Waste. *Environ. Sci. Technol.* **2013**, *47* (10), 5495–5503. https://doi.org/10.1021/es400614y.

(178) Yonekuta, Y.; Susuki, K.; Oyaizu, K.; Honda, K.; Nishide, H. Battery-Inspired, Nonvolatile, and Rewritable Memory Architecture: A Radical Polymer-Based Organic Device. *J. Am. Chem. Soc.* **2007**, *129* (46), 14128–14129. https://doi.org/10.1021/JA075553P/SUPPL_FILE/JA075553PSI20070725_101247.PDF.

(179) Tan, Y.; Casetti, N. C.; Boudouris, B. W.; Savoie, B. M. Molecular Design Features for Charge Transport in Nonconjugated Radical Polymers. *J. Am. Chem. Soc.* **2021**, *143* (31), 11994–12002. https://doi.org/10.1021/jacs.1c02571.

(180) Nakahara, K.; Oyaizu, K.; Nishide, H. Organic Radical Battery Approaching Practical Use. *Chemistry Letters*. The Chemical Society of Japan 公益社団法人 日本化学会 February 5, 2011, pp 222–227. https://doi.org/10.1246/cl.2011.222.

(181) Loo, W. S.; Mongcopa, K. I.; Gribble, D. A.; Faraone, A. A.; Balsara, N. P. Investigating the Effect of Added Salt on the Chain Dimensions of Poly(Ethylene Oxide) through Small-Angle Neutron Scattering. *Macromolecules* **2019**, *52* (22), 8724–8732. https://doi.org/10.1021/acs.macromol.9b01509.

(182) McCulloch, B.; Ho, V.; Hoarfrost, M.; Stanley, C.; Do, C.; Heller, W. T.; Segalman, R. A. Polymer Chain Shape of Poly(3-Alkylthiophenes) in Solution Using Small-Angle Neutron Scattering. *Macromolecules* **2013**, *46* (5), 1899–1907. https://doi.org/10.1021/ma302463d.

(183) Annis, B. K.; Kim, M. H.; Wignall, G. D.; Borodin, O.; Smith, G. D. Study of the Influence of LiI on the Chain Conformations of Poly(Ethylene Oxide) in the Melt by Small-Angle Neutron Scattering and Molecular Dynamics Simulations. *Macromolecules* **2000**, *33* (20), 7544–7548. https://doi.org/10.1021/ma000452w.

(184) Bugnon, L.; Morton, C. J. H.; Novak, P.; Vetter, J.; Nesvadba, P. Synthesis of Poly(4-Methacryloyloxy-TEMPO) via Group-Transfer Polymerization and Its Evaluation in Organic Radical Battery. *Chem. Mater.* **2007**, *19* (11), 2910–2914. https://doi.org/10.1021/cm063052h.

(185) Basma, N. S.; Headen, T. F.; Shaffer, M. S. P.; Skipper, N. T.; Howard, C. A. Local Structure and Polar Order in Liquid N-Methyl-2-Pyrrolidone (NMP). *J. Phys. Chem. B* **2018**, *122* (38), 8963–8971. https://doi.org/10.1021/acs.jpcb.8b08020.

(186) Easley, A. D.; Vukin, L. M.; Flouda, P.; Howard, D. L.; Pena, J. L.; Lutkenhaus, J. L. Nitroxide Radical Polymer−Solvent Interactions and Solubility Parameter Determination. **2020**. https://doi.org/10.1021/acs.macromol.0c01739.

(187) Bauer, W.; Nötzel, D. Rheological Properties and Stability of NMP Based Cathode Slurries

for Lithium Ion Batteries. *Ceram. Int.* **2014**, *40* (3), 4591–4598. https://doi.org/10.1016/J.CERAMINT.2013.08.137.

(188) Rostro, L.; Baradwaj, A. G.; Boudouris, B. W. Controlled Radical Polymerization and Quantification of Solid State Electrical Conductivities of Macromolecules Bearing Pendant Stable Radical Groups. *ACS Appl. Mater. Interfaces* **2013**, *5* (20), 9896–9901. https://doi.org/10.1021/am403223s.

(189) Hansen, C. M. THE THREE DIMENSIONAL SOLUBILITY PARA METER, 1967.

(190) Hansen, C. M. *Hansen Solubility Parameters: A User's Handbook*, Second Edi.; (CRC Press, 2007.

(191) Barton, A. F. M. CRC Handbook of Solubility Parameters and Other Cohesion Parameters, Second Edition. *CRC Handb. Solubility Parameters Other Cohes. Parameters, Second Ed.* **2017**, 1–739. https://doi.org/10.1201/9781315140575/CRC-HANDBOOK-SOLUBILITY-PARAMETERS-COHESION-PARAMETERS-ALLAN-BARTON.

(192) Budkowski, A.; Rysz, J.; Scheffold, F.; Klein, J.; Fetters, L. J. Effect of Deuterium Substitution on the Surface Interactions in Binary Polymer Mixtures. *J. Polym. Sci. Part B Polym. Phys.* **1998**, *36* (15), 2691–2702. https://doi.org/10.1002/(SICI)1099-0488(19981115)36:15<2691::AID-POLB3>3.0.CO;2-D.

(193) Lee, B.; Littrell, K.; Sha, Y.; Shevchenko, E. V. Revealing the Effects of the Non-Solvent on the Ligand Shell of Nanoparticles and Their Crystallization. *J. Am. Chem. Soc.* **2019**, *141* (42), 16651–16662. https://doi.org/10.1021/jacs.9b06010.

(194) Orofino, T. A.; Flory, P. J. Relationship of the Second Virial Coefficient to Polymer Chain Dimensions and Interaction Parameters. *J. Chem. Phys.* **2004**, *26* (5), 1067. https://doi.org/10.1063/1.1743472.

(195) Paulse, C. D.; Pickup, P. G. Chronoamperometry of Polypyrrole: Migration of Counterions and Effect of Uncompensated Solution Resistance. *J. Phys. Chem.* **1988**, *92* (24), 7002–7006. https://doi.org/10.1021/j100335a032.

(196) Ma, T.; Li, C. H.; Thakur, R. M.; Tabor, D. P.; Lutkenhaus, J. L. The Role of the Electrolyte in Non-Conjugated Radical Polymers for Metal-Free Aqueous Energy Storage Electrodes. *Nat. Mater.* **2023**, *22* (4), 495–502. https://doi.org/10.1038/s41563-023-01518-z.

(197) Wang, S.; Li, F.; Easley, A. D.; Lutkenhaus, J. L. Real-Time Insight into the Doping Mechanism of Redox-Active Organic Radical Polymers. *Nat. Mater.* **2019**, *18* (1), 69–75. https://doi.org/10.1038/s41563-018-0215-1.

(198) Zhang, Y.; Park, A.; Cintora, A.; McMillan, S. R.; Harmon, N. J.; Moehle, A.; Flatté, M. E.; Fuchs, G. D.; Ober, C. K. Impact of the Synthesis Method on the Solid-State Charge Transport of Radical Polymers. *J. Mater. Chem. C* **2017**, *6* (1), 111–118. https://doi.org/10.1039/c7tc04645f.

(199) Zimm, B. H. Molecular Theory of the Scattering of Light in Fluids. *J. Chem. Phys.* **2004**, *13* (4), 141. https://doi.org/10.1063/1.1724013.

(200) Teixeira, J.; IUCr. Small-Angle Scattering by Fractal Systems. *urn:issn:0021-8898* **1988**, *21* (6), 781–785. https://doi.org/10.1107/S0021889888000263.

(201) Dewey, T. G. *Fractals in Molecular Biophysics*; Oxford University Press, 1997.

(202) De Gennes, P. G. Scaling Concepts in Polymer Physics. Cornell University Press. *Ithaca N.Y.,* **1979**, 324.

(203) Hammouda, B.; Ho, D. L. Insight into Chain Dimensions in PEO/Water Solutions. *J. Polym. Sci. Part B Polym. Phys.* **2007**, *45* (16), 2196–2200. https://doi.org/10.1002/polb.21221.

(204) Hiemenz, P. C.; Lodge, T. P. Polymer Chemistry. **2007**. https://doi.org/10.1201/9781420018271.

(205) Joo, Y.; Agarkar, V.; Sung, S. H.; Savoie, B. M.; Boudouris, B. W. A Nonconjugated Radical Polymer Glass with High Electrical Conductivity. *Science (80-.).* **2018**, *359* (6382), 1391–1395. https://doi.org/10.1126/science.aao7287.

Appendix

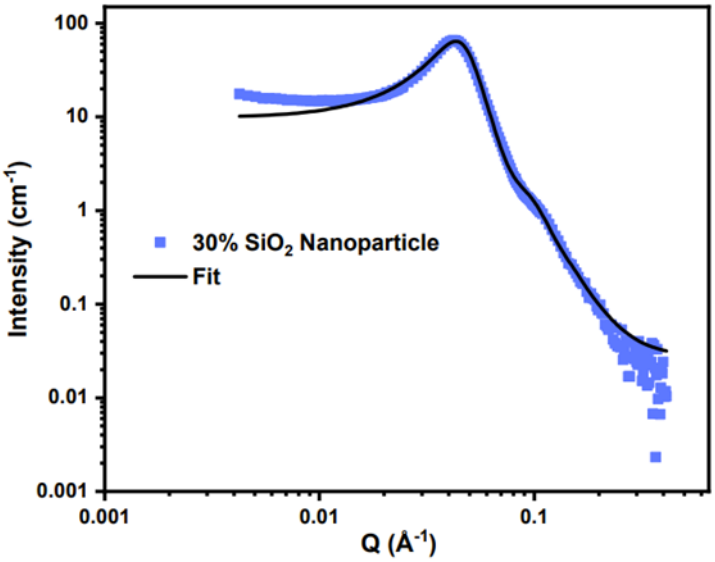

Figure 44. Small angle neutron scattering curve for the 30 wt.% SiO_2 nanoparticles (purple squares) fit with sphere model (black line).

Table 12. Variables used in combined model fit (core-shell sphere and polymer excluded volume model), as well as the range of values used in the fitting process.

Model	Variables	Value (units)
Form factor: Core-shell sphere	Core_radius	45 Å
	Effective thickness of shell	2-20 Å
	SLD_core	4.3 E-06 $Å^{-2}$
	SLD_shell	4.2-5.9 E-06 $Å^{-2}$
	SLD_solvent	4.7-6.2 E-06 $Å^{-2}$
	Polydispersity_radius	0.1-1.0 Å
	Polydispersity_thickness	0.1-1.0 Å
Form factor: Polymer excluded volume	Radius of gyration	4.0-20 Å
	Porod exponent	1.0-3.0
Structure factor: square well	Well depth	1.5 kT
	Well width	1.0-2.0 diameteres
Structure factor: sticky hard sphere	perturb	0.01-0.1
	stickiness	0.06-0.13

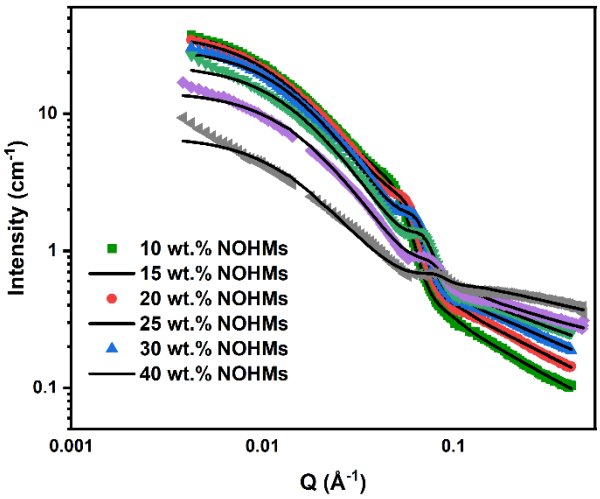

Figure 45. Small angle neutron scattering curve for the 10-40 wt.% NOHMs nanoparticles fit with the combine model (black line).

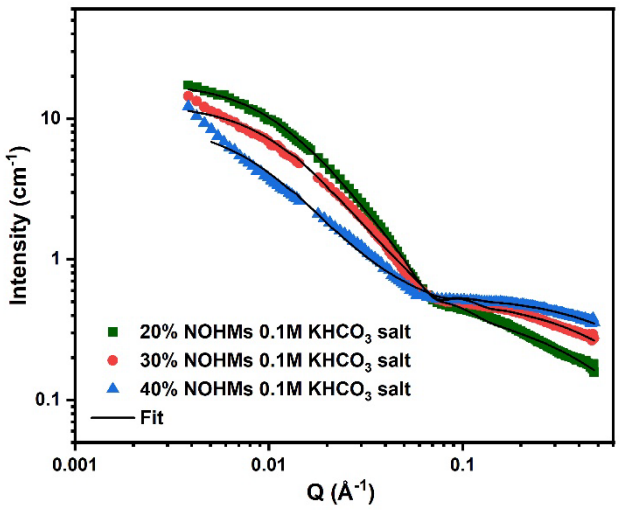

Figure 46. Small-angle neutron scattering profile of 20-40 wt.% NOHMs in presence of supporting electrolyte, 0.1 M $KHCO_3$ including fits to the combined model.

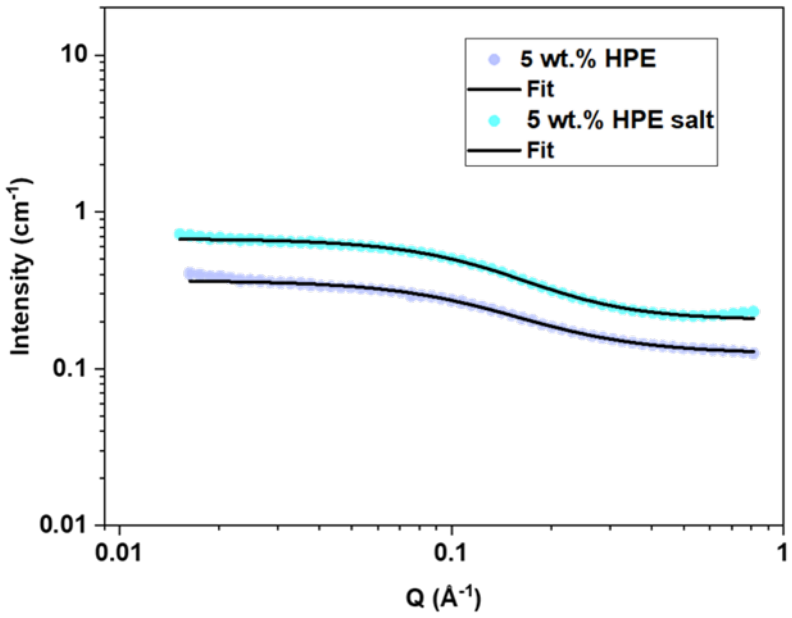

Figure 47. SANS profile fit of 5 wt.% HPE in aqueous solution with and without salt. 5 wt.% salt solution scattering profile and fit are scaled for clarity.

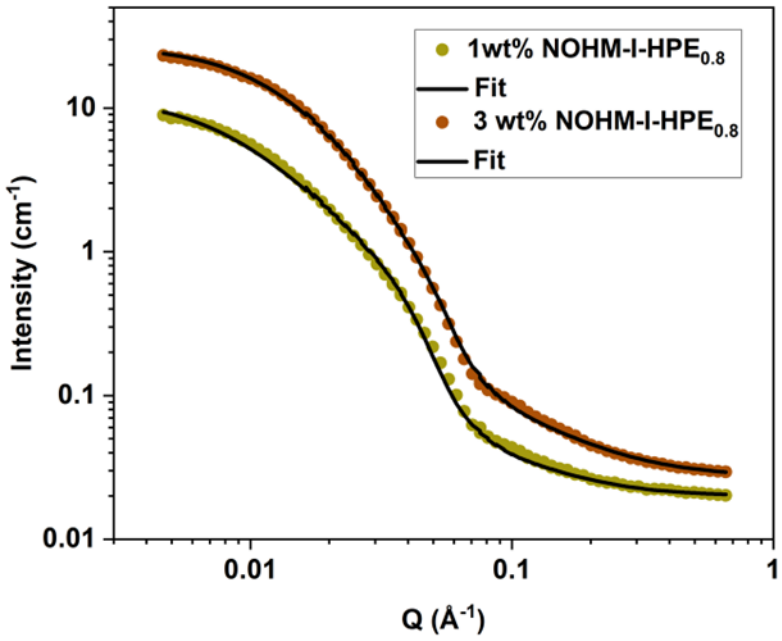

Figure 48. SANS profile fit of 1 wt.% and 3 wt.% NOHM-I-HPE$_{0.8}$ in aqueous solution, including fits to the combined model.

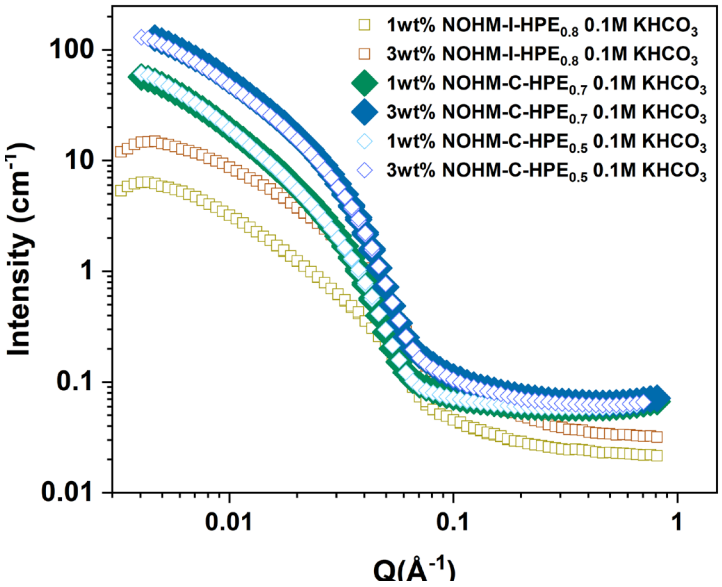

Figure 49. SANS profile of 1 wt.% and 3 wt.% NOHM-I-HPE and NOHM-C-HPE in aqueous solution with salt. 1 wt.% and 3 wt.% NOHM-C-HPE$_{0.7}$ scattering profiles are intentionally enlarged for clarity.

s

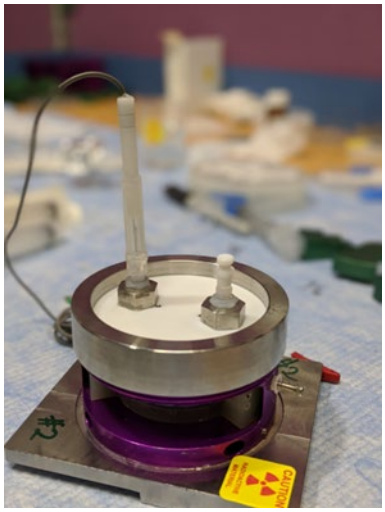

Figure 50. A picture of the cell used for neutron reflectivity experiments.

Table 13. SLD of the components calculated using neutron activation calculator.

Component	**SLD (10^{-6} Å^{-2})**
Si	2.07
Au	4.63
Cr	3.03
SiO	2.89
HPE polymer	0.52
SiO_2 Nanoparticle	4.20
D_2O	6.35
K	0.49
Zn	3.73

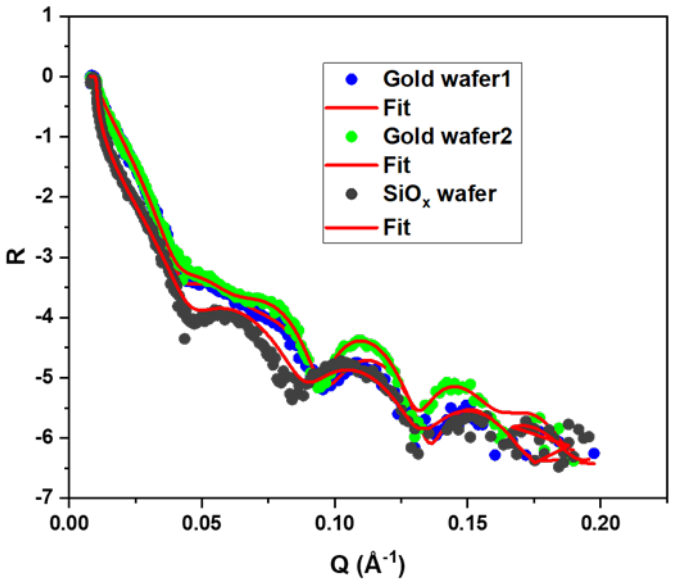

Figure 51. Neutron reflectivity profiles of Au (green and blue circles) and SiO_x (black circles) wafers with fit (red line)

Table 14. Density profile parameters of Au and SiO_x wafers obtained from the reflectivity fit of the Au and SiO_x wafers.

Sample	Parameters	Si	SiO_x	Cr	Au
	SLD (10^{-6} Å^{-2}) ± error	2.07	2.89		
SiO_x Wafer in air	Z (Å) ± error	-	143 ± 0.50		
	R(Å) ± error	1.5	4.88 ± 0.20		
	SLD (10^{-6} Å^{-2}) ± error	2.07	-	3.03	4.63
Au Wafer in air	Z (Å) ± error	-	-	46.4 ± 0.12	140 ± 1
	R(Å) ± error	4.0 ± 0.1	-	7.96 ± 0.01	4.94± 0.07
	SLD (10^{-6} Å^{-2}) ± error	2.07	-	3.03	4.63
Au Wafer in air	Z (Å) ± error	-	-	56.6 ± 0.18	140 ± 1
	R(Å) ± error	1.00 ± 0.01	-	5.36 ± 0.30	7.24 0.38

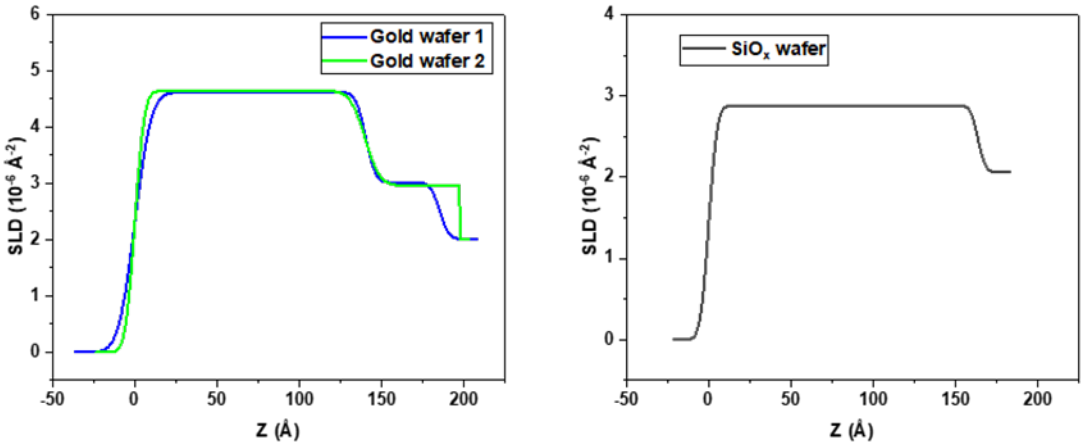

Figure 52. SLD profile of Au (left) and SiO_x (right) wafers obtained from reflectivity fit of the Au and SiO_x wafers.

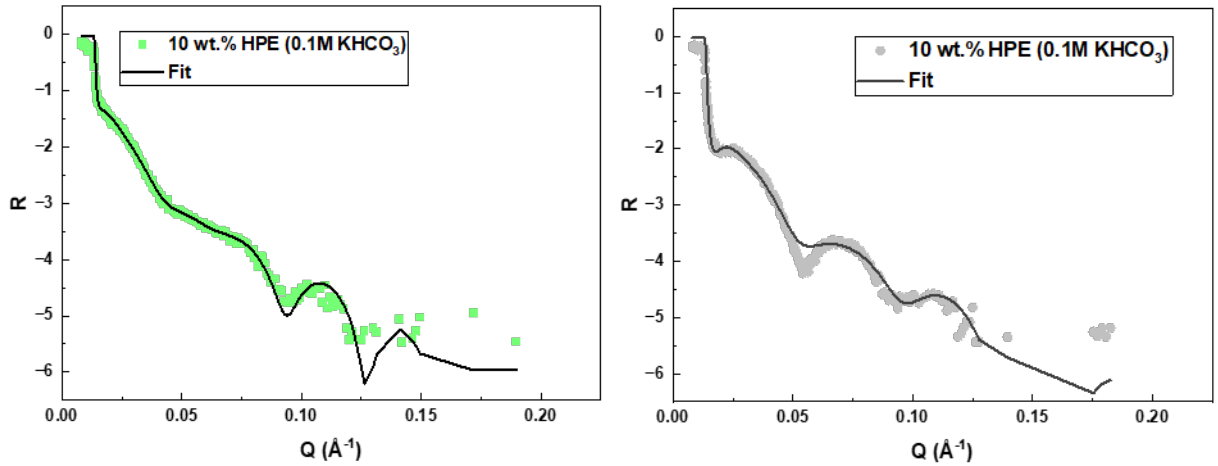

Figure 53. Neutron reflectivity profiles (circles) and fit (line) of 10 wt.% HPE in D_2O in presence of 0.1 M $KHCO_3$ salt near Au surface (left) and SiO_x surface (right).

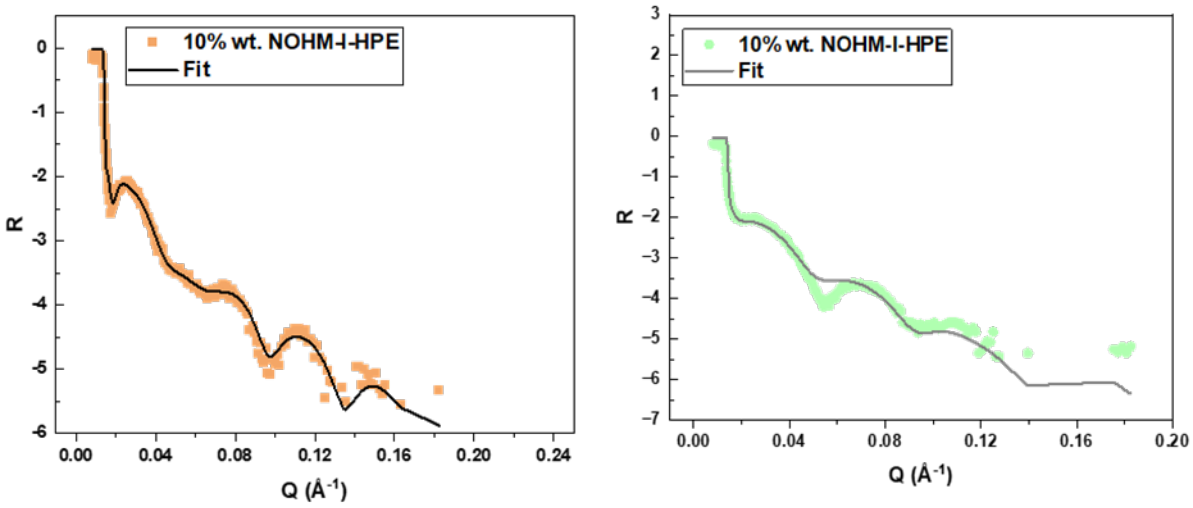

Figure 54. Neutron reflectivity profiles (circles) and fit (line) of 10 wt.% NOHM-I-HPE in D_2O near Au surface (left) and SiOx surface (right).

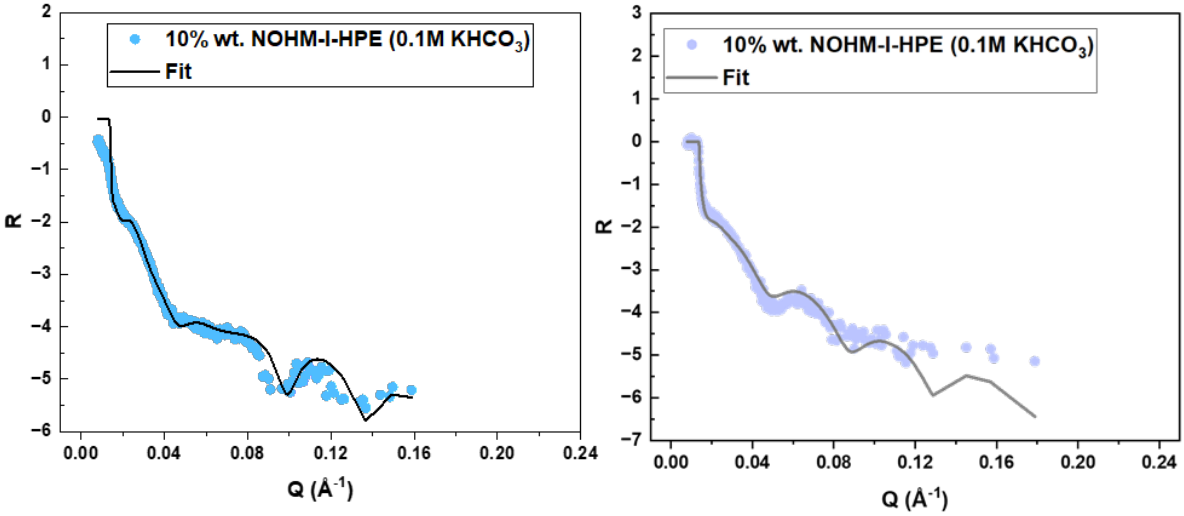

Figure 55. Neutron reflectivity profiles (circles) and fit (lines) of 10 wt.% NOHM-I-HPE in D_2O in presence of 0.1M $KHCO_3$ salt near Au surface (left) and SiO_x surface (right).

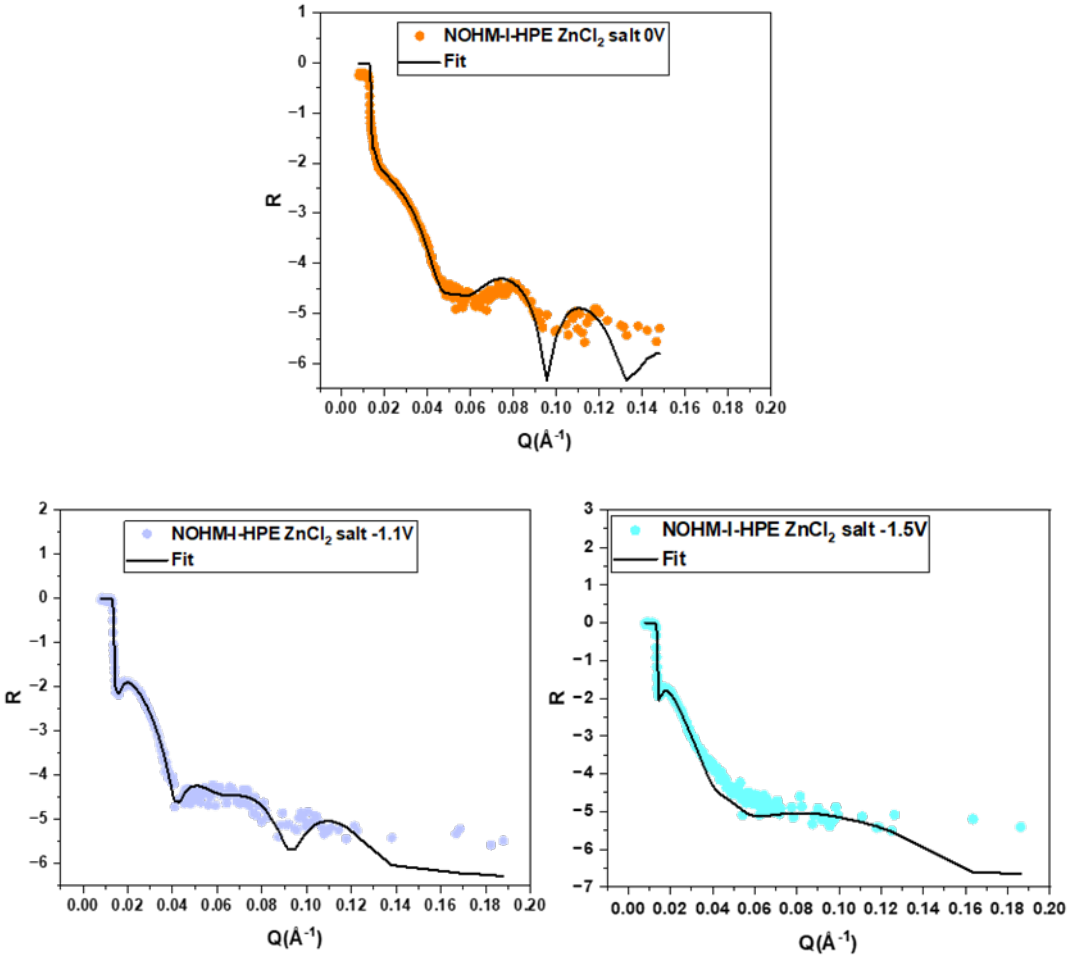

Figure 56. Neutron reflectivity profile (circle) and fit (line) of 10 wt.% NOHM-I-HPE in D_2O in presence of $ZnCl_2$ salt near Au surface at different potentials; 0V (top) -1.1V (bottom left), -1.5V (bottom right).

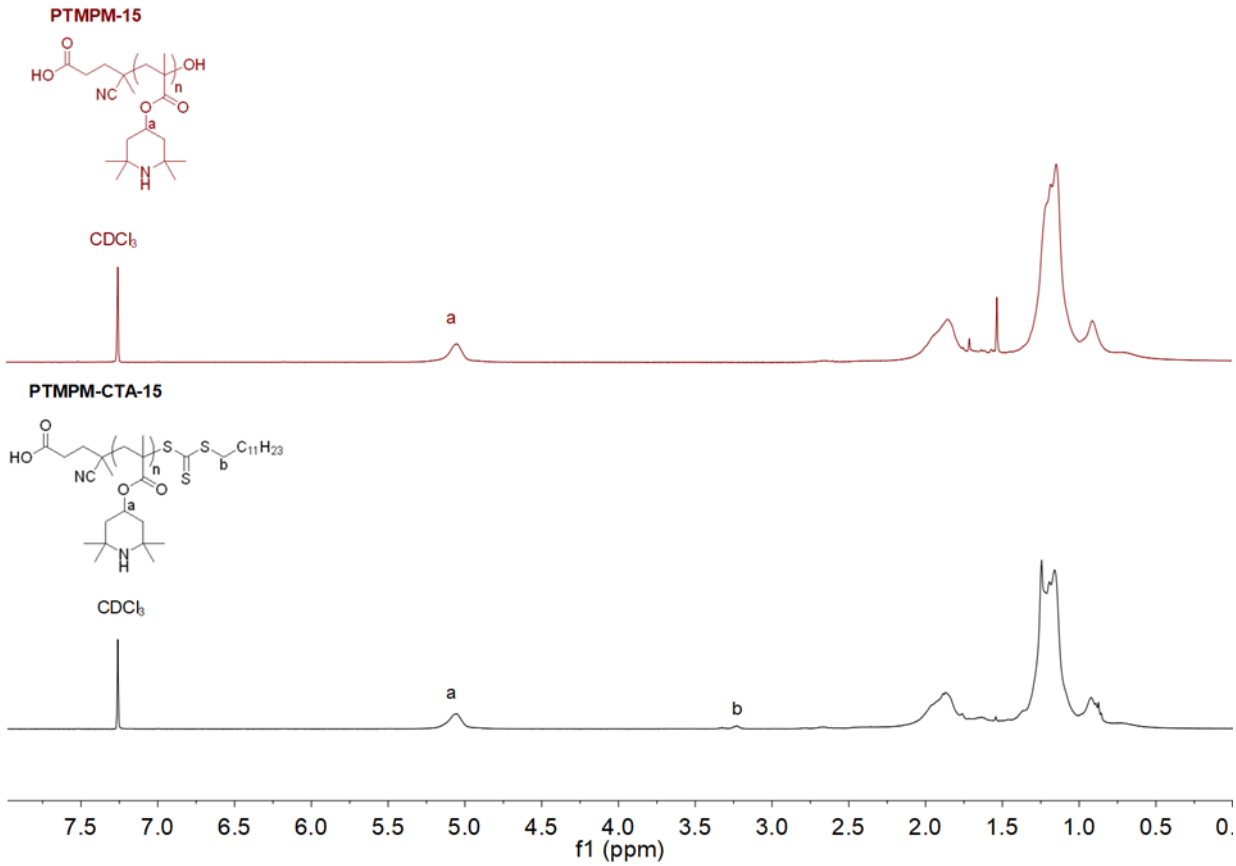

Figure 57. ^{1}H-NMR of PTMPM-CTA-15 and PTMPM-15.

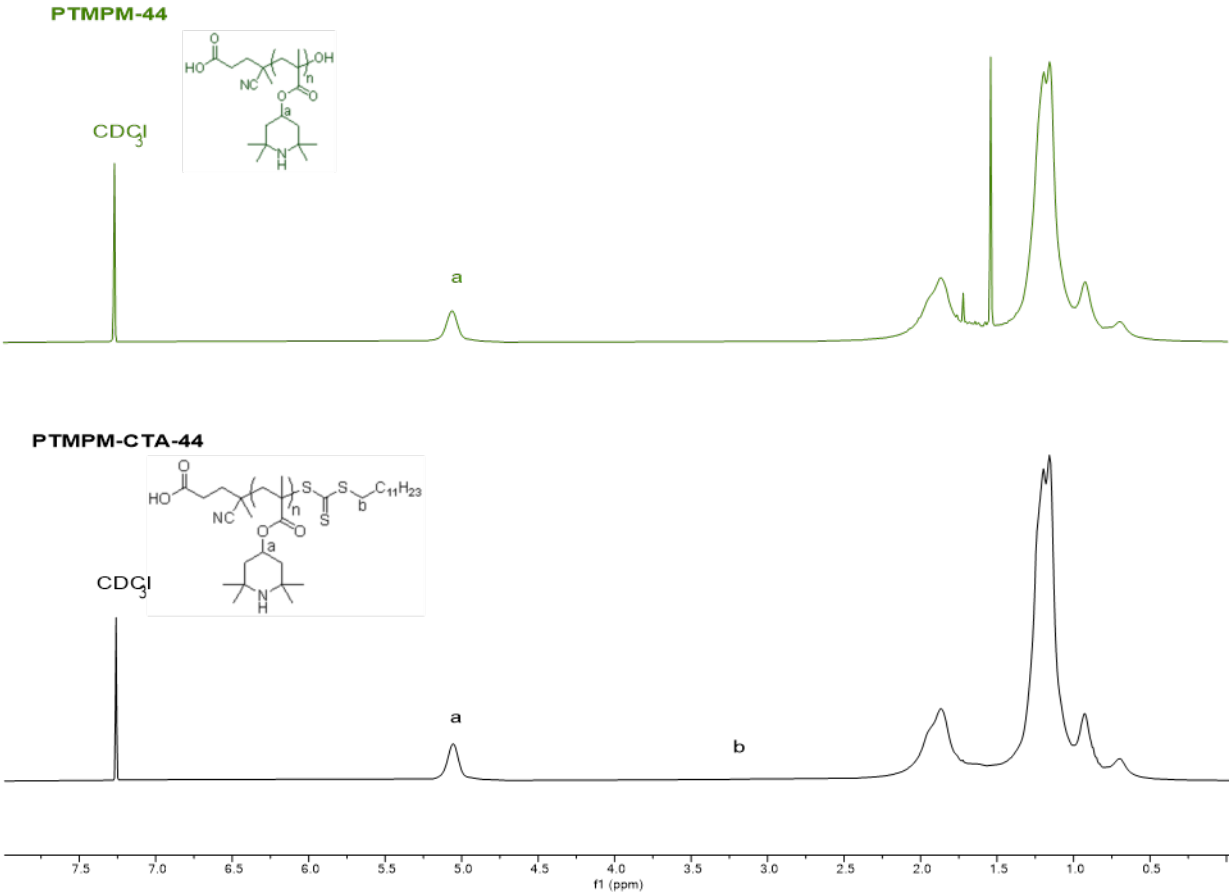

Figure 58. ^{1}H-NMR of PTMPM-CTA-44 and PTMPM-44.

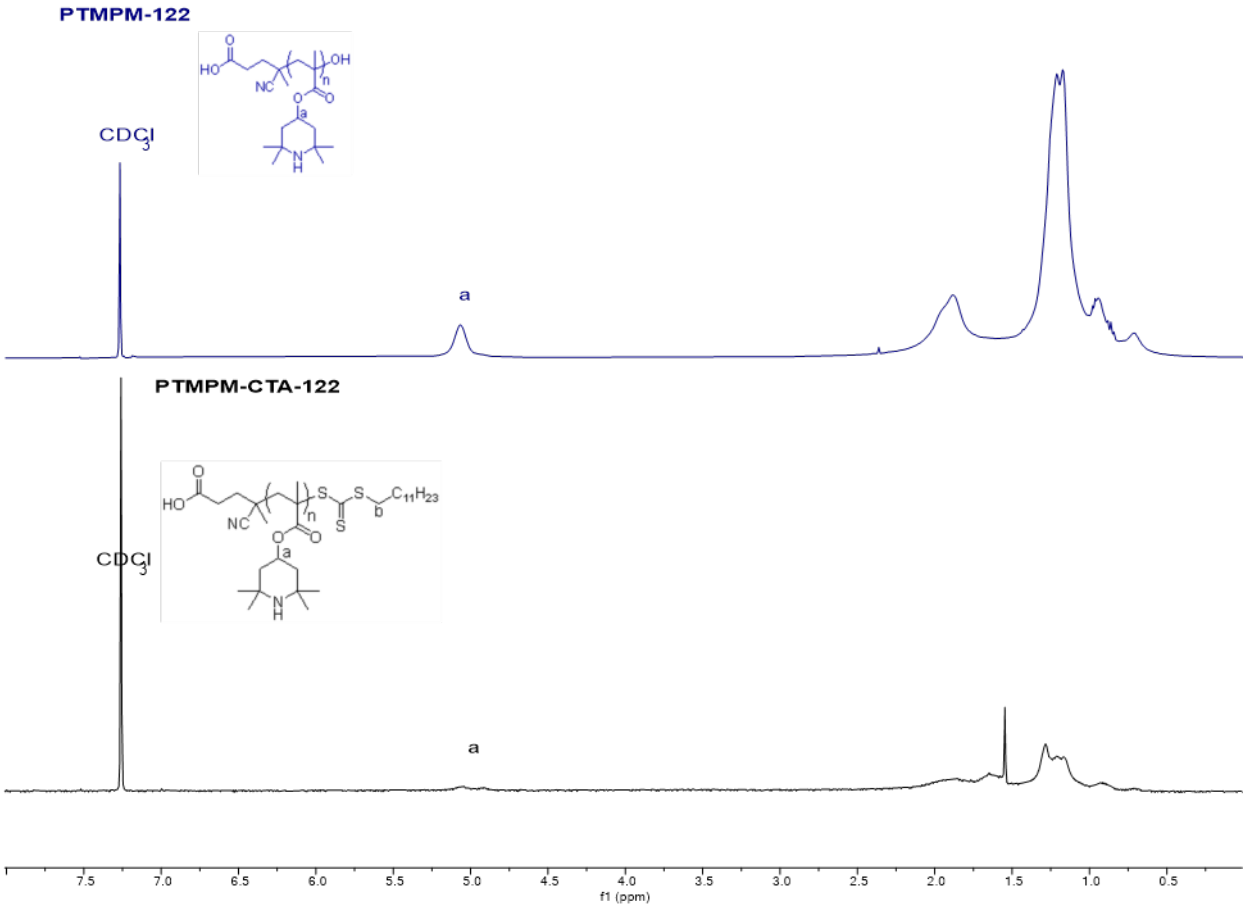

Figure 59. ^{1}H-NMR of PTMPM-CTA-122 and PTMPM-122.

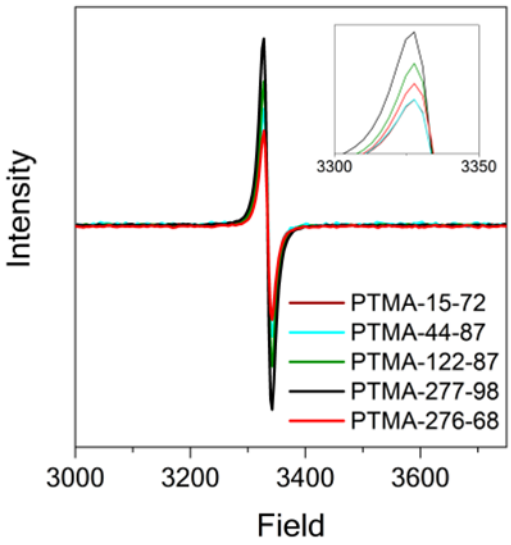

Figure 60. Electron paramagnetic resonance (EPR) spectroscopy for all the PTMA-X-R polymers considered. EPR data was collected on the polymer powders.

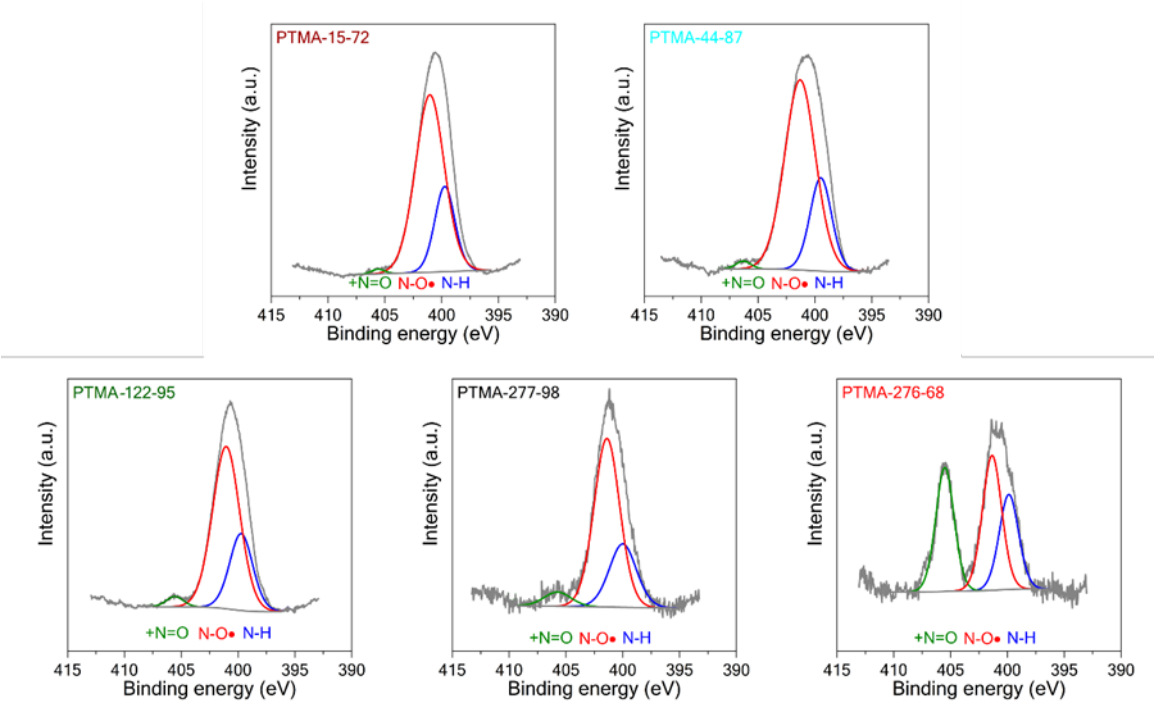

Figure 61. N1s nitrogen deconvolution data for all the PTMA-X-R data.

Table 15. Molecular weight (M_w) and radius of gyration (R_g) calculation from Guinier Analysis of 1 wt.% PTMA-X-R in respective solvents.

Sample Name	**Solvent (Temperature)**	**M_w (kg/mol)**	**R_g ± error (Å)**
PTMA-276-68	d-NMP (25 °C)	155	65 ± 2
PTMA-276-68	d-NMP (60 °C)	146	66 ± 2
PTMA-276-68	d-EC:d-DMC (25 °C)	142	71± 4
PTMA-276-68	d-EC:d-DMC (60 °C)	142	69 ± 3
PTMA-277-98	d-NMP (25 °C)	130	100 ± 5
PTMA-277-98	d-NMP (60 °C)	130	96 ± 3

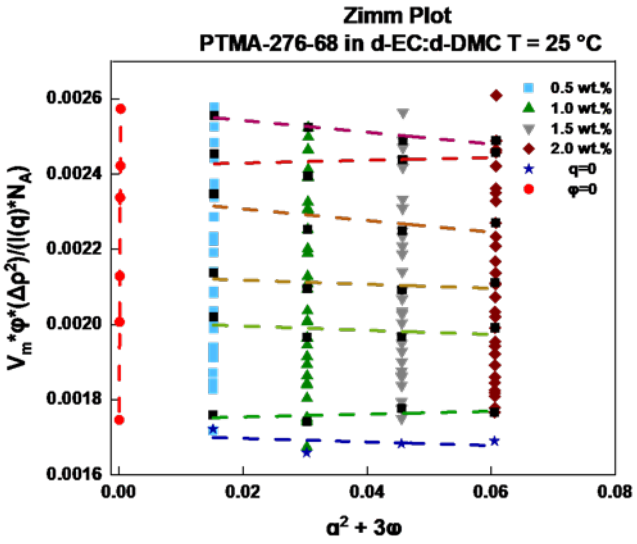

Figure 62. Representative Zimm plot of PTMA-276-68 in d-EC:d-DMC at T = 25 °C.

Table 16. Second Virial Coefficient (A_2), Molecular weight (M_w) and radius of gyration (R_g) from Zimm analysis before correction.

Sample Name	**Solvent (Temperature)**	**A_2 (mol cm^3 g^{-2})**	**M_w (kg/mol)**	**R_g (Å)**
PTMA-276-68	d-NMP (25 °C)	0.156×10^{-3}	106.8	103
PTMA-276-68	d-NMP (60 °C)	0.207×10^{-3}	116.8	118
PTMA-276-68	d-EC:d-DMC (25 °C)	1.46×10^{-5}	170.0	80
PTMA-276-68	d-EC:d-DMC (60 °C)	1.04×10^{-4}	165.0	88
PTMA-277-98	d-NMP (25 °C)	0.216×10^{-3}	211.2	200
PTMA-277-98	d-NMP (60 °C)	0.263×10^{-3}	156.2	145

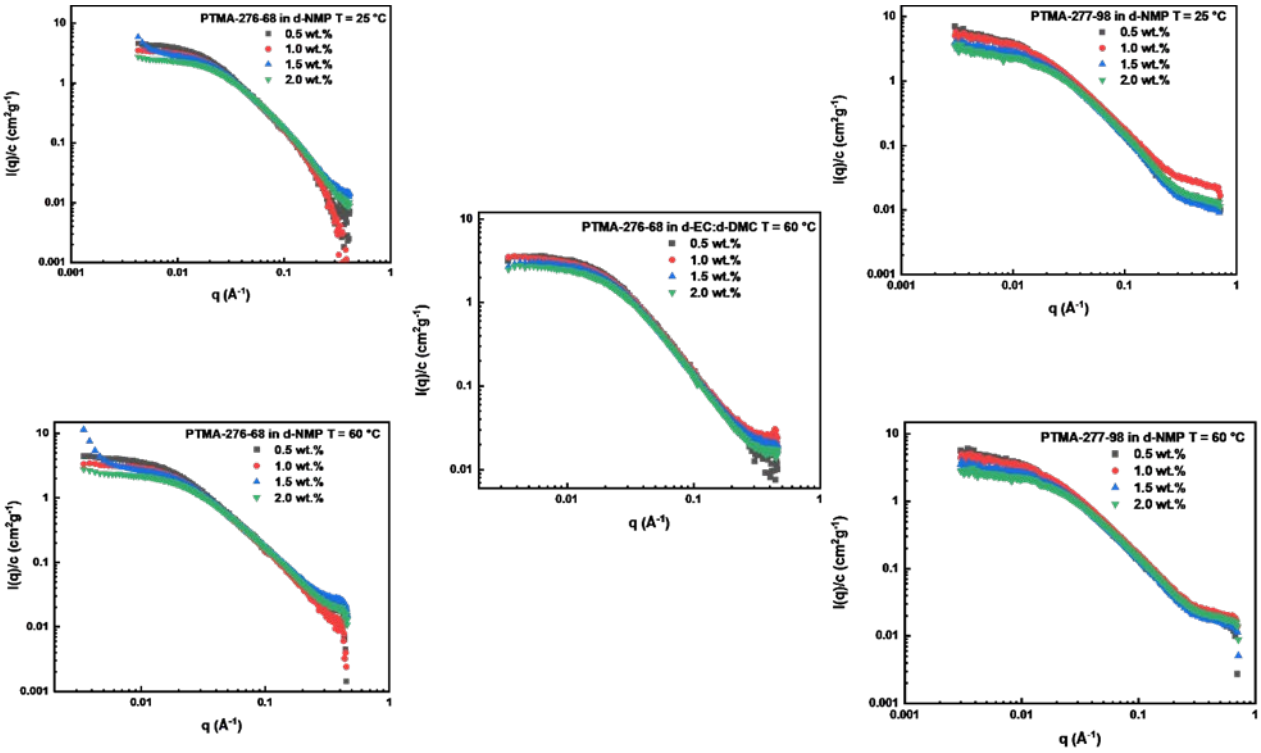

Figure 63. Change in scattering profile of PTMA-276-68 in d-NMP (left), d-EC:d-DMC (center) and PTMA-277-98 in d-NMP (right) at low-q proportional to the increase in concentration of counter-ion in solution.

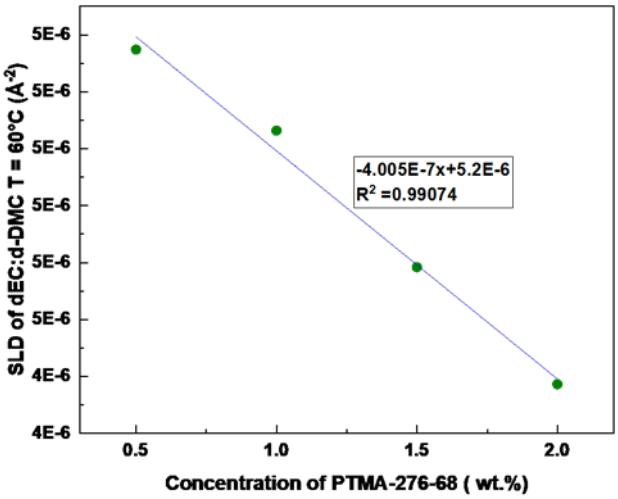

Figure 64. Representative plot showing corrected SLD of solvent d-EC:d-DMC at T= 60 °C

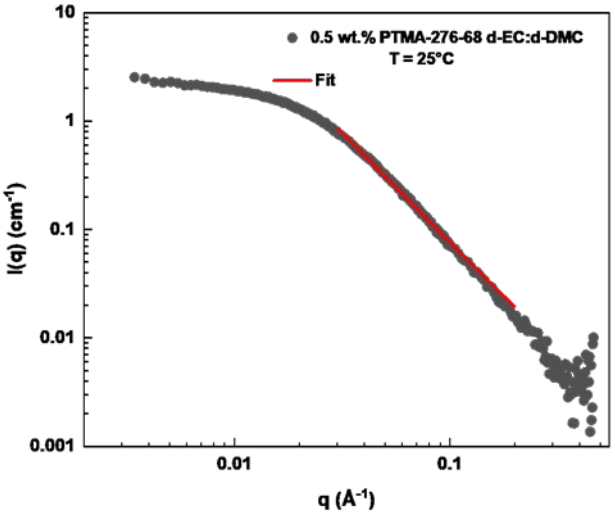

Figure 65. Representative fractal dimension fit of PTMA-276-68 in d-EC:d-DMC T= 25 °C.

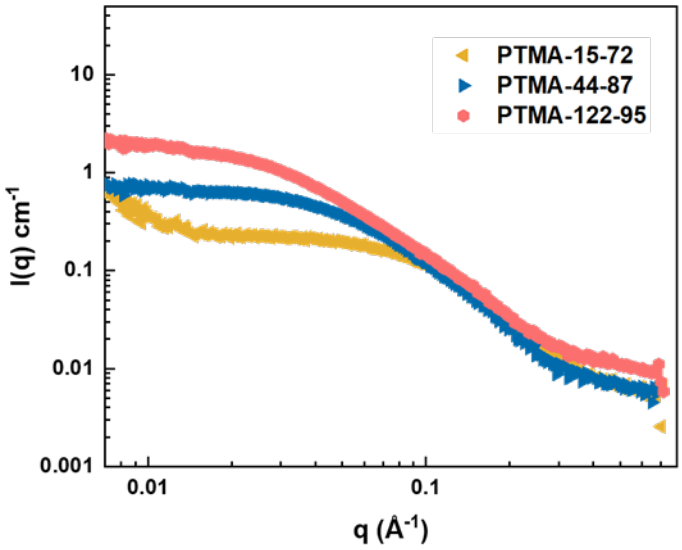

Figure 66. Small-angle neutron scattering profiles of 1 wt.% PTMA-X-R in d-NMP at T = 25 °C oxidized by H_2O_2.

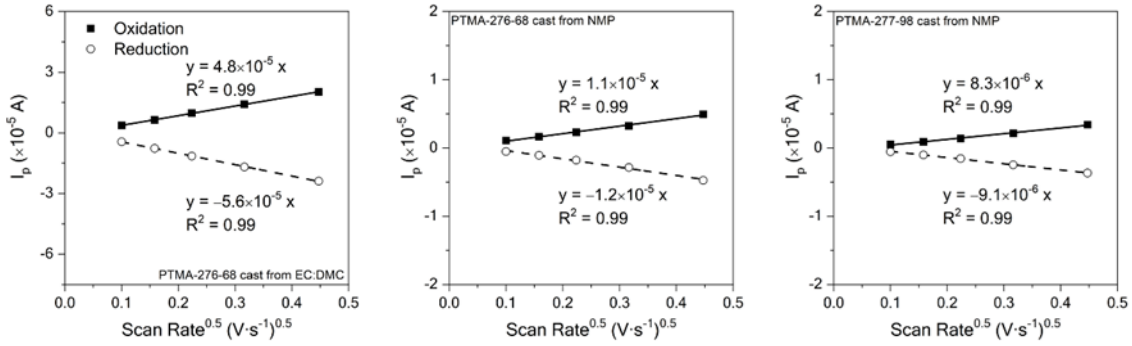

Figure 67. Peak current *vs.* square-root scan rate for PTMA-276-68 thin films cast from (left) EC:DMC solution and (center) NMP solution and for (right) PTMA-277-98 cast from NMP solution. Peak currents (I_p) are taken from Figure 43.

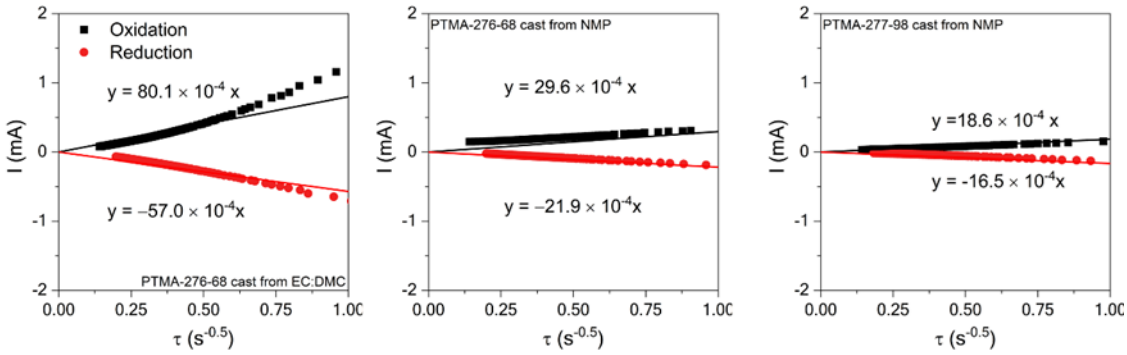

Figure 68. Cottrell plots for PTMA-276-68 thin films cast from (left) EC:DMC solution and (center) NMP solution and for (right) PTMA-277-98 cast from NMP solution. The cyclic voltammograms were obtained in a three-electrode beaker cell with the PTMA-X-R thin films on glassy carbon working electrodes, Pt wire counter electrode, Ag/AgCl (sat.) reference electrode, and 0.5 M $TEABF_4$ in water supporting electrolyte.

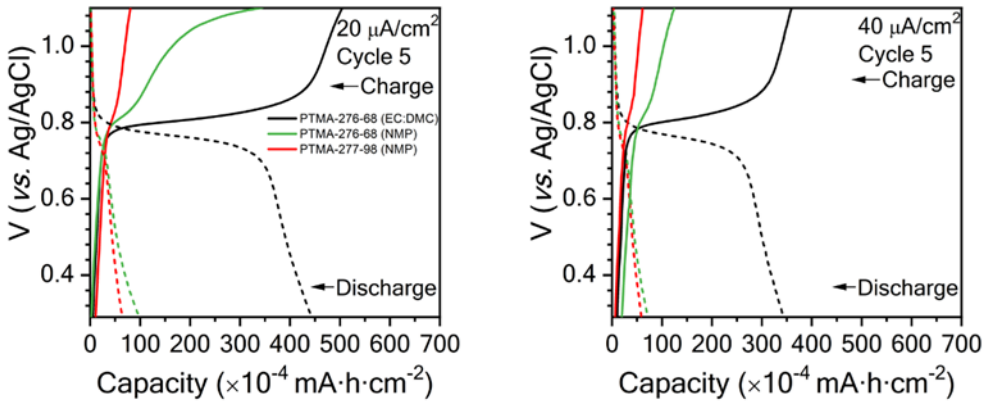

Figure 69. Galvanostatic charge-discharge (GCD) plots for PTMA-276-68 thin films cast from (left) EC:DMC solution and (center) NMP solution and for (right) PTMA-277-68 cast from NMP solution. The GCDs were obtained in a three-electrode beaker cell with the PTMA-X-R thin films on glassy carbon working electrodes, Pt wire counter electrode, Ag/AgCl (sat.) reference electrode, and 0.5 M $TEABF_4$ in water supporting electrolyte.

Vita

Md Ashraful Haque was born on November 3rd, 1995 in Bangladesh. He completed his Bachelor of Science degree from the department of Applied Chemistry and Chemical Engineering at the University of Dhaka in 2016. He then earned his Master of Science degree from the same department in 2017. Afterward, he pursued higher studies in the US and got admission to the University of Tennessee, Knoxville (UTK) in the fall of 2018. At UTK, he worked with Dr. Mark D. Dadmun to complete his research work and earned his Doctor of Philosophy degree in December 2023.